COLOR IRIS RECOGNITION AND MATCHING USING QUATERNION GABOR WAVELETS

BY

Fares Saleh Al-Qunaieer

A Thesis Presented to the

DEANSHIP OF GRADUATE STUDIES

KING FAHD UNIVERSITY OF PETROLEUM & MINERALS

DHAHRAN, SAUDI ARABIA

In Partial Fulfillment of the
Requirements for the Degree of

MASTER OF SCIENCE

In

INFORMATION AND COMPUTER SCIENCE

January 2009

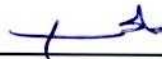# KING FAHD UNIVERSITY OF PETROLEUM AND MINERALS

DHAHRAN 31261, SAUDI ARABIA

DEANSHIP OF GRADUATE STUDIES

This thesis, written by **Fares Saleh Al-Qunaieer** under the direction of his thesis advisor and approved by his thesis committee, has been presented to and accepted by the Dean of Graduate Studies, in partial fulfillment of the requirements for the degree of **MASTER OF SCIENCE IN COMPUTER SCIENCE.**

Thesis Committee

_____
Dr. Lahouari Ghouti (Thesis Advisor)

_____
Dr. Muhammad Al-Mulhem (Member)

_____
Dr. Muhammad Al-Suwaiyel (Member)

_____
Dr. Kanaan A. Faisal
Department Chairman

_____
Dr. Salam A. Zummo
Dean of Graduate Studies

_____
17/4/09
Date

II

DEDICATION

To my parents

Who taught me the value of knowledge

ACKNOWLEDGMENT

TABLE OF CONTENTS

LIST OF FIGURES

LIST OF TABLES

THESIS ABSTRACT

Name: Fares Saleh Al-Qunaieer

Title: Color Iris Recognition and Matching Using Quaternion Gabor Wavelets

Major Field: Information and Computer Science

Date of Degree: February 2009

Biometric systems have gradually become an accepted mean for person identification and verification. Recently, person identification using iris features has received a lot of attention in both research and industry communities. This is mainly due to the unique characteristics and texture found in iris images. Most proposed iris recognition techniques are based on gray-level representations. The aim of this research is to develop and investigate novel methods for the automatic recognition and matching of color iris images based on hypercomplex (Quaternion) representations. The performance of Quaternion image representation is compared with that of other representations, and a study of the results is conducted. The well-known IrisCode algorithm, developed by John Daugman, is extended to the color domain. Furthermore, in the present research, hypercomplex processing and filtering of color iris images are defined.

ملخص الرسالة

الاســــــــــــم:	فارس بن صالح بن عبدالعزيز القنيعير
عنوان الرسالة:	التعرف على القزحية الملونة ومطابقتها باستخدام مرشح جابور المركب المتعدد
التخصـــــــص:	علوم الحاسب الآلي
تاريخ التخـرج:	صفر 1430

اكتسبت الأنظمة الحيوية بشكل تدريجي القبول كوسيلة فعالة للتعرف على الأشخاص. في الآونة الأخيرة، ازداد الاهتمام باستخدام القزحية كوسيلة للتعرف على الأشخاص، وقد تم إفراد العديد من البحوث حول ذلك الموضوع. يكمن السبب في ذلك إلى الخصائص والنقوش الفريدة التي تحملها القزحية، مما يجعلها وسيلة ممتازة لتمييز الأشخاص. معظم الأساليب والتقنيات المرتكزة على القزحية كوسيلة للتعرف على الأشخاص تعتمد على الصور ذات التدرجات الرمادية. يهدف هذا البحث إلى تطوير واستكشاف طرق جديدة ومبتكرة للتعرف على الأشخاص عن طريق صور القزحية الملونة وذلك باستخدام التمثيل المركب المتعدد. يعقد هذا البحث دراسة مقارنة بين أداء التمثيل المركب المتعدد وأداء تمثيلات أخرى. الخوارزمية الأكثر شهرة وانتشاراً تعمل على الصور ذات التدرجات الرمادية وقد تم تطويرها بواسطة دوجمان. في هذا البحث تم تطوير هذه الخوارزمية لتعمل على الصور الملونة وذلك باستخدام التمثيل المركب المتعدد وجبر كليفورد. بالإضافة إلى ذلك فقد تم تطوير فلتر جابور المركب المتعدد وذلك لاستخلاص السمات المميزة للصورة ثم إنشاء تمثيل مناسب لها.

CHAPTER ONE

INTRODUCTION

1.1. Introduction

Technology has become dominant in the daily life routines. People use technology to facilitate communication, automate processes, and enforce security. Technology can be found in many forms and almost everywhere. For instance, cell phones, laptops, and ATM machines are using different forms of technologies. Several of the existing technologies require a mean for user authentication and identification. There are many existing forms of identification mechanisms to ensure each person's identity. Some of the commonly-used methods are usernames, passwords, electronic cards, and smart cards. Although these methods are effective, they suffer from serious drawbacks. First, they can be used by others for identity fraud. This can be achieved, for example, by using the username and password of another person. Such methods occur very much in Internet applications that require username and password. Also, the electronic or smart card of the intended person can be stolen, or else lost or forgotten. Furthermore, in almost every form requiring a username and password, there is a link to enable users to request password re-setting or retrieval if forgotten.

To solve these problems, the use of the human body's parts or behavior was considered. Systems based on these personal traits are called *biometric systems*. These systems were,

and still continue to be, the focus of active research and developmental efforts. Furthermore, they have received wide acceptance in access-control applications. Several biometric/personal traits such as fingerprints, face, iris, ear, voice, palmprint, hand geometry and gait are used for their uniqueness as characterizing features. In this way, it is provably asserted that the subject under authentication/recognition is the intended person because of the unique traits. This effective person discrimination is contrasted with systems relying on usernames, passwords or electronic cards, which can be forgotten, lost, or stolen.

1.2. Biometric Systems

As briefly stated earlier, biometric systems are those systems that use characteristics of the human's physical body or behavior as means of identification of different people. Thus, biometrics is considered more efficient and is more reliable for person identification. Biometric systems can be used in various ways, depending on the field of application and security level. They can be used in the process of authorization for the access to restricted areas or machines. Also, many companies and organizations nowadays are using biometric systems to take attendance of their staff. Another area of usage is in forensic science as a means of investigating crime scenes. Moreover, biometrics is used in border-control systems in many countries, mostly by using fingerprints or the iris as the means of identification.

Two types of traits can be used in biometric systems:

Physiological: Parts of the body are used as unique characteristics. Examples of this type are fingerprints, face, ear, hand geometry, hand veins, iris, and Deoxyribonucleic Acid (DNA).

Behavioral: The behavioral characteristics are taken as the means of identification. For instance, keystrokes, signature, and gait are used in this type of biometrics.

In general, in order to use biometrics, there should be a way of capturing the chosen unique characteristic. Then, some preprocessing is applied in order to enhance the input. After that, the most discriminating features are extracted, and then encoded in a convenient representation template for storage and processing. Query inputs are compared with stored templates to decide the identity of the subject under investigation.

Some biometric systems have gained wide acceptance in various applications. The most common of these are fingerprints and these are used almost everywhere from authorization and attendance systems to a means of computer access. Other biometrics, such as the iris, are gradually gaining acceptance because of their high performance, efficiency, and ease of use.

1.3. Process of Iris Recognition

In order to use the eye's iris as a means of identification, some processing should be carried out on the image of the eye to extract useful information that will be further used

for discrimination. In the literature, there is a general consensus among researchers on the main steps that should be applied on the image to extract useful information and match between different images. They are as follows [1]:

1. Image preprocessing

Acquired iris images contain some unnecessary information such as sclera, eyelids and pupil [1]. The main target is the iris region itself. So, there are methods to locate and extract the iris from the image, and then to convert it into an appropriate format to extract needed features. The main preprocessing steps are given below [1]:

a. Segmentation and localization

The iris is extracted from the eye image, by detecting the iris circle and the pupil circle and then excluding the pupil circle. Also, the intersection of the eyelids with the iris is excluded, as are the eyelashes and reflections. Figure 1.1 shows a segmented iris part where the eyelashes and reflections are removed.

b. Normalization

After the iris region is extracted, it is transformed into a format that will compare different iris regions consistently and efficiently. There are several sources of inconsistency, such as varying imaging distance, camera rotation, and head tilt [1]. One of the most famous methods consists of converting the Cartesian coordinate system into a polar coordinate system as suggested by Daugman [2]. This process is illustrated in Figure 1.2.
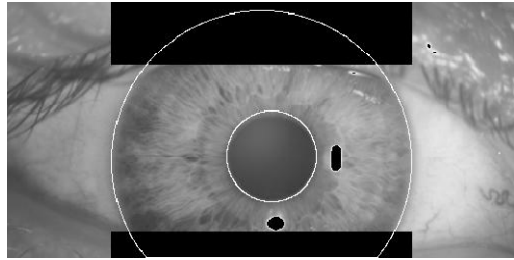
Figure 1.1: Iris segmentation and localization. [1]   Figure 1.2: Normalization to polar coordinate. [1]
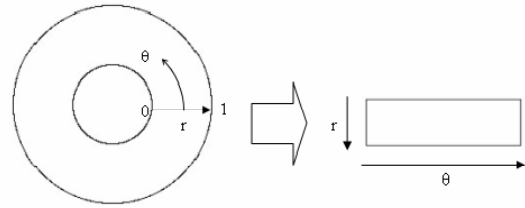
2. Features extraction and encoding

In this step, features, important for discrimination between different iris images, are extracted. These features are unique for each iris image [1]. The major difference between the various methods of iris recognition systems, proposed in the literature, lies in the features extraction and encoding step. After extracting the features, they are encoded in a way that is efficient for both storage and matching.

3. Matching

Comparisons between input iris images and stored iris images in the database are carried out in this step. For person identification, the iris of the person is photographed, and the previous steps are applied in order to get the iris code. Then, the input iris code is compared with iris codes in the database by using one of the methods of comparison outlined later in this Thesis.

1.4. Problem Statement

It had been proven that iris texture is a very efficient means for person identification. In the literature, most proposed approaches are dealing with grayscale iris images. This is due to adoption from fingerprint recognition techniques, which achieved very accurate results. Fingerprints are naturally grayscale images, and so grayscale image processing will achieve nearly optimal results. In iris images, colors carry a lot of information that will be lost if colors are discarded. According to the "*information preserving rule*" [**3**], information should be preserved until the final stage of classification. Thus, the performance of iris-based recognition systems should be increased if the color information is incorporated in the process of identification.

1.5. Proposed Research

The aim of the proposed research is to develop and investigate novel methods for the automatic recognition and matching of color iris images based on hypercomplex representations. Gray-level iris recognition systems, based on the well-known IrisCode patterns, developed by John Daugmann [**2**], have been widely accepted and deployed in most commercial iris recognition systems and products. In this Thesis, we intend to extend the concept of the IrisCode pattern to the color domain where a new formulation based on Clifford algebra is developed. This formulation will provide the mathematical background for hypercomplex representations, transforms and multi-resolution analysis (MRA). Hypercomplex Gabor wavelets will be developed to provide pattern feature

vectors which will be labeled as color IrisCodes. Furthermore, hypercomplex processing and filtering of color iris images will be defined.

Existing systems for recognizing and matching iris images against a database of known iris images (CASIA Databases and others) have been limited to the gray-level space, and hence they reduce the recognition efficiency due to the loss of color information which is an important component from an information-theoretic point of view.

Problems with the current approaches are not only the loss of color information but also related to the lighting-invariance property which can hinder the recognition accuracy.

Unlike the previous attempts to integrate color in iris recognition systems, our approach is novel. Firstly, it will aim to seamlessly integrate the color information into the recognition/matching system by letting the recognition process operate in the hypercomplex domain (based on Clifford Algebra). Secondly, we will not merely implement the proposed framework by separating the color components and operating in three (or reduced-color) independent spaces; rather we will use hypercomplex transforms which will encode color iris pattern features into a color-based IrisCode derived from Quaternionic Gabor wavelets representations which operate in a hypercomplex multi-resolution (MRA) space, exploiting the color/rotation/scale/lighting invariance properties of the hypercompelx Gabor wavelets. Our novel approach also has greater potential for addressing the problems of background noise and artifacts in color iris images by exploiting efficient hypercomplex edge-detection algorithms (spatial/transform/MRA) for

better color iris image segmentation which would allow better matching and recognition performance than their gray-based counterparts.

1.6. Research Objectives and Contributions

Almost all iris recognition methods, proposed in the literature, use gray-level images and process them to get the unique features of the iris. The objective of this research is to investigate the use of colors in the process of iris feature generation. We will use Hypercomplex image representation to represent the color images in a holistic manner, and we develop Quaternion Gabor Wavelets to process and represent color images. The results of the experiments will be compared with Daugman and other methods which will form a common benchmark.

The major research contributions are as follows:

- Propose an efficient means of color iris representation and processing. The processing is performed in a holistic manner.
- Study the effect of different types of noise on color iris images by using the proposed representation and comparing the results with other representations.
- Investigate the effect of low-pass filtering on the performance of the proposed representation and other representations against different types of noise.
- Compare the correlation performance of different color iris images between the proposed representation method and other representations.

- Study the effect of low-pass filtering on the correlations of different representations.

- Extend the well known Daugman algorithm to use color iris images based on the proposed representation, with filtering performed by using hypercomplex (quaternion) Log-Gabor filters.

1.7. Organization of Thesis

The rest of this Thesis is organized as follows. A review of existing methods is conducted in Chapter 2. In Chapter 3, Hypercomplex (Quaternion) representation is described with an explanation of Quaternion Fourier Transforms and convolution. Then, Gabor wavelets are described in Chapter 4, followed by the outline of the proposed method to extend it to the Quaternion domain. In Chapter 5, the methodology of the research and datasets used are presented along with a description of the techniques used in performance evaluation of the methodology, and this performance evaluation is given in detail. In conclusion, Chapter 6 points out the findings of this research, and it offers suggestions for possible future work.

CHAPTER TWO

LITERATURE REVIEW

2.1. Introduction

Iris-based person identification attracted many researchers to investigate and propose novel methods. Consequently, a lot of approaches for iris recognition were proposed in the literature. These include preprocessing iris images, extracting representative features, constructing and encoding the most convenient representation of the features, and various methods of matching depending on the extracted features.

The majority of the available techniques, including ours, concentrate on the process of feature extraction and encoding. A detailed review of the five most popular approaches will be given. Then, a brief description of the other techniques is given, in chronological order, where we restrict our attention to the processes of feature extraction, encoding, and matching.

2.2. The Five Most Popular Methods

2.2.1. Daugman Algorithm [2] [4] [5]:

Daugman was the first to propose an efficient algorithm to verify people by iris patterns. Most commercial products are based on this technique, such as the products of British

Telecom, Sandia Labs, U.K. National Physical Lab, Panasonic, LG, Oki, EyeTicket, Sensar, Sarnoff, IBM, SchipholGroup, Siemens, Sagem, IrisScan, and Iridian.

In order to apply the encoding algorithm, the portion of the iris should be extracted from the eye image. Iris extraction is carried out by locating the inner and outer boundaries of the iris. For this purpose, a coarse-to-fine strategy, terminating in single-pixel precision, is used to estimate the center coordinates and radius of both the iris and the pupil. The following integro-differential operator is suggested to estimate the triple parameters (x,y,r) [2]:

$$max_{(r,x_0,v_0)} \left| G_\sigma(r) * \frac{\partial}{\partial r} \oint_{r,x_0,v_0} \frac{I(x,y)}{2\pi r} ds \right| \qquad (2.1)$$

where $I(x,y)$ is the image of eye, (x_0, y_0) are the center coordinates, r is the radius, and $G_\sigma(r)$ is a smoothing function such as the Gaussian function. The purpose of the operator is to detect circular edges in the image. After the center coordinates and the radius are found, a similar approach is implemented in order to detect the upper and lower eyelid boundaries.

After the iris region is extracted from the eye image, it is normalized by projecting it from the Cartesian coordinate system to the Polar coordinate system. This transformation is based on [2]:

$$I(x(r,\theta), y(r,\theta)) \rightarrow I(r,\theta) \qquad (2.2)$$

$$x(r,\theta) = (1-r)x_p(\theta) + rx_s(\theta) \qquad (2.3)$$

$$y(r,\theta) = (1-r)y_p(\theta) + ry_s(\theta) \tag{2.4}$$

where x_p, y_p are points on the pupil's boundary and x_s, y_s are points on the sclera boundary. This normalization provides invariance to the iris position and size, and to the dilation of the pupil within the iris.

Then, in order to encode the iris pattern, the normalized image is demodulated to extract its phase information by using quadrature 2-D Gabor wavelets. This is performed by a patch-wise phase quantization of the iris pattern where each bit, in the iris code, is a coordinate of one of the vertices of a logical unit square in the complex plane. Figure 2.1 shows the phase demodulation process. This coordinate is obtained by projecting a given part of the iris onto complex-valued 2-D Gabor wavelets and by evaluating the sign of both the real and imaginary parts of the resulting complex number by the following equations [2]:

$$h_{Re} = 1 \text{ if } \mathrm{Re} \int_\rho \int_\emptyset e^{-iw(\theta_0-\emptyset)} e^{-\frac{(r_0-\rho)^2}{\alpha^2}} . e^{-\frac{(\theta_0-\emptyset)^2}{\beta^2}} I(\rho,\emptyset)\rho d\rho d \quad \emptyset \geq 0 \tag{2.5}$$

$$h_{Re} = 0 \text{ if } \mathrm{Re} \int_\rho \int_\emptyset e^{-iw(\theta_0-\emptyset)} e^{-\frac{(r_0-\rho)^2}{\alpha^2}} . e^{-\frac{(\theta_0-\emptyset)^2}{\beta^2}} I(\rho,\emptyset)\rho d\rho d \quad \emptyset < 0 \tag{2.6}$$

$$h_{Im} = 1 \text{ if } \mathrm{Im} \int_\rho \int_\emptyset e^{-iw(\theta_0-\emptyset)} e^{-\frac{(r_0-\rho)^2}{\alpha^2}} . e^{-\frac{(\theta_0-\emptyset)^2}{\beta^2}} I(\rho,\emptyset)\rho d\rho d \quad \emptyset \geq 0 \tag{2.7}$$

$$h_{Im} = 0 \text{ if } \mathrm{Im} \int_\rho \int_\emptyset e^{-iw(\theta_0-\emptyset)} e^{-\frac{(r_0-\rho)^2}{\alpha^2}} . e^{-\frac{(\theta_0-\emptyset)^2}{\beta^2}} I(\rho,\emptyset)\rho d\rho d \quad \emptyset < 0 \tag{2.8}$$
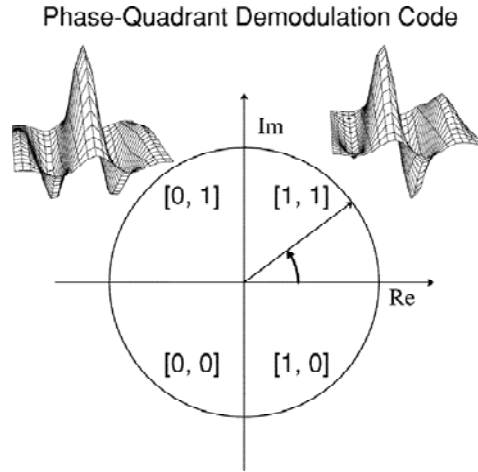
Figure 2.1: The phase demodulation process used to encode iris patterns. [5]

The resulting iris code is a 2048 bits code which is equal to 256 bytes.

In the process of matching, Daugman used Hamming Distance (HD) as a measure of statistical independence between two iris codes. HD is computed as follows [5]:

$$HD = \frac{\|(codeA \otimes codeB) \cap maskA \cap maskB)\|}{\|maskA \cap maskB\|} \tag{2.9}$$

where $\otimes$ is the Boolean XOR operator, codeA and codeB are iris codes, maskA and maskB are used to remove noises such as eyelashes and reflections from the iris codes. HD is used as a measure of dissimilarity such that "0" would indicate a perfect match. Figure 2.2 illustrates the process of Daugman algorithm.

Figure 2.2: Process of Daugman algorithm.

2.2.2. Wildes Algorithm [6]:

The Wildes algorithm for iris-based personal verification can be considered as one of the earliest algorithms in this field. As with the Daugman method for iris localization, Wildes [6] used the first derivative of the image intensity to locate the boundaries of the iris. The contour fitting is performed in two steps. First, a binary edge-map is obtained from the image intensity information by using a gradient-based edge detection. Then, the Hough transform is utilized in order to choose the contour of interest. Given a set of recovered edge points (x_j, y_j), j=1,…,n, the Hough transform can be defined as:

$$H(x_c, y_c, r) = \sum_{j=1}^{n} h(x_j, y_j, x_c, y_c, r) \tag{2.10}$$

where

$$h(x_j, y_j, x_c, y_c, r) = \begin{cases} 1, & \text{if } g(x_j, y_j, x_c, y_c, r) = 0 \\ 0, & \text{otherwise} \end{cases} \tag{2.11}$$

and

$$g(x_j, y_j, x_c, y_c, r) = (x_j - x_c)^2 + (y_j - y_c)^2 - r^2 \tag{2.12}$$

14

Based on Equation (2.11), the contour having a parameter triple (x_c, y_c, r) is selected as the best contour that maximizes the H quantity. Therefore, this contour will have the largest number of edge points. For normalization, Wildes used an image-registration technique by aligning the test and stored images. Thus, both images will have the same scale and orientation. For the process of feature extraction, isotropic band-pass decomposition is performed by using Laplacian of Gaussian (LoG) filters. Such filters are defined as [6]:

$$-\frac{1}{\pi\sigma^4}\left(1 - \frac{\rho^2}{2\sigma^2}\right)e^{-\rho^2/2\sigma^2} \tag{2.13}$$

where σ is the standard deviation of the Gaussian and ρ is the radial distance of a point from the filter's center, respectively. The result of this decomposition is a Laplacian pyramid of four levels. Then, a normalized correlation between the acquired and stored representations is estimated for matching. Figure 2.3 shows the processes involved in the Wildes algorithm.
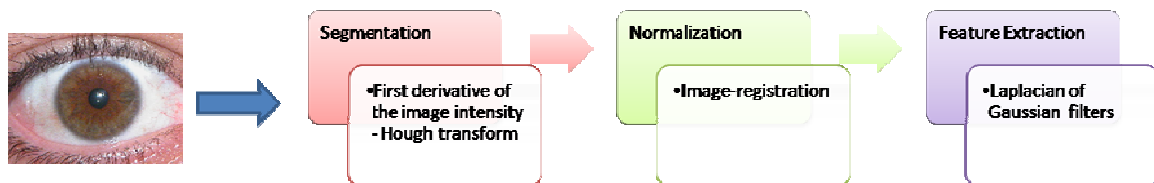
Figure 2.3: Process of Wildes algorithm.

2.2.3. Boles and Boashash Algorithm [7]:

Boles and Boashash used a fine-to-coarse approximation at different resolution levels based on zero-crossing representation of the wavelet transform [7]. When comparing two images, one is considered as a reference and its maximum diameter is calculated. After that, the ratio of the maximum diameter of the reference image to that of the other image is calculated. Using this ratio, the dimensions of the irises of the two images are scaled to have the same diameter. Additionally, the extracted irises are normalized to have the same number of pixels. Then, the normalized iris is used to generate a zero-crossing representation. This is achieved by decomposing a signal into a set of signals at different resolution levels using a dyadic wavelet transform [7]. From these resolution levels, only a few low-resolution levels are chosen in order to reduce the effect of noise on the zero-crossing representation. Figure 2.4 shows a zero-crossing representation of an iris.

Figure 2.4: Zero-crossing representation of an iris. [7]

16

The query iris image for matching is compared with the stored models in the database, and the degree of dissimilarity is computed. The image with the smallest dissimilarity represents a possible match. Many dissimilarity functions can be used. Boles and Boashash [**7**] used the following dissimilarity functions:

$$D_j^{(1)}(f,g) = \frac{\min}{m} \sum_{n=1}^{N} \left| Z_j f(n) - \Gamma Z_j g(n+m) \right|^2, \quad m \in [0, N-1] \qquad (2.14)$$

$$d_j^{(2)}(f,g) = \frac{\min}{m} \frac{\sum_{r=1}^{R_j}\{[\mu_j(r)]_f[\rho_j(r)]_f - \Gamma[\mu_j(r+m)]_g[\rho_j(r+m)]_g\}^2}{\Gamma\sum_{r=1}^{R_j}\left|[\mu_j(r)]_f[\rho_j(r)]_f\right|\left|[\mu_j(r)]_g[\rho_j(r)]_g\right|}, \quad m \in [0, R_j - 1] \qquad (2.15)$$

where g is the query image, f is the candidate model, j is resolution level, Γ is a scale factor, $Z_j f$ and $Z_j g$ are zero crossing representations of signatures f and g, respectively. $[\mu_j]_f$ and $[\rho_j]_f$ are the real and imaginary parts of the representation $Z_j f$. Figure 2.5 shows the process of the Boles and Boashash algorithm.
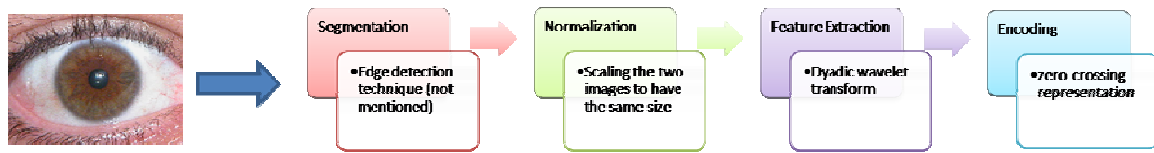
Figure 2.5: Process of Boles and Boashash algorithm.

2.2.4. Ma Algorithm [8]:

Beginning with iris localization, Ma [8] first roughly estimates the position of the pupil region and then accurately calculates the parameters of the two circles of the pupil and iris by using edge detection and the Hough transform. Then, the center of the pupil is approximately estimated by projecting the image in the vertical and horizontal directions. After determining the center of the pupil, the parameters of the pupil's and iris's circles are calculated by using the edge detection technique (Canny operator) and the Hough transform [8].

In order to normalize the extracted portion, the iris is unwrapped, in a counter-clockwise direction, into a rectangular texture block with a fixed size. Then, to enhance the texture details, the iris illumination is carried out. Local sharp variations are used as features to distinguish between two irises. These local variations are captured by constructing a set of 1-D intensity signals from the iris image. The set of signals is obtained by decomposing the normalized image into several signals. This is performed by having a defined number of rows to form a signal. This signal consists of the top 78% section of

18

the normalized image. For each signal, a dyadic wavelet transform is applied in order to locate the position of local sharp variations. Features from the signal are formed by concatenating the position sequence of two consecutive scales. Then, features from all signals are concatenated to form the feature vector. For the matching purpose, the feature vector is converted into a binary feature vector. Then, an exclusive OR operation is used to calculate the similarity between two binary vectors (which represent two iris images). The similarity equation is given by [**8**]:

$$D = \frac{1}{N}\sum_{i=1}^{N}\frac{1}{2L}\sum_{j=1}^{2}\left(Ef_{(i,j)}^1 \otimes Ef_{(i,j)}^2\right) \tag{2.16}$$

where Ef^1 and Ef^2 are two binary feature vectors, $\otimes$ is the exclusive OR operator, L is the length of the binary sequence at one scale, and N is the total number of intensity signals, respectively. Figure 2.6 illustrates the process of the Ma algorithm.
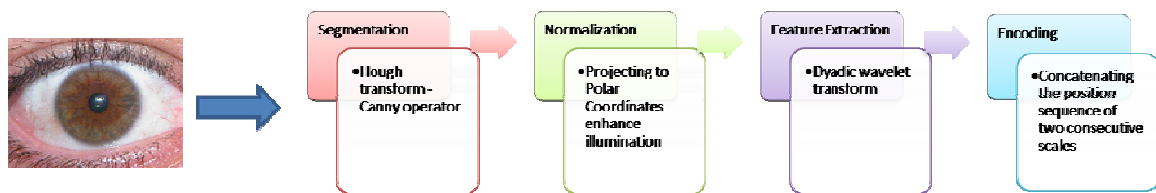
Figure 2.6: Process of Ma algorithm.

2.2.4. Miyazawa Algorithm [9] [10]:

Miyazawa proposed a system that uses phase-based correlation. Phase-based image matching was used for image alignment and the calculation of matching score. This process is carried out by using the Phase-Only Correlation (POC) function. POC is the 2-D inverse Discrete Fourier Transform of the cross-phase spectrum. The POC function of two similar images will give a sharp peak, but the peak will drastically drop if there is no similarity, and so the height of the peak was used as a similarity measure. The translation displacement between two images can be seen by the location of the peak. Because the most meaningful phase information lies in a certain frequency band, a Band-Limited Phase-Only Correlation (BLPOC) function was used. So, in order to match two images, first the translational displacement is aligned between the iris regions, and then the BLPOC function is calculated, and the matching score is considered to be the maximum correlation peak value.

Phase-Only Correlation (POC)

In order to calculate the similarity between two images, Phase-Only Correlation (POC), described by Miyasawa et al. [10], is used. Given two images, one can find POC by first performing the 2D Discrete Fourier Transform on both images. In the frequency domain, the two images can be described as [11]:

$$F(u, v) = A_F(u, v)e^{j\theta_F(u,v)} \tag{2.17}$$

and

$$G(u, v) = A_G(u, v)e^{j\theta_G(u,v)} \tag{2.18}$$

where $A_F(u, v)$ and $A_G(u, v)$ are amplitude components and $\theta_F(u, v)$ and $\theta_G(u, v)$ are the phase components, respectively.

Then, the cross-phase spectrum is performed as [11]:

$$R_{FG}(u, v) = \frac{F(u,v)\overline{G(u,v)}}{|F(u,v)\overline{G(u,v)}|} \tag{2.19}$$

where $\overline{G(u, v)}$ is the complex conjugate of $G(u, v)$.

Equation (2.19) represents the phase correlation in the frequency domain. It is given by [11]:

$$e^{j\{\theta_F(u,v)-\theta_G(u,v)\}} \tag{2.20}$$

Finally, the POC function is calculated by performing the 2D Inverse DFT. The resulting POC function gives a distinct sharp peak if the two images are similar but a low peak otherwise. The peak values are normalized between 0 and 1 (see Figures 2.7- 2.9).
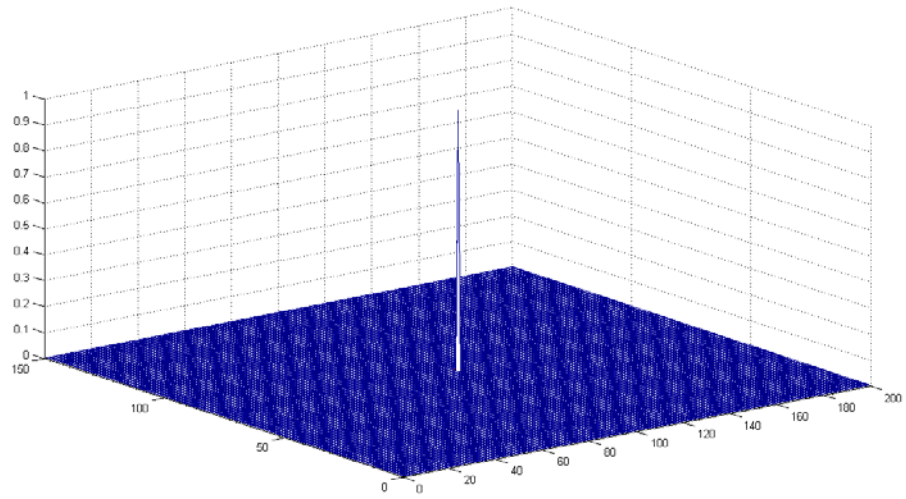
Figure 2.7: Correlation between the same iris image.
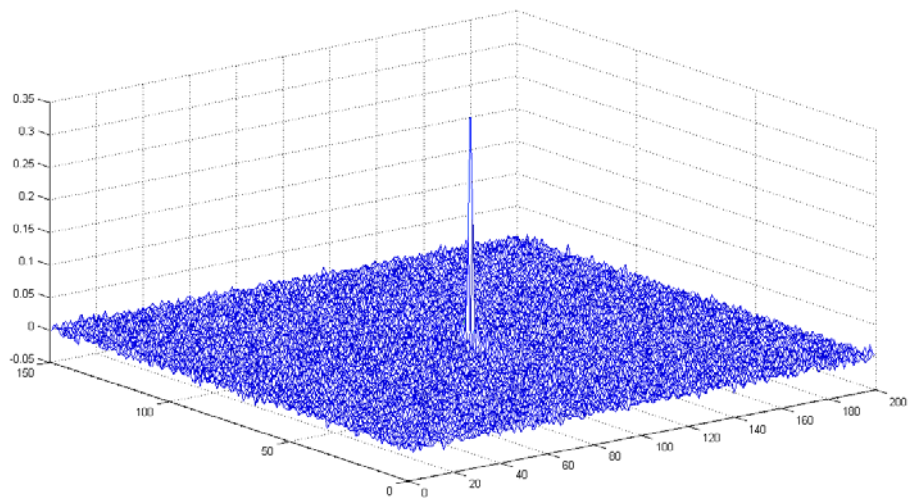
Figure 2.8: Correlation between different iris images of the same person.
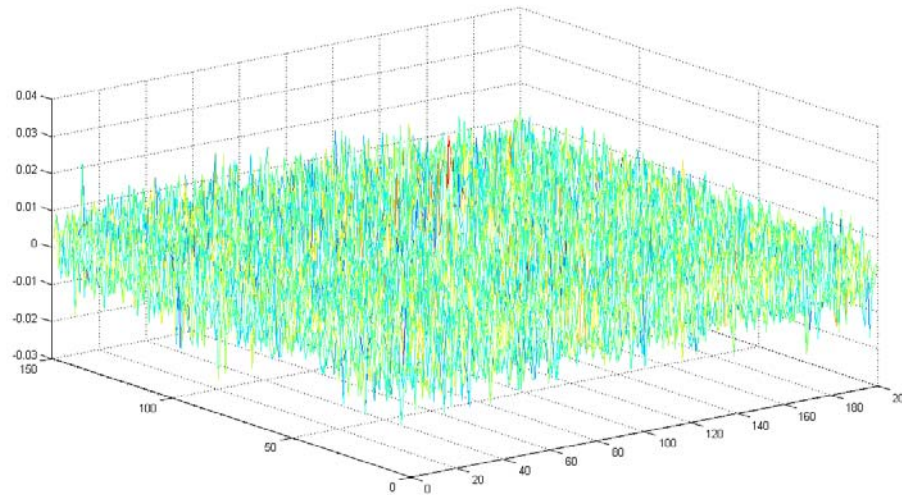
Figure 2.9: Correlation between different iris images of different persons.

Band-Limited Phase-Only Correlation (BLPOC)

Ito et al. [**12**] proposed the Band-Limited POC where only the portion of spectrum that has the most meaningful information is used in the POC calculation. The portion of each image can be calculated as follows:

1. Perform the 2D Discrete Fourier Transform on the image.
2. Compute the projection of both u-axis and v-axis.
3. Compute the mean values of the two projections.
4. Determine the maximum point that is greater than the mean and find the opposite point. This is done in both u-axis and v-axis.

This procedure is described in Figure 2.10 and the resulting portion is shown in Figure 2.11.
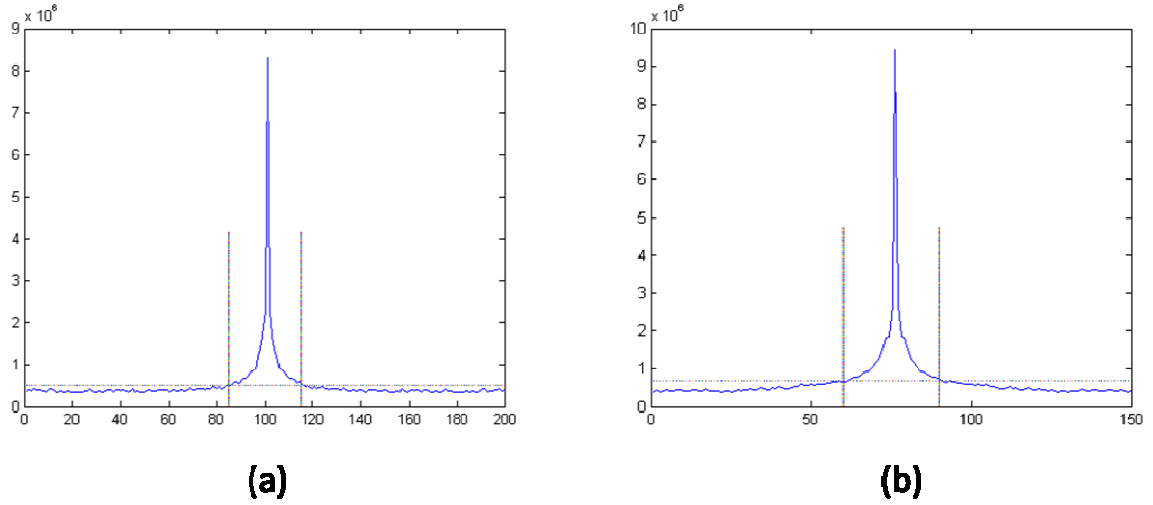
Figure 2.10: (a) u-axis projection. (b) v-axis projection.
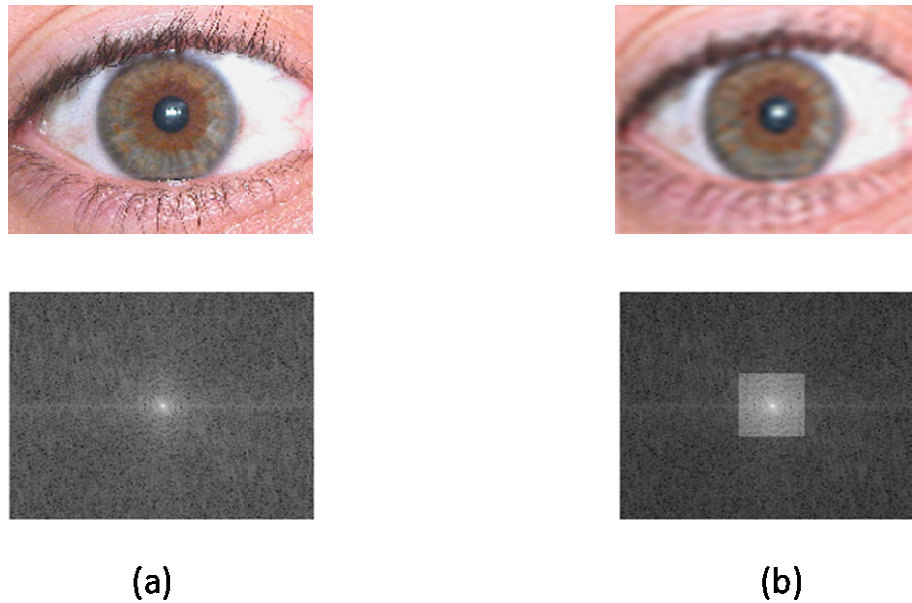
Figure 2.11: (a) Image and its spectrum. (b) Filtered image and the selected portion that contains the most information.

2.3. Other methods used in the literature

Using the fact that a monochrome image can be expressed as a superposition of basis functions and feature coefficients which are independent, Huang et al. [13] proposed the use of independent component analysis (ICA) to estimate the feature coefficients. This was performed by first calculating independent components on small windows NxN for the normalized iris image and then estimating the ICA coefficients for these windows. Then, the ICA coefficients were quantized in order to reduce their size. To estimate the center of each class (which represents a person), a competitive learning mechanism was used. Average Euclidean Distance (AED) was used in the process of the matching

between two given iris images. Ma et al. [14] defined a new spatial filter to capture local textures of the normalized iris image. The new filter is a Gaussian modulated by a circularly-symmetric sinusoidal function, which differentiates it from Gabor filters that are modulated by orientated sinusoidal functions. Features were extracted from the region having the most discriminating features, known as the region of interest (ROI). Because the most useful information, in an iris image, is distributed in a specific frequency range, the defined filters were used in two different channels. The two filtered images were divided in small blocks, and from each block the mean and the average absolute deviation were calculated and used as features. Features from all blocks are arranged in a 1-D feature vector. To reduce the dimensionality of the feature vector, Fisher Linear Discriminant (FLD) was used. The nearest center classifier was used for the purpose of matching [14].

Son et al. [15] proposed a method to extract features by applying the 2-D Daubechies wavelet transform to decompose the image into four sub-images. The low frequency sub-image is decomposed recursively, and the process is terminated by reaching a lowest frequency sub-image that can be used for discrimination. The authors used three-level decomposition. However, if the image size is higher, then higher decomposition levels are needed. After getting the feature vector of the iris, the dimension of the vector is reduced by using Direct Linear Discriminant Analysis (DLDA). This step aims to decrease the dimensionality and increase the efficiency. Support Vector Machines (SMVs) were utilized in matching different iris images. Gaussian kernels were used in the proposed architecture.

Zhang et al. [16] introduced an approach that used feature fusion of global and local features of the iris image. Global features are known to be insensitive to shift changes and noise, easy to compute, and have a small intra-class variance and a large inter-class variance. The local features are variant in intra-class and have no effects on the inter-class. To extract the global features, the *Log-Gabor wavelet* was used. From the transformed image, the statistical values of the amplitude are used as global features. These statistical values represent the mean and average absolute deviations and they are taken with four orientations and frequency levels. Global features are classified by using the weighted Euclidean distance. For the extraction of local features, the Log-Gabor wavelet filter was applied and the features were extracted from the intermediate frequency levels. This is performed by taking the filtered image and encoding its amplitude into a binary form. Hamming distance was used for the classification of local features. The process of fusion begins with the global features. If the weighted Euclidean distance gives a value not between the two thresholds (t_a, t_b), then local features will not be considered. Otherwise, local features will be processed as discussed above.

Khan et al. [17] used Haar wavelets in the process of extracting the features from the normalized iris image. Khan et al. preferred the use of Haar wavelets over Gabor wavelets because the former have a slightly better recognition rate. Furthermore, computing Haar wavelets is faster and simpler than computing Gabor wavelets. For the comparison of two iris images, Hamming distance was used.

Ives et al. [18] proposed an iris identification using histogram analysis. First, the histogram of the segmented iris image was calculated. A 5-tap averaging filter was used

to reduce noise. All histograms were normalized to make their peak value equal to 1. Finally, the peak was shifted to a grayscale value of 128 in order to adjust the differences of illumination between different images. The Du measure was used to compare two images [18]. Du measure yields an integer that represents the closeness of two vectors (which are iris's features in this case). Two vectors are said to be close, when the Du measure yields small values.

Ko et al. [19] introduced a method that utilize cumulative sum for analyzing changes in the gray values of the normalized iris image. First, the normalized image was divided into a number of cells of dimensions $m_x n$, and for each cell the average gray value is calculated. These gray values were used in turn to calculate the cumulative sum by grouping the cells horizontally and vertically and calculating the cumulative sum over each group. Then, the iris codes were generated by analyzing the changes of gray values in the iris patterns. For the process of matching two iris images, the Hamming distance was used.

Conti et al. [20] suggested a technique of iris recognition that uses micro-features of the iris. Such micro-features are nucleus, collarette, valleys, and radius [20], Figure 2.12 illustrates them. The nucleus is extracted from the zone inside the contour of the pupil that does not respect a circular symmetry. The distance of horizontal, vertical and diagonal direction was calculated by using the Bresenham's algorithm. The collarette was extracted from the zone between the contours of the pupil and the iris. In order to detect the collarette, a contrast variation was applied to highlight the different intensities. Applying a sigmoid using the maximum and minimum values of the image intensity

yields the contrast variation. Image regions having the same gray level were labeled. Considering all regions, if the boundary intensity level was less than a specific threshold, then they were considered to belong to the collarette. The valley was extracted from the region over the zone specified by the collarette. The zones with different intensities were detected by applying a contrast variation to the circular crown of the iris. If a zone has greater intensity than the base threshold, then it should be individualized. Zones, having the same intensity, are labeled. The positions, in the Cartesian system, of the specified points were considered as the micro-feature of the valley. Radius micro-feature can be considered as the intensity variation toward the white color in comparison to the iris background. It can be extracted from the zone between the collarette and the edge between the iris and the sclera. After the four micro-features are extracted, a translation between template models and input models is performed. The matching is done by calculating the number of corresponding micro-features between the two iris images.
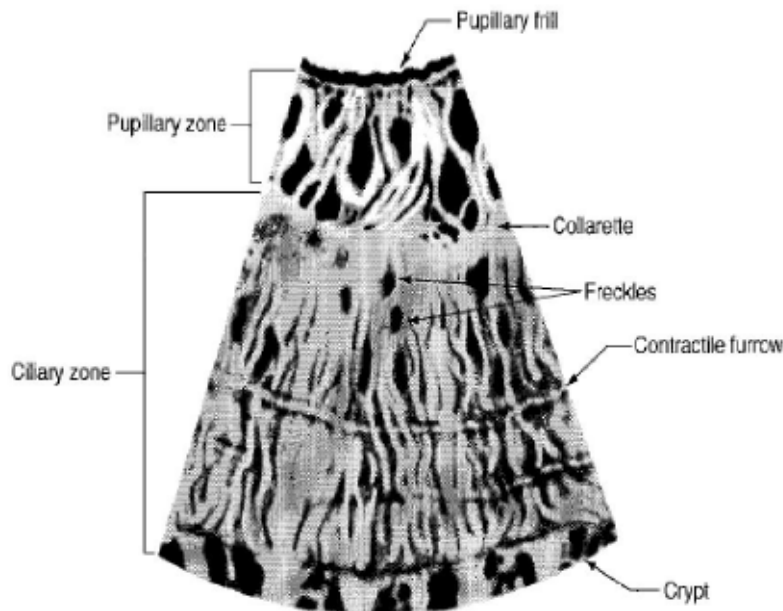
Figure 2.12: Illustration of the micro-features of the iris. [20]

Narote et al. [21] proposed a technique for iris identification based on the Dual Tree Complex Wavelet Transform (DTCWT). DTCWT is a redundant complex wavelet transform that was designed by Kingsbury [22]. Complex wavelets are better than standard discrete wavelet transform in terms of shift sensitivity, directionality and phase information. Two parallel trees were used with odd-length filters in one tree and even-length in the other. A four level DTCWT was applied to the normalized iris image in order to extract the features of the iris. Two linear phase biorthogonal filter sets, with odd and even lengths, were used alternately for the dual filter tree. The coefficients of the filtered images were used to construct the iris code. For the purpose of matching between two iris images, Hamming distance was used.

Anna et al. [23] utilized both wavelet transform and neural network for iris recognition. They used Wavelet Probabilistic Neural Network (WPNN), which combines wavelet neural network and probabilistic neural network. The WPNN consisted of four layers, the feature layer, the wavelet layer, the Gaussian layer, and the decision layer. In order to extract feature, vertical projection of the normalized iris image was performed to obtain a 1-D energy signal. Each node in the wavelet layer is equivalent to a multidimensional wavelet. Boosting was chosen as the learning algorithm to train the WPNN and adjust its parameters in order to get the best accuracy for the classifier.

Sudha et al. [24] proposed a method for iris recognition based on edge maps and Hausdorff distance measure. The Hausdorff distance is the distance between two sets of points. It gives a measure of the dissimilarity between the sets' points. Pixel sets that represent the coordinates of feature pixels are considered as the point sets when the Hausdorff distance is measured between images. To compare closely matching portions of the image effectively, a modified measure called Partial Hausdorff Distance (PHD) was used. First, the linear patterns of the iris are captured by using the Canny edge detection technique. Then, the images are divided into non-overlapping blocks of the same size. The Partial Hausdorff Distance is computed between the significant blocks (where all pixel values are not zero) of the same position in the two images. The result is a value that determines the dissimilarity between the two images.

Szewczyk [25] proposed a method for iris identification based on the use of reverse biorthogonal wavelets in the phase of feature extraction. After reverse biorthogonal wavelets were applied to decompose the image, the median of the resultant coefficient

was computed. In order to get the iris code, coefficients that are less than the median were set to 0 while others were set to 1. Hamming distance was used for the purpose of matching.

Krichen et al. [26] utilized the color information in order to classify iris images that were acquired under normal light illumination. First, the number of colors of the normalized iris reference image was reduced by using the minimum variance quantization. The corresponding color map of the compressed image was obtained. Query iris image was processed by using the color map obtained from the reference image. This was done by assigning each color in the map into nearest color in the query image using RGB color space. Then, the distribution of the corresponding pixel positions were compared by using the modified Hausdorff Distance [26].

CHAPTER THREE

HYPERCOMPLEX (QUATERNION) REPRESENTATION

3.1. Quaternion Numbers

Quaternion numbers were first proposed by Sir William Hamilton in 1843. They have several applications, such as mechanics in 3D space and 3D rotations. One of their appealing applications is their use to represent and process color images in a holistic manner rather than each color separately. Quaternion numbers are extensions of the regular complex numbers to higher dimensions. Complex numbers are also extensions of the real numbers, and they take the following form:

$$c = a + bi \tag{3.1}$$

where i is an imaginary number and defined by

$$i^2 = -1 \tag{3.2}$$

Definition [**27**]: A quaternion is defined as follows:

$$q = a + bi + cj + dk \tag{3.3}$$

where i, j, and k are imaginary numbers, and a, b, c, and d are real numbers. Another possible representation is given as follows:

$$\mathbb{Q} = \{a + bi + cj + dk \mid a, b, c, d \in \mathbb{R}\} \tag{3.4}$$

where $\mathbb{Q}$ is Quaternion space, and $\mathbb{R}$ is real numbers. Hence,

$$\mathbb{R} \subseteq \mathbb{C} \subseteq \mathbb{Q} \qquad (3.5)$$

where $\mathbb{C}$ is complex numbers.

3.2. Properties of Quaternion Numbers

Quaternions have several properties. Some of these properties, of interest to our proposed work, are covered in this section.

Given a quaternion number q:

$$q = a + bi + cj + dk \qquad (3.6)$$

Property 1:

$$ijk = i^2 = j^2 = k^2 = -1 \qquad (3.7)$$

Property 2:

$$jk = i, \ kj = -i \qquad (3.8)$$

$$ki = j, \ ik = -j \qquad (3.9)$$

$$ij = k, \ ji = -k \qquad (3.10)$$

From Equations (3.8)-(3.10), it is clear that the multiplication is not commutative in Quaternions. This is an important property that will affect the design of the Quaternion

Fourier Transform (QFT) and the Quaternion convolution (QC) as will be shown in the next sections.

Property 3: A quaternion with a zero real part is called a *pure quaternion*:

$$q = 0 + bi + cj + dk \tag{3.11}$$

Property 4: The *conjugate* of a quaternion is defined by negating its imaginary parts[1]:

$$\overline{q} = \overline{a + bi + cj + dk} = a - bi - cj - dk \tag{3.12}$$

Property 5: The *modulus* or *magnitude* of a quaternion is defined by:

$$|q| = \sqrt{a^2 + b^2 + c^2 + d^2} \tag{3.13}$$

---

[1] Note that the conjugate of Quaternions can be in many forms. These forms consist of different combinations of negative imaginary numbers. In this definition, all are negatives.

3.3. 2-D Quaternion Fourier Transform

3.3.1. Regular 2-D Quaternion Fourier Transform

The regular 2D Fourier Transform is defined as [11]:

$$I(u,v) = \int_{-\infty}^{\infty} \int_{-\infty}^{\infty} I(x,y) e^{-iux} e^{-ivx} \, dxdy \tag{3.14}$$

where I(x, y) is the spatial-domain representation of the image, x and y are the spatial coordinates, I(u, v) is the frequency-domain representation of the image, and u and v are the frequency coordinates. Because complex numbers are commutative in multiplication, Equation (3.14) has the following equivalent representations:

$$I(u,v) = \int_{-\infty}^{\infty} \int_{-\infty}^{\infty} e^{-iux} e^{-ivx} I(x,y) \, dxdy \tag{3.15}$$

$$I(u,v) = \int_{-\infty}^{\infty} \int_{-\infty}^{\infty} e^{-iux} I(x,y) e^{-ivx} \, dxdy \tag{3.16}$$

3.3.2. Types of 2-D Quaternion Fourier Transform

Due to the fact that Quaternion numbers are not commutative in multiplication, there are different types of Quaternion Fourier Transforms (QFT). Pei et al. [28] defined three QFT types. These are two-side, left-side and right-side QFTs, respectively.

The two-side QFT (Type 1) is defined by [28]:

$$H_{(q1)}(u,v) = \int_{-\infty}^{\infty} \int_{-\infty}^{\infty} e^{-\mu_1 ux}.h(x,y).e^{-\mu_2 vy}.dxdy \qquad (3.17)$$

where h(x,y) is the input Quaternion image, μ_1 and μ_2 are two pure unit Quaternions, orthogonal to each other, and w and v are the spatial frequencies in x and y directions, respectively.

Similarly, the left-side QFT (Type 2) is defined by [28]:

$$H_{(q2)}(u,v) = \int_{-\infty}^{\infty} \int_{-\infty}^{\infty} e^{-\mu_1(ux+vy)}.h(x,y).dxdy \qquad (3.18)$$

Also, the right-side QFT (Type 3) is defined by [28]:

$$H_{(q3)}(u,v) = \int_{-\infty}^{\infty} \int_{-\infty}^{\infty} h(x,y).e^{-\mu_1(ux+vy)}.dxdy \qquad (3.19)$$

Pei et al. [28] also defined the inverse representations of these QFTs as follows:

$$h(x,y) = \frac{1}{4\pi} \int_{-\infty}^{\infty} \int_{-\infty}^{\infty} e^{-\mu_1 ux}.H_{(q1)}(u,v).e^{-\mu_2 vy}.dudv \qquad (3.20)$$

$$h(x,y) = \frac{1}{4\pi} \int_{-\infty}^{\infty} \int_{-\infty}^{\infty} e^{-\mu_1(ux+vy)}.H_{(q2)}(u,v).dudv \qquad (3.21)$$

$$h(x, y) = \frac{1}{4\pi} \int_{-\infty}^{\infty} \int_{-\infty}^{\infty} H_{(q3)}(u, v) . e^{-\mu_1(ux+vy)} . du dv \qquad (3.22)$$

Similarly, the discrete two-side (Type 1) Quaternion Fourier Transform (DQFT) is defined by [28]:

$$H_{(q1)}(u, v) = \sum_{x=0}^{M-1} \sum_{y=0}^{N-1} e^{-\mu_1 2\pi\left(\frac{ux}{M}\right)} . h(x, y) . e^{-\mu_2 2\pi\left(\frac{vy}{N}\right)} \qquad (3.23)$$

where M and N are the size of the image.

Left-side DQFT (Type 2) is defined by:

$$H_{(q2)}(u, v) = \sum_{x=0}^{M-1} \sum_{y=0}^{N-1} e^{-\mu_1 2\pi\left(\left(\frac{ux}{M}\right)+\left(\frac{vy}{N}\right)\right)} . h(x, y) \qquad (3.24)$$

Right-side DQFT (Type 3) is defined by:

$$H_{(q3)}(u, v) = \sum_{x=0}^{M-1} \sum_{y=0}^{N-1} h(x, y) . e^{-\mu_1 2\pi\left(\left(\frac{ux}{M}\right)+\left(\frac{vy}{N}\right)\right)} \qquad (3.25)$$

It is well known that the efficient algorithm for computing the Fourier Transform (called Fast Fourier Transform FFT) of an MxN image has a complexity of [28]:

$$MN.log_2MN \tag{3.26}$$

QFT can use two FFTs in its implementation. Thus complexity of three types of QFT is:

$$2MN.log_2MN \tag{3.27}$$

Thus, both FFT and QFT have complexity equal to:

$$O(MN.log_2MN) \tag{3.28}$$

3.3.3. Implementation of 2-D Discrete Quaternion Fourier Transform

Ell and Sangwine [29] proposed a method to calculate the 2-D Discrete Quaternion Fourier Transform by using regular FFTs. This is achieved by decomposing the quaternion representation into two perpendicular planes in a four-dimensional space, which intersect only at the origin. This decomposition, called symplectic form, is based on the Cayley-Dickson form. In this form, a quaternion is defined recursively as a generalized complex number whose "real" and "imaginary" components are themselves complex numbers. So, any quaternion:

$$q = a + bi + cj + dk \tag{3.29}$$

can be rewritten in the Cayley-Dickson form as [29]:

$$q = A + Bj \tag{3.30}$$

where $A = a + bi$ and $B = c + di$. In this symplectic form, A is called the simplex part and B is called the perplex part, respectively.

Ell and Sangwine [**29**] described the steps to implement a quaternion Fourier transform. Let μ_1 and μ_2 be two pure unit Quaternions, orthogonal to each other. Then the implementation of the 2-D Discrete Quaternion Fourier Transform is carried out as follows [**29**]:

1. First, the image f(x,y) is decomposed into its symplectic components as:

$$f(x,y) = f_1(x,y) + f_2(x,y)\mu_2 \tag{3.31}$$

where each $f_i \in (1, \mu_1)$ plane.

2. Then, each symplectic component is expanded as:

$$f_i(x,y) = r_{i,1}(x,y) + r_{i,2}(x,y)\mu_1 \tag{3.32}$$

where each $r_{i,j}(x,y)$ is an image of scalars.

3. After that, equivalent complex images are constructed as :

$$f'_i(x,y) = r_{i,1}(x,y) + r_{i,2}(x,y)i \tag{3.33}$$

4. Next, two 2-D complex FFTs of $f'_i(n,m)$ are performed to obtain:

$$F'_i[u,v] = R'_{i,1}[u,v] + R'_{i,2}[u,v]i \tag{3.34}$$

5. Then, simplex and perplex parts are constructed as:

$$F_i[u,v] = R'_{i,1}[u,v] + R'_{i,2}[u,v]\mu_1 \tag{3.35}$$

6. Finally, the full quaternion in symplectic form is constructed as:

$$F[u, v] = F_1[u, v] + F_2[u, v]\mu_2 \tag{3.36}$$

Figure 3.1 shows an image and its spectrum in the frequency domain, using the three types of 2D DQFT.
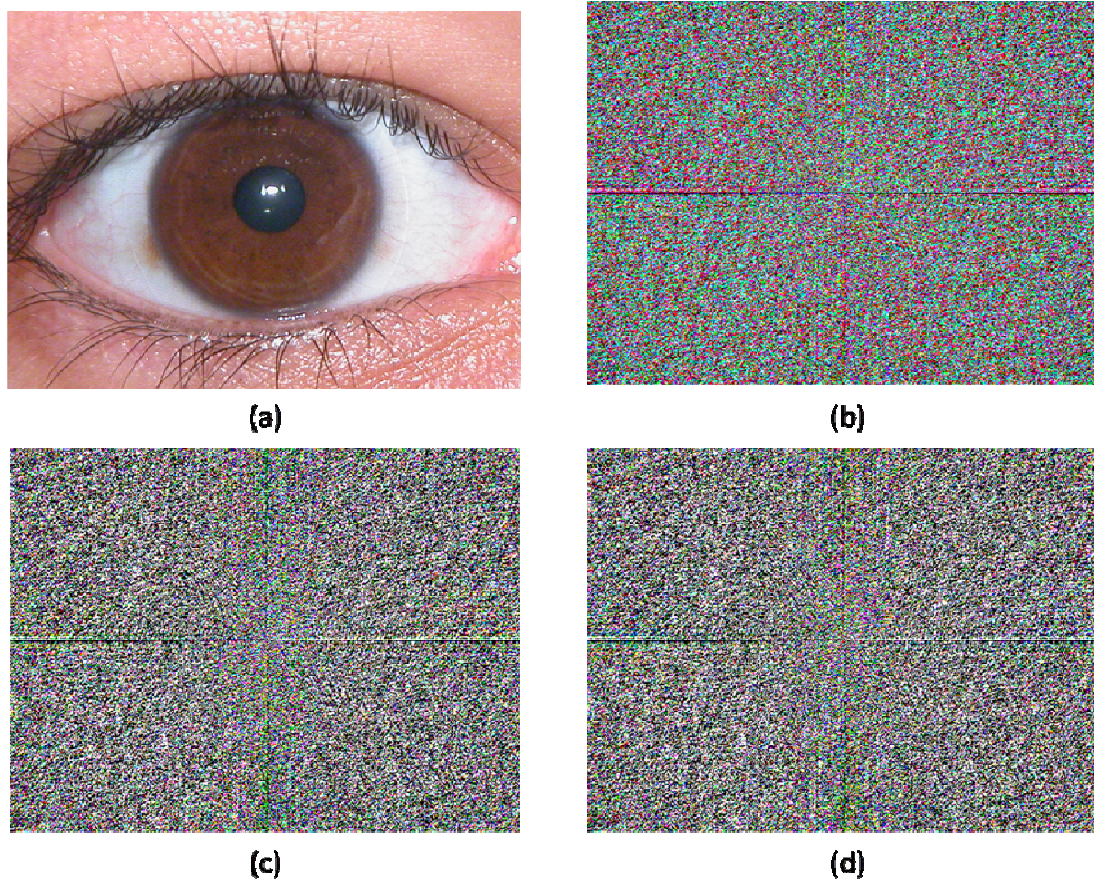
Figure 3.1: Spectrum of transformed Quaternion image. (a) Input image. (b) 2-side QFT. (c) Left-side QFT. (d) Right-side QFT.

3.4. Quaternion Convolution

Because Quaternion numbers are not commutative in multiplication, there are two types of Quaternion convolution (QCV), namely: one-side and two-side convolution. The one-side Quaternion convolution is defined by [28]:

$$g(x,y) = f(x,y) *_q h(x,y) = \int_{-\infty}^{\infty} \int_{-\infty}^{\infty} f(x-\tau, y-\eta).h(\tau,\eta).d\tau d\eta \qquad (3.37)$$

where f(x,y) is the input image and h(x,y) is the filter.

The two-side quaternion convolution is defined by [28]:

$$g(x,y) = f(x,y) *_q \{h_1(x,y), h_2(x,y)\}$$
$$= \int_{-\infty}^{\infty} \int_{-\infty}^{\infty} h_1(\tau,\eta)f(x-\tau, y-\eta).h_2(\tau,\eta).d\tau d\eta \qquad (3.38)$$

where h2(x,y) is the second filter applied, along with filer h1(x,y), to the image f(x,y). A common and fast method of convolution for real and complex images is to perform Fourier Transform (FT) on the image and the filter. Then, scalar multiplication is performed in the frequency domain, followed by the inverse FT of the product. This fast implementation is written as [11]:

$$ImConv = IFT(FT(Image).FT(Filter)) \qquad (3.39)$$

Pie et al. [28] utilized the QFT implementation described in Section 3.3, to implement two types of Quaternionic convolutions: one-side and two-side. The relationships between different types of QFT and quaternion convolutions were provided therein [28] as shown in Table 3.1. From the Table 3.1, it can be seen that achieving one-side QCV requires the use of three QFTs, while two-side QCV requires six QFTs. Thus, the complexity of one-side QCV is

$$6MN.log_2MN \tag{3.40}$$

And the complexity of two-side QCV is

$$12MN.log_2MN \tag{3.41}$$

Hence, both FFT and QFT have complexity equal to:

$$O(MN.log_2MN) \tag{3.42}$$

Relation between 1-side QCV and QFT-1	$G_{(q1)}(w,v) = F_{a(q1)}(w,v)Q^{r,j}\big(H_{(q1)}(w,v)\big) + F_{a(q1)}(w,-v)Q^{j,k}\big(H_{(q1)}(w,v)\big) +$ $F_{b(q1)}(w,-v)jQ^{r,j}\big(H_{(q1)}(-w,v)\big) + F_{b(q1)}(w,v)jQ^{j,k}\big(H_{(q1)}(-w,v)\big),$ where $f_a(x,y) = f_r(x,y) + f_i(x,y)i,$ $f_b(x,y) = f_j(x,y) + f_k(x,y)i.$
Relation between 1-side QCV and QFT-2	$G_{(q2)}(w,v) = F_{a(q2)}(w,v)H_{(q2)}(w,v) + F_{b(q2)}(w,v)\cdot jH_{(q2)}(-w,-v),$ where $f_a(x,y) = f_r(x,y) + f_i(x,y)i,$ $f_b(x,y) = f_j(x,y) + f_k(x,y)i.$
Relation between 1-side QCV and QFT-3	$G_{(q3)}(w,v) = F_{(q3)}(w,v)H_{a(q3)}(w,v) + F_{(q3)}(-w,-v)\cdot jH_{d(q3)}(w,v),$ where $h_a(x,y) = h_r(x,y) + h_i(x,y)i,$ $h_d(x,y) = h_j(x,y) - h_k(x,y)i.$
Relation between 2-side QCV and QFT-2	$G_{(q2)}(w,v) = F_{a(q2)}(w,v)H_{3(q2)}(w,v) + \overline{F_{a(q2)}(-w,-v)}\,jH_{4(q2)}(w,v)$ $F_{b(q2)}(w,v)jH_{5(q2)}(-w,-v) + \overline{F_{b(q2)}(-w,-v)}\,jH_{6(q2)}(-w,-v),$ where $f_a(x,y) = f_r(x,y) + f_i(x,y)i,$ $f_b(x,y) = f_j(x,y) + f_k(x,y)i,$ $h_3(x,y), h_4(x,y), h_5(x,y), h_6(x,y),$ are defined as (68)

Table 3.1: Relationships between different types of QFT and QCV. [28]

3.5. Quaternion Representation of Images

A pure quaternion is used to represent an image in a holistic manner by using the quaternion form. Decomposing the color components of the image and assigning each of them to an imaginary part of the quaternion would yield such holistic representation. In this research, the Red-Green-Blue (RGB) color space is used. Figure 3.2 illustrates the approach adopted to represent RGB color image by using the quaternion form.
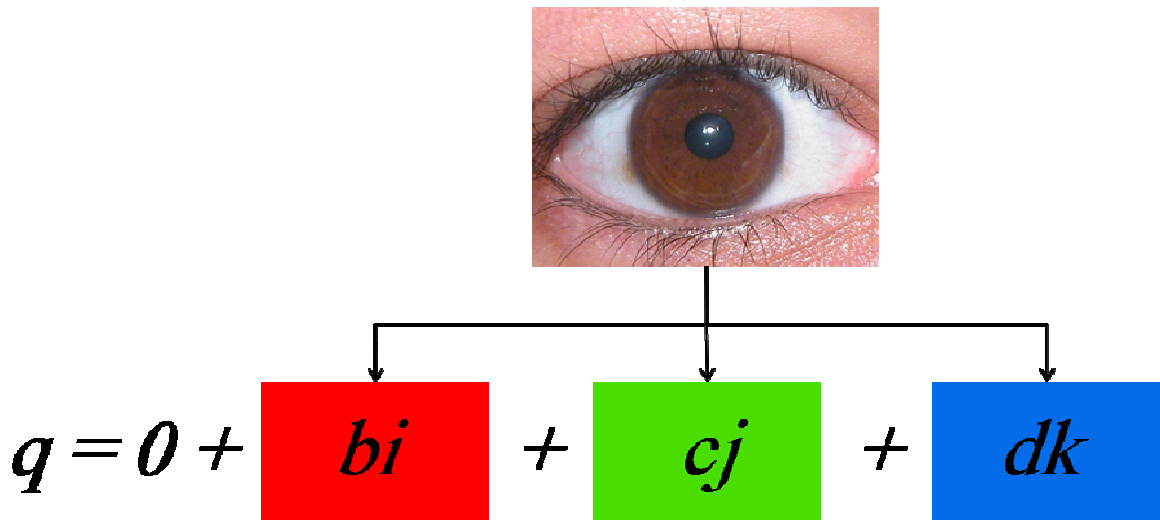

Figure 3.2: Quaternion representation of an image.

3.6. Spatio-Chromatic Representation

McCabe et al. [**30**] proposed a method to capture spatio-chromatic information of images. The chromatic information consists of the hue and saturation components. Figure 3.3 illustrates the hue and saturation components. The hue component represents the

variation in colors, and it varies along the outer circumference of the cone in Figure 3.3. The saturation component defines the saturation of the hue component, and saturation is represented by the distance from the center of a circular cross-section of the cone.
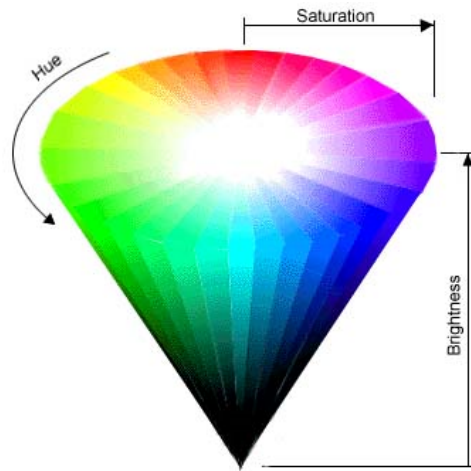
Figure 3.3: Hue and saturation components.

The method proposed by McCabe et al., based on one regular complex FT, can be described as follows [30]:

1. Transform the color space into CIE 1976 chromaticity $\acute{u}\acute{v}$ space [31]. This is done by first transforming the image into XYZ.

2. Rotate $\acute{u}\acute{v}$ values by $\pi/30$ radian in order to align the $\acute{u}$ axis with the red-green orientation and the $\acute{v}$ axis with the yellow-blue orientation.

3. Perform the regular 2D Fourier Transform as:

$$U(u,v) + jV(u,v)$$

$$= \sum_{x=-\frac{N}{2}+1}^{N/2} \sum_{y=-\frac{N}{2}+1}^{N/2} [ú(x,y) + jv́(x,y)].\exp[-2\pi j(ux + vy)/N] \qquad (3.43)$$

where NxN is the size of the image, and $[ú(x,y) + v́(x,y)]$ is the complex chromaticity coordinates at the spatial point (x,y).

CHAPTER FOUR

GABOR WAVELETS

4.1. Introduction

A well-known shortcoming of signal analysis in the frequency domain using the FT representation is the inability to simultaneously capture the time and frequency information of signals. Only information about the spectral component of the signal is provided. This is shown in Figure 4.1(b). It is clear that at any frequency point, space (time) components cannot be defined. By duality, this holds true for the space domain, where the temporal location of the signal can be found, while the information of the frequency is not provided. Figure 4.1(a) illustrates this effect. To remedy this problem, Gabor [32] applied a method, rooted in quantum physics and called the Heisenberg uncertainty principle, to analyze signals in both time and frequency domains. He proposed a solution by multiplying a sinusoid with a Gaussian envelope. The basic Gabor function is defined as [32]:

$$\Psi(t) = e^{-\alpha^2(t-t_0)^2} e^{j(2\pi f_0 + \phi)} \tag{4.1}$$

Figures 4.1(c) and 4.1(d) show the result of using a Gabor function with a fixed Gaussian envelope and different Gaussians, respectively. It is clear that for any frequency point the information of space is available, and vice-versa.
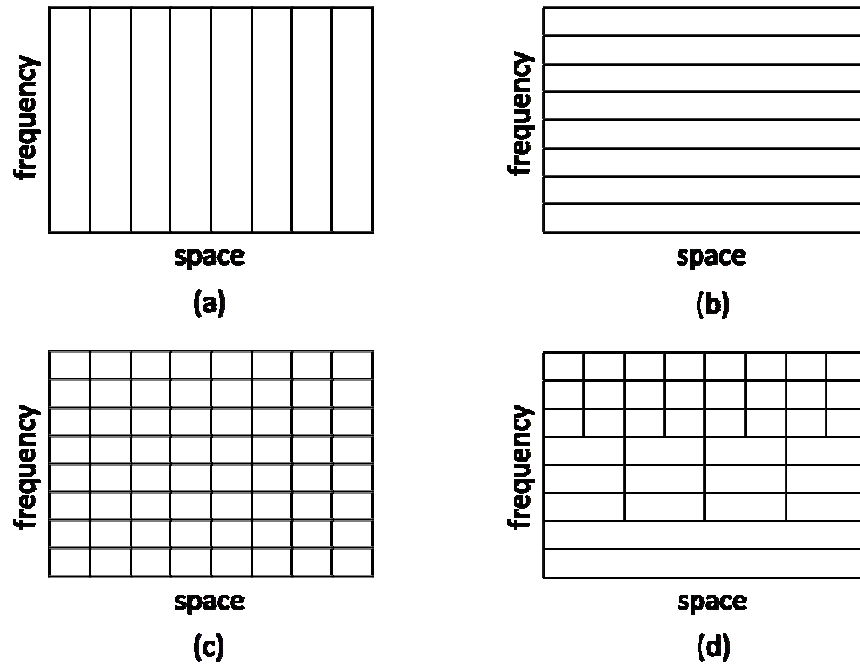
Figure 4.1: Transformations between frequency and space domains. (a) Signal in space domain. (b) Signal in frequency domain. (c) and (d) space-frequency analysis using Gabor functions.

To enable the use of Gabor wavelets in image processing, it was extended into two dimensions. This extension allowed 2D signals to be analyzed in different orientations and frequencies.

In the literature, Gabor filters have been used in image processing for three tasks [33]:

- Texture information analysis.

- Nearly periodic features enhancement such as fingerprint ridges.

- Feature analysis and extraction.

4.2. Gabor Filters

It is important to achieve representations of the iris that are invariant for scale, rotation, and size. In this way, the effect of a slight tilt of the face or the camera, or variation of distances from the camera, will be minimized. This can be achieved by decomposing the image into different frequency and orientation channels. Such multi-resolution decomposition can be realized effectively by using filter-banks that are constructed with Gabor wavelets. Gabor filters are multi-resolution band-pass filters capable of achieving optimum joint spatial/frequency localization. In addition, they can imitate the behavior of simple cells in the visual cortex in the human and mammalian visual system.

In its essence, a Gabor wavelet is a Gaussian that is modulated by a complex sinusoid. A 2D Gabor can be defined as follows:

$$g(x,y) = \frac{1}{2\pi\sigma_x\sigma_y}\exp\left\{-\frac{1}{2}\left[\frac{x^2}{\sigma_x^2}+\frac{y^2}{\sigma_y^2}\right]\right\}\exp\{j2\pi(ux+uy)\} \qquad (4.2)$$

where σ_x and σ_y are the space constants of the Gaussian envelope along the x and y axes. They also characterize the bandwidth of the filter. The frequency term can be found by:

$$F = \sqrt{u^2 + v^2} \qquad (4.3)$$

This can be represented in the frequency domain as:

$$G(u,v) = \exp\left\{\frac{1}{2}\left[(\sigma_x[u-U])^2 + (\sigma_y[v-V])^2\right]\right\} \qquad (4.4)$$

It was found that the choice $\sigma_x = \sigma_y = \sigma$ is sufficient for most applications [**34**]. Thus, Equation (4.2) is reduced to:

$$g(x,y) = \frac{1}{2\pi\sigma^2}\exp\left\{-\frac{1}{2}\left[\frac{x^2+y^2}{\sigma^2}\right]\right\}\exp\{j2\pi(Ux+Vy)\} \qquad (4.5)$$

Three parameters should be chosen carefully in order to achieve the best performance. These are frequency, size, and orientation, respectively.

Figure 4.2 shows a set of Gabor functions in the spatial domain with six orientations and two sizes. Each row has six orientations, incremented by 30 degrees from the previous one. Figure 4.3 shows the results of convolving an image with the Gabor functions shown in Figure 4.2. The effect of different sizes can be clearly seen on each row. Furthermore, the different angles of the filter have the effect of selecting edges oriented at a specific direction.
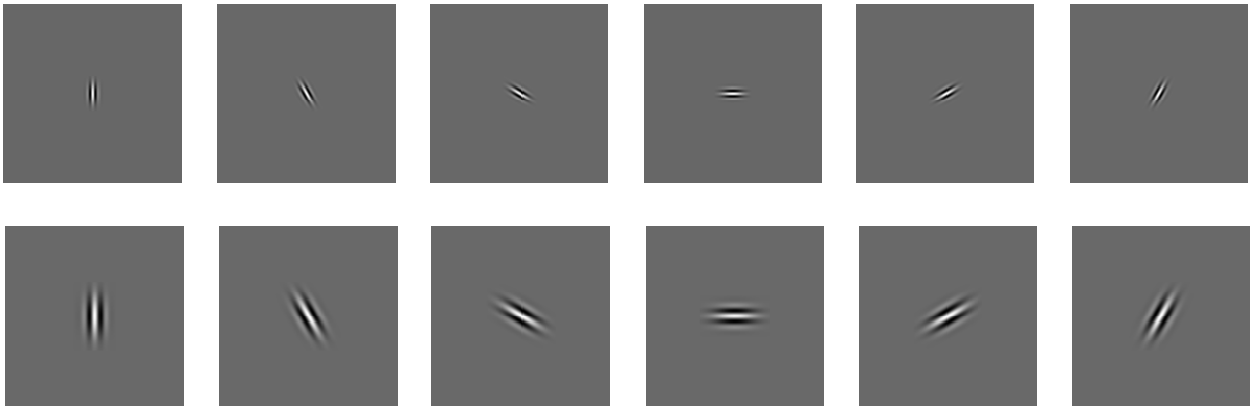
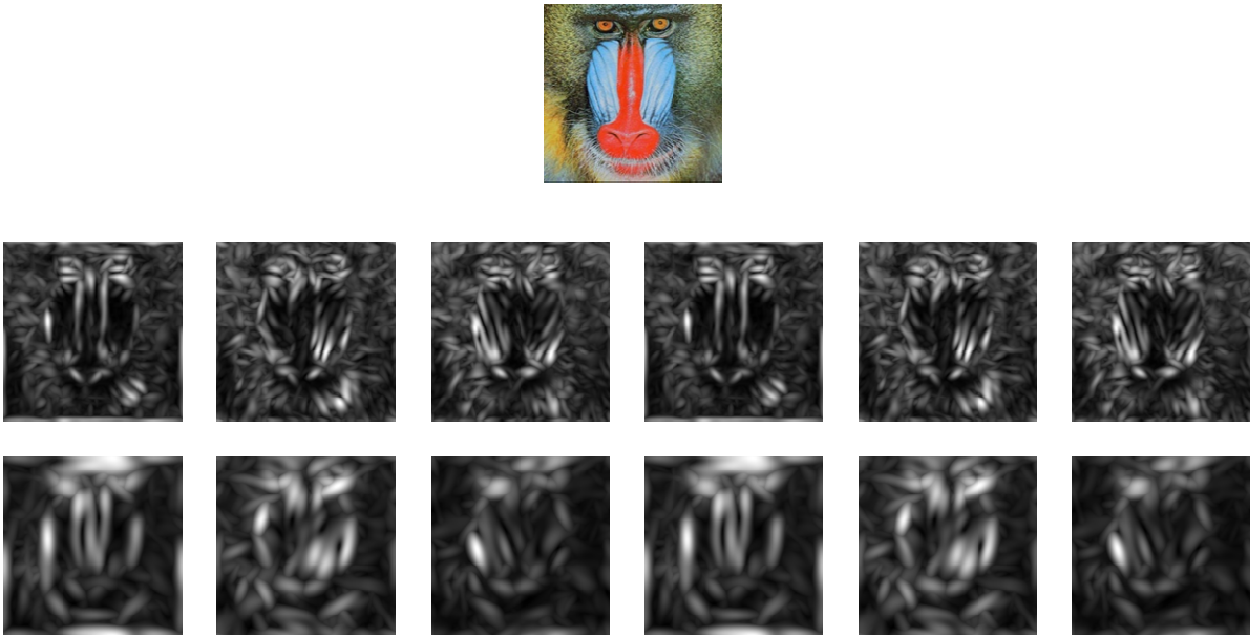Figure 4.2: Set of Gabor functions with 8 orientations and 2 sizes.

Figure 4.3: Results of convolving the image on the top with the filters in Figure 4.2.

4.3. Log-Gabor Filters

Gabor filters face a limitation in their bandwidth coverage; they can cover one octave at most. Furthermore, it is impossible to construct Gabor filters that cover wide bandwidth and have small DC values at the same time. Thus, optimal results cannot be achieved if high bandwidth information is required. In his study on the statistics of natural images, Field [35] found that the use of Gaussian transfer functions in logarithmic frequency scale in constructing filters yields better results. Consequently, he proposed Log-Gabor filters as an alternative to Gabor filters. Log-Gabor filters can be constructed with arbitrary bandwidth and zero DC component. The Log-Gabor function is defined in the frequency domain as [35]:

$$G(f) = \exp\left\{\frac{-\left[\log\left(\frac{f}{f_0}\right)\right]^2}{2\left[\log\left(\frac{\sigma}{f}\right)\right]^2}\right\} \tag{4.6}$$

where f_0 is the center frequency of the filter, and σ is scaling factor of the bandwidth. The three-octave Log-Gabor function is approximately equal to the one-octave Gabor function [36]. Figure 4.4 shows a comparison between the responses of Gabor and Log-Gabor functions. It can be noticed that Gabor functions over-represent the low frequency components, leading to correlated and redundant information in the low frequency regions. On the other hand, the use of Log-Gabor functions results in equally spread information.
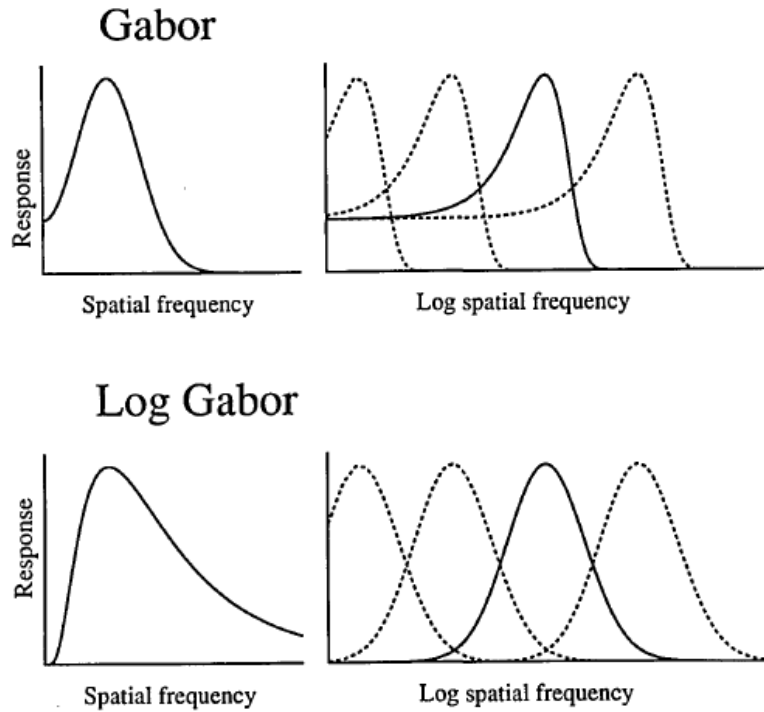
Figure 4.4: Comparison between Gabor and Log-Gabor functions responses. [**35**]

4.4. Quaternion Gabor Filters

There were very few attempts in the literature to extend the complex Gabor filter into the Quaternion domain. One of the early attempts was proposed by Bulow and Sommer [**37**]. Because complex Gabor filters are Gaussian modulated by a complex sinusoidal, they suggested implementing the Quaternion Gabor Filters by performing the Quaternion Fourier Transform. Thus, the 2D Gabor filter, given in Equation (4.2), can be extended to the Quaternion Gabor filter as:

$$g(x,y) = \frac{1}{2\pi\sigma_x\sigma_y} \exp\left\{-\frac{1}{2}\left[\frac{x^2}{\sigma_x^2} + \frac{y^2}{\sigma_y^2}\right]\right\} \exp\{i2\pi(ux+uy)\}. \exp\{j2\pi(ux+uy)\} \qquad (4.7)$$

Jones [33] explored several methods for extending the Gabor filter to Quaternion. He found that geometrical interpretation of the product gives the best interpretation of colors. This is based on the fact that multiplying two pure Quaternions will result in a real part equal to the negative of their dot product and a quaternion part as a vector equal to the cross product of these two vectors. Thus, the Gabor filter can be defined as a pure quaternion where its color component is as described in Section 3.5 and pointing to a particular direction in the 3D color space. A unit quaternion μ, pointing to an interesting direction in the 3D color space, is multiplied with the previously defined Gabor filter in order to get the Quaternion Gabor Filter. The resulting filter can be used to extract the intensity and hue information. By this method, the 2D Gabor filter, defined by Equation (4.2), is extended to the Quaternion Gabor filter by multiplying the unit quaternion μ with the real part of the filter as:

$$g(x,y) = \mu \frac{1}{2\pi\sigma_x\sigma_y} \exp\left\{-\frac{1}{2}\left[\frac{x^2}{\sigma_x^2} + \frac{y^2}{\sigma_y^2}\right]\right\} \cos\{2\pi(ux+uy)\} \qquad (4.8)$$

Figures 4.5 shows the real and imaginary parts of a Gabor filter. In comparison, Figure 4.6 shows the real and the three imaginary parts of a Quaternion Gabor filter.
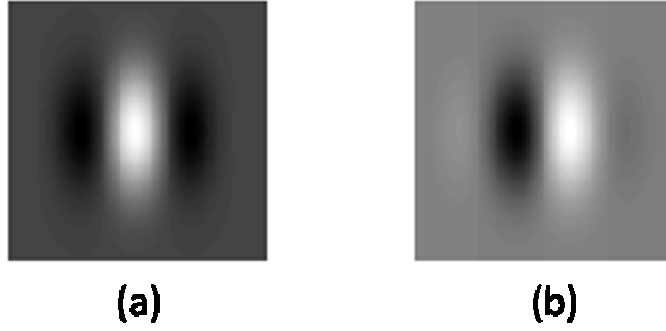
Figure 4.5: Complex 2D Gabor filter. (a) Real part. (b) Imaginary part. [**37**]
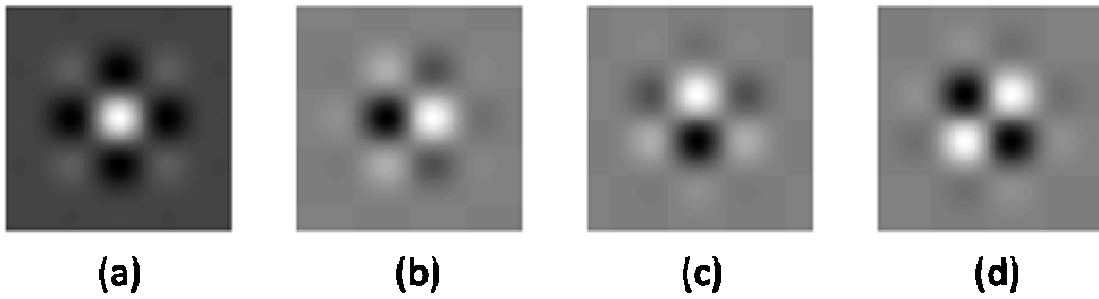

Figure 4.6: Quaternion 2D Gabor filter. (a) Real part. (b) Imaginary part (i-term). (c) Imaginary part (j-term). (d) Imaginary part(k-term). [**37**]

CHAPTER FIVE

METHODOLOGY AND EXPERIMENT DESIGN

5.1. Research Methodology

In this chapter, we will present several experiments to measure the performance of different methods proposed in this Thesis.

During the performance evaluation experiments, three representations are considered:

1. Grayscale representation of each color separately: The common complex Fourier Transform (FT) is used in the analysis.

2. Spatio-chromatic representation: The complex Fourier Transform will be used again. A description of the spatio-chromatic color representation is provided in Section 3.6.

3. Quaternion representation: Three types of Quaternion Fourier Transform are used, which are: the two-side, left-side and right-side transforms, respectively. Sections 3.3 and 3.5 give a detailed description.

In order to characterize the performance of these different representations, two types of performance evaluation are considered. The first type is to determine the performance when different noise statistics are introduced. Five types of noise are used in the

experiments. The second type is to determine the correlation measure between different images. This is carried out by using different performance measurements. An implementation of the Daugman algorithm is proposed for the sake of comparison. This requires a modification of the original algorithm in order to work with quaternion representations. A comparison will be performed by using color components separately.

5.2. Iris Image Database

UBIRISv1 database, provided by the University of Beira Interior in Portugal, was used in our experiments [38]. UBIRISv1 contains 1877 color images that were taken from 241 different persons in two distinct sessions. Images in the database have different kinds of noise in order to simulate the capturing with minimum collaboration from subjects. In session one, noise is reduced by taking pictures in a dark room. So, reflections, luminosity and contrast were reduced in this session. On the other hand, pictures in session two were taken in natural illumination which introduces the mentioned noises. The database is provided in three different formats:

a) 800 x 600 - 24 bit color

b) 200 x 150 - 24 bit color

c) 200 x 150 – Grayscale

Images are classified using three parameters: focus, reflection, and visible iris. Each of these parameters can have the following values: Good, Average, and Bad. Figure 5.1

illustrates some images in each category. The result of such classification is presented in Table 5.1.

Parameter	Good	Average	Bad
Focus	73.83%	17.53%	8.63%
Reflections	58.87%	36.78%	4.34%
Visible Iris	36.73%	47.83%	15.44%

Table 5.1: Classification of images in UBIRISv1 database.
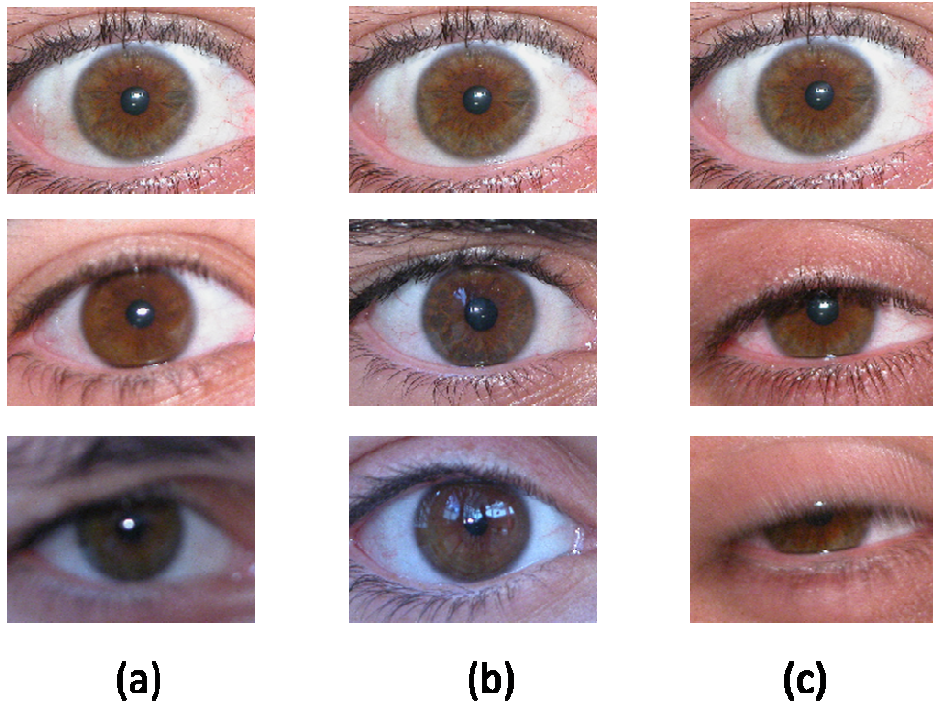

(a)   (b)   (c)

Figure 5.1: Classification of UBIRISv1 iris images. (a) Focus. (b) Reflection. (c) Visible iris.

5.3. Types of Errors

Two common types of errors in biometric systems can be used in the performance assessment of iris-based systems:

False Match: The error of considering two iris images from different persons to belong to one person. The False Match Rate (FMR) is the probability of false match error.

False Non-Match: False non-match error occurs when two iris images from the same person are considered to belong to different persons. False Non-Match Rate (FNMR) is the probability of false non-match error.

A trade-off between these two types of errors can be made, depending on the type of system being designed or deployed. For positive recognition systems, such as access control systems, false match represents accepting an imposter user, while false non-match would mean rejecting a genuine user. For negative recognition systems, such as banking systems, genuine attempts are rejected when having a false match, while imposter attempts are falsely accepted when having a false non-match [**39**].

5.4. Performance Evaluation of Hypercomplex Representation

5.4.1. Correlation Performance for Different Types of Noise

We conduct five experiments in order to see the performance of each representation against different types of noises. The following noises are tested: Gaussian noise, rotation, average filtering, median filtering, and compression using JPEG.

Gaussian noise: A noise of Gaussian distribution is added by using variances ranging from 0 to 1000 and a mean equal to zero. Figure 5.3 shows a comparison of using different color representations for POC performance evaluation. It is clear that the three types of QFT achieved much better results than regular FT and spatio-chromatic. On the other hand, spatio-chromatic representation had the worst results. In Figure 5.4, the same comparison was done by using BLPOC. For all representations, the results are much better than using POC only, and the three types of Quaternion still obtain the best results.

Rotation: Iris images are rotated through angles from 0 to 30° in increments of 1°. The correlation is considered as the performance measure. Figure 5.5 shows the performance results from POC-based techniques. As indicated, quaternion representations yielded the best performance. The inclusion of band-limited filtering (BLPOC) significantly improved the system performance as reported in Figure 5.6. The same performance superiority of the Quaternion representations is obtained. Moreover, the regular and spatio-chromatic representations slightly improved in performance.

Average Filtering[2]**:** Spatial average filtering is used with varying window sizes NxN with $3 \le N \le 11$. Figure 5.7 summarizes the performance of the systems being compared. Similar to the results given in Figures 5.5-5.6, the Quaternion representations achieved the best performance. This superiority in performance is due to the ability of these representations to efficiently capture the color information in the iris images (unlike, for instance, the case with their counterparts based on the spatio-chromatic transform). By ignoring the luminance component in the iris images, the latter representations clearly fail to meet the requirements of the "information-preserving rule" principle. Aiming to let the systems under investigation concentrate their retrieval capabilities on the most important features present in the iris images, band-limited filtering (BLPOC) is incorporated to investigate the efficiency of these systems when fed with band-limited iris information. Figure 5.8 gives a summary of the performance measures in this case. It can be safely stated, in the present case also, that the Quaternion representations successfully and efficiently captured the color information which enabled them to achieve the improved performance.

Median Filtering[3]**:** Figure 5.9 illustrates the performance of the systems in the presence of spatial median filtering. Varying window sizes NxN with $3 \le N \le 11$ are applied.

---

[2] Average filtering is considered to represent the loss of focus when capturing iris images.
[3] The effect of motion blurring is simulated by the incorporation of median filtering during the conducted experiments to assess the systems' performance.

Based on the analysis presented in average filtering, Quaternion-based transforms lead to the best performance due to the afore-mentioned properties. Furthermore, similar performance improvement is achieved when considering band-limited filtering of the iris images before conducting the experiments as evidenced by Figure 5.10.

JPEG Compression: Though there is no clear indication in the literature about the effect of image compression on the performance of existing iris-based recognition systems, it is quite interesting to investigate this effect for the sake of completeness. Figures 5.11-5.12 report the performance of the different systems under JPEG4 compression. Different image compression rates are considered. The compression rates are related to the quality factor ranging from 0 to 100. A quality factor of 100 means a perfect image coding where only a minor compression is achieved. On the other hand, a quality factor of 0 means full image compression. Figure 5.2 shows an iris image compressed using two quality factors (Figure 5.2 (b) Quality factor = 100 and Figure 5.2 (c) Quality factor = 0).

It is a well-known fact that JPEG compression is achieved by first removing the high frequency components of the images. This effect is similar to high pass filtering. However, to achieve high compression, JPEG compression attempts to remove parts of the low-frequency components. Therefore, JPEG compression can be viewed as a combined low-pass and high-pass filtering when a low quality factor is applied during compression. Therefore, the same performance behavior is expected in the presence of

---

[4] JPGEG: Joint Photographic Expert Group Standard for Image Coding.

JPEG compression. This would mean that the Quaternion-based transforms will result in the best achieved performance. The expected performance results are given in Figure 5.11. Finally, by using band-limited filtering of the iris images, all systems under investigation yield the same level of performance improvement as illustrated in Figure 5.12.
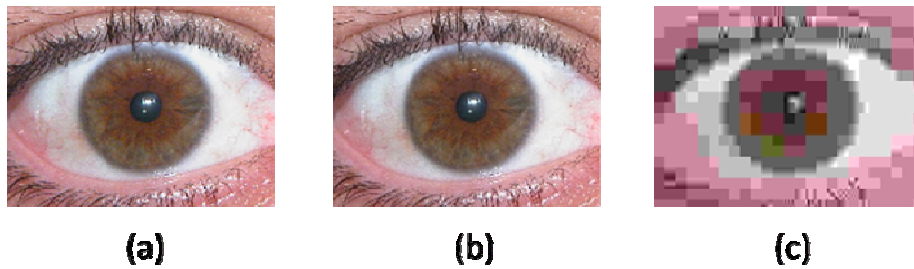

Figure 5.2: (a) Iris image. (b) Same image compressed using quality factor = 100. (c) Same image compressed using quality factor = 0.
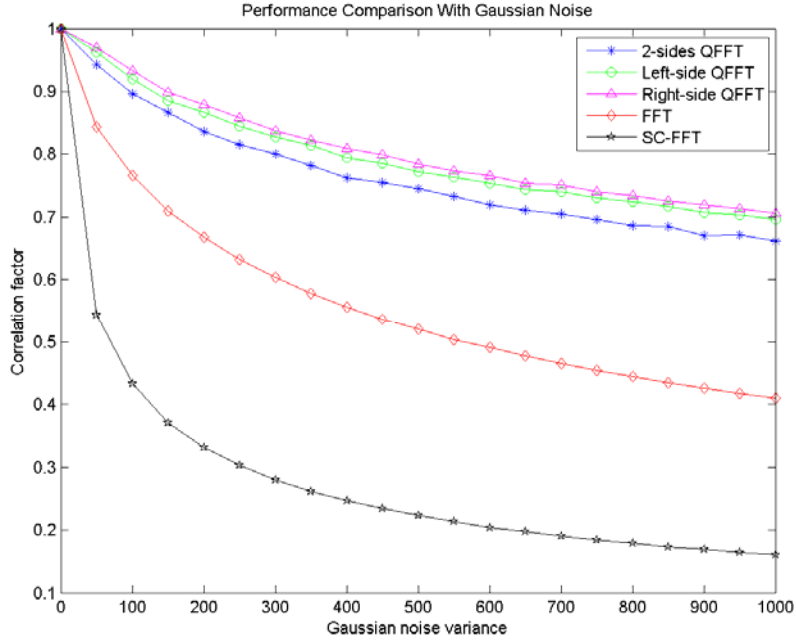
Figure 5.3: System performance against Gaussian noise.
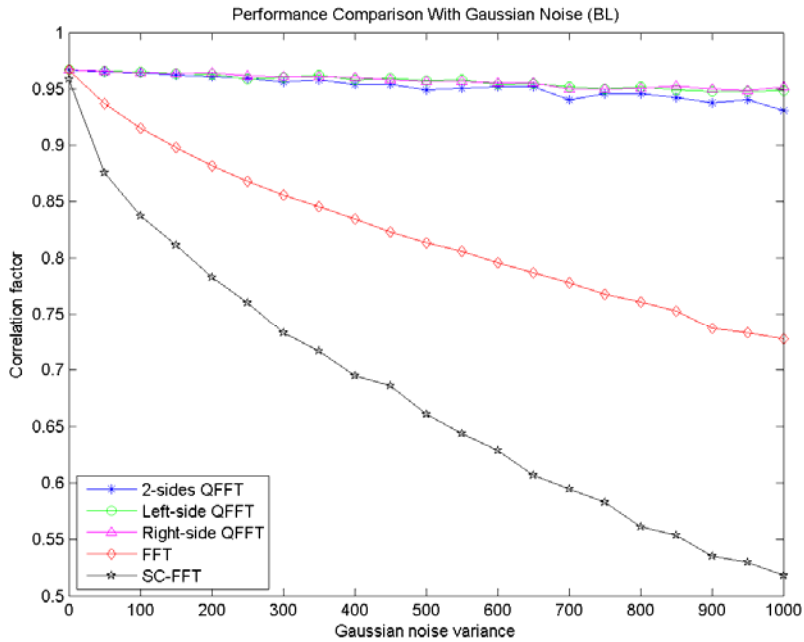
Figure 5.4: System performance against Gaussian noise using band-limited POC.
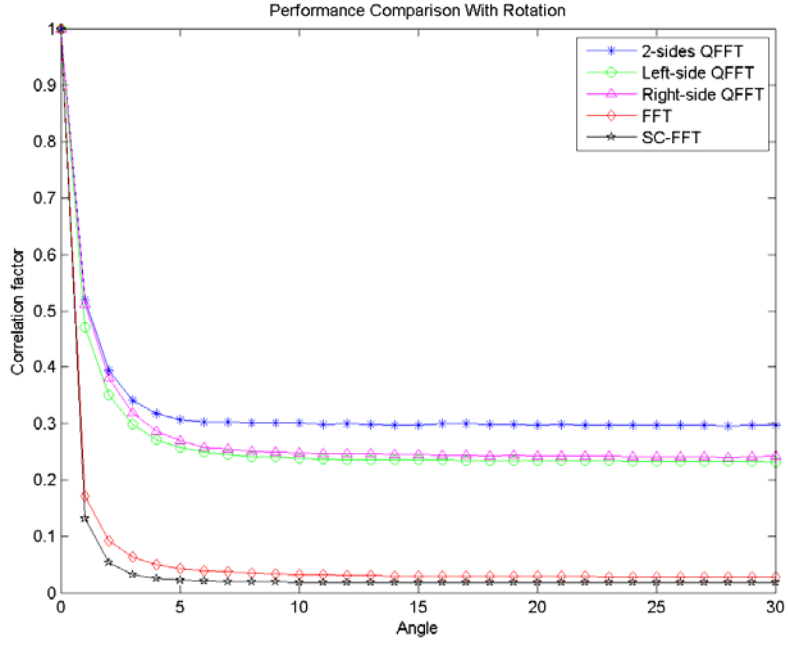
Figure 5.5: System performance against rotation.
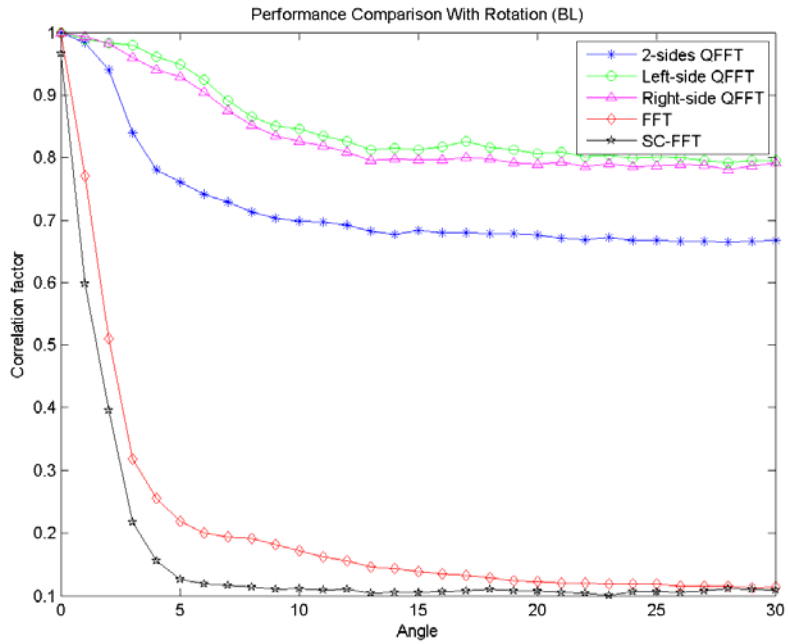
Figure 5.6: System performance against rotation using band-limited POC.
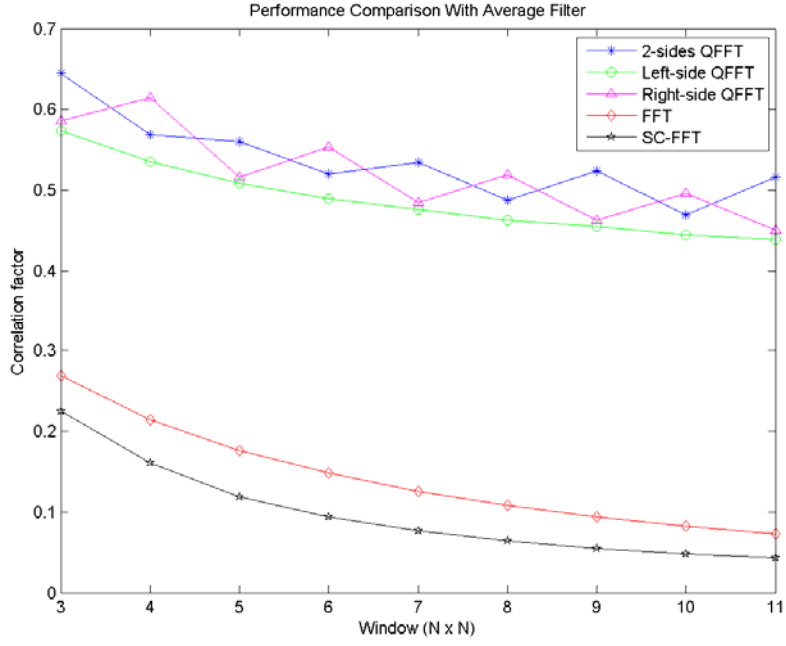
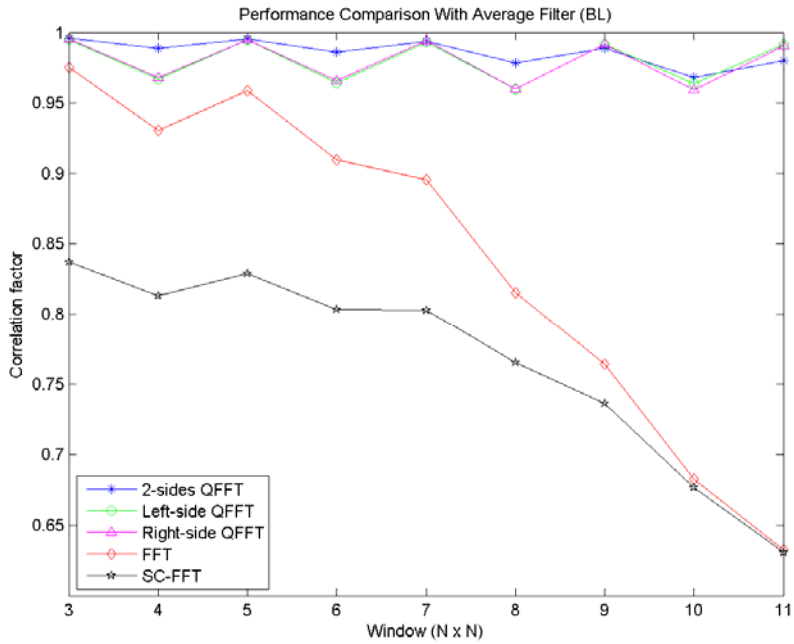Figure 5.7: System performance against average filtering.

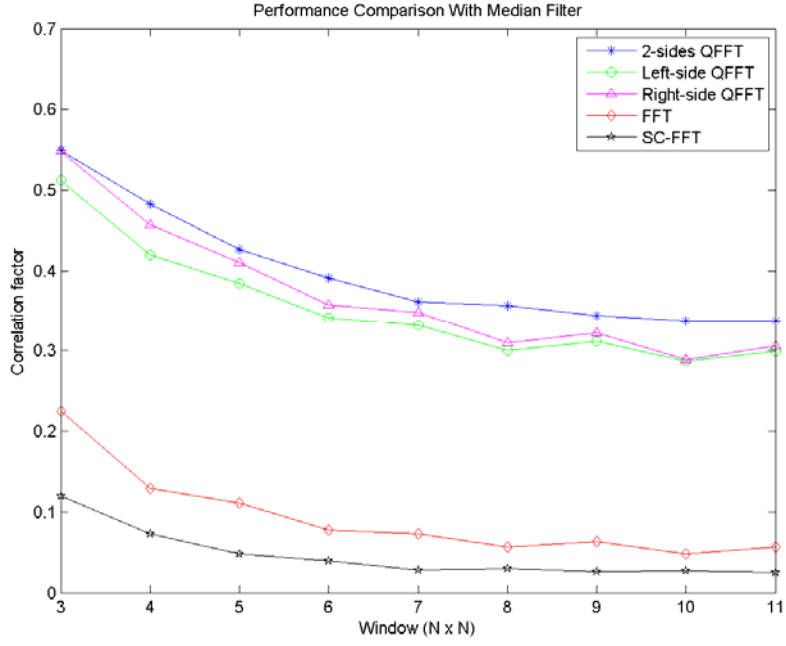Figure 5.8: System performance against average filtering using band-limited POC.

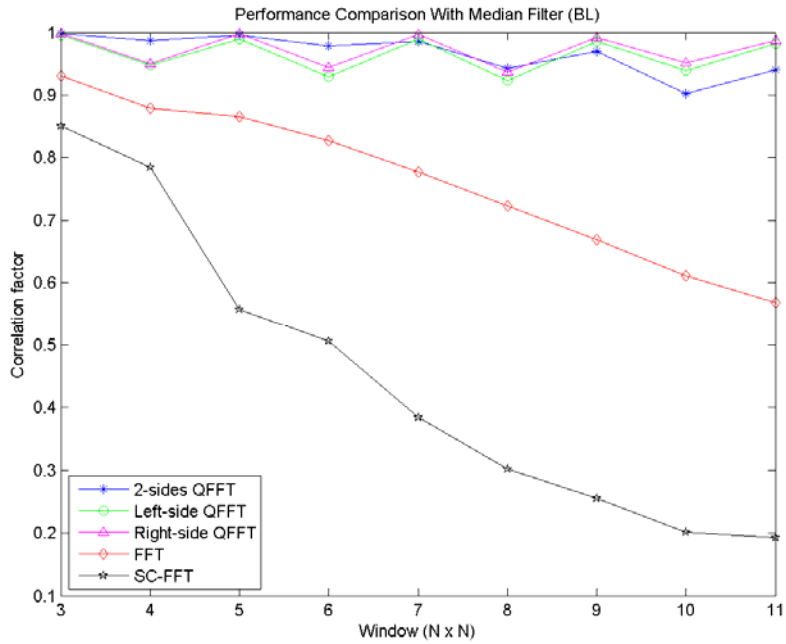Figure 5.9: System performance against median filtering.

Figure 5.10: System performance against median filtering using band-limited POC.
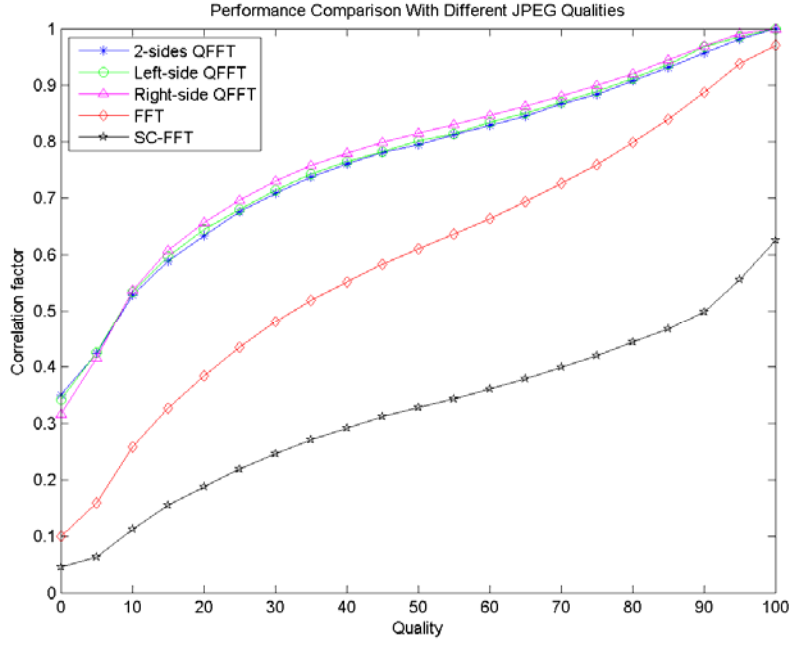
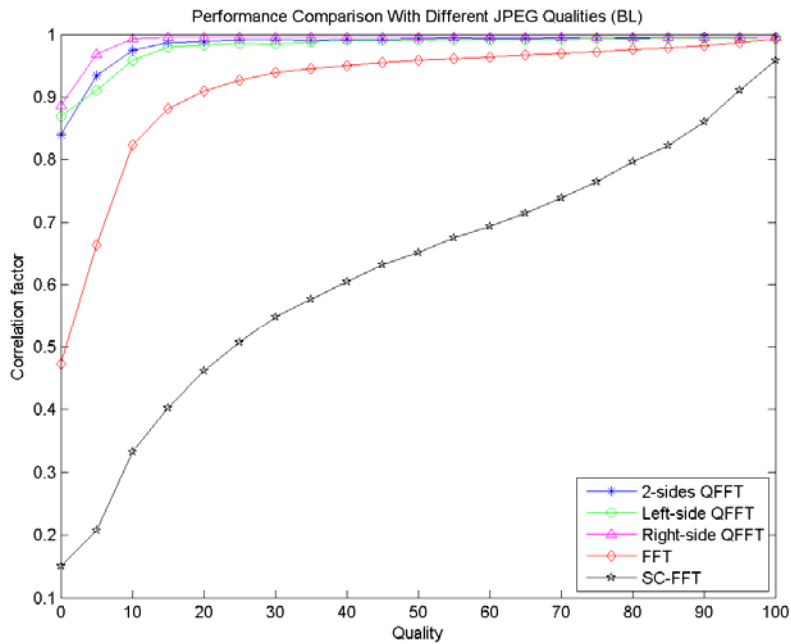Figure 5.11: System performance against JPEG compression.

Figure 5.12: System performance against JPEG compression using band-limited POC.

5.4.2. System Performance Statistics

5.4.2.1. Genuine versus Imposter Distribution

To estimate the genuine distribution, iris images belonging to the same person are compared against each other. It should be noted that if a comparison between sample i and sample j is performed, the inverse comparison is omitted since it will give the same result. The purpose of this procedure is to measure the similarity between iris images belonging to the same person. Moreover, to estimate the imposter distribution, comparisons between iris images belonging to different persons are performed. In this case, the ith sample of each person is compared to the ith sample of all the remaining persons. Since the correlation is an asymmetric process, if a comparison is carried out between samples i of two persons, the inverse comparison is omitted. The aim of imposter distribution is to measure the difference between iris images belonging to different persons.

Figure 5.13 illustrates a sample of genuine and imposter distributions. The more separated are the genuine and imposter distributions, the better is the matching process. The area of intersection between the two distributions represents errors in the system performance. FMR is the region of imposter distribution that is considered to belong to the genuine distribution. On the other hand, FNMR is the portion of genuine distribution that is considered as part of the Imposter distribution. The selection of a specific threshold provides a trade-off between the FNMR and FMR probabilities, which depends

on the application of the biometric system. For instance, in forensic applications for criminal identification, FMR is selected to be large in order not to miss the criminal. In highly secure access control systems, FNMR is chosen to be large to ensure that only genuine users will gain access.
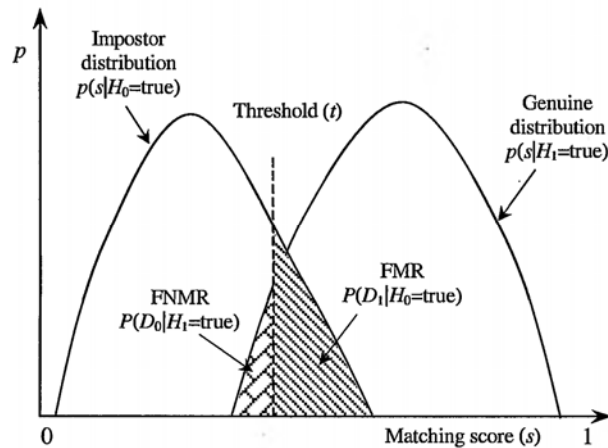

Figure 5.13: Genuine versus imposter distributions, and illustration of FNMR and FMR errors suing a threshold t. [**39**]

Better results are achieved if the two distributions are well separated. Thus, the separation between the mean of the two distributions gives a hint about the system's performance. This separation is called the "*decidability index*". The decidability index, d́, is calculated as follows [4]:

$$\acute{d} = \left| \mu_g - \mu_i \right| \qquad\qquad (5.1)$$

where μ_g and μ_i are the means of the genuine and imposter distributions, respectively.

Table 5.2 shows the decidability index for the different representations. Large values for the decidability index do not necessarily mean that the performance is better. In some cases, the errors too can be large and should be taken into account. To illustrate this concept, errors regions are highlighted in Figures 5.14 and 5.15.

Fourier Transform Method	Decidability Index
FFT	0.0926
FFT-BL	0.0559
QFT two-side	0.1239
QFT two-side BL	0.3302
QFT left-side	0.1921
QFT left-side BL	0.2128
QFT right-side	0.2826
QFT right-side BL	**0.2267**
Spatio-chromatic FT	0.0535
Spatio-chromatic FT BL	0.3578

Table 5.2: Decidability indices for the different representations.

Figure 5.14 shows the genuine and imposter distributions using the POC algorithm and the regular FFT. Vertical lines illustrate the means of the two distributions, and the shaded region indicates the errors resulting from their intersection. Band-Limited filtering (BLPOC) yields distributions illustrated in Figure 5.15. It can be noted that BLPOC achieved better separation between genuine and imposter distributions, but with far more

errors. The error region is shown as the shaded portion. In Figure 5.16, the distributions of using two-side QFT representation for the POC-based technique are shown. The separation of genuine and imposter is better than that achieved by using the regular FFT. As shown in Figure 5.17, the use of Band-Limited filtering (BLPOC) yields more separation, but also far more errors. This finding is in agreement with the result of regular FFT. The distributions using left-side QFT representation and POC technique are shown in Figure 5.18. The separation is slightly better than what is achieved by two-side QFT. In the case of BLPOC, the distributions are presented in Figure 5.19. As in the two-side QFT, the separation between the two distributions is greater, but also the errors increase rapidly. In Figure 5.20, the distributions using right-side QFT representation are illustrated. It can be noticed that the separation between genuine and imposter distributions is far greater than that of left-side QFT. The result of inclusion of Band-Limited filtering is shown in Figure 5.21. This result agrees with the previous representations in that more separation is achieved, but with more errors. The distributions of spatio-chromatic FT using POC-based algorithm are shown in Figure 5.22. It can be inferred from this figure that spatio-chromatic FT achieved less separation than the three types of QFT, but more than FFT. The use of BLPOC resulted in more widely separated distributions, but with more errors, which are presented in Figure 5.23. It is clear that the use of Band-Limited filtering (BLPOC) contributed to the improvement in the system performance. However, this observation is violated in the right-side QFT.
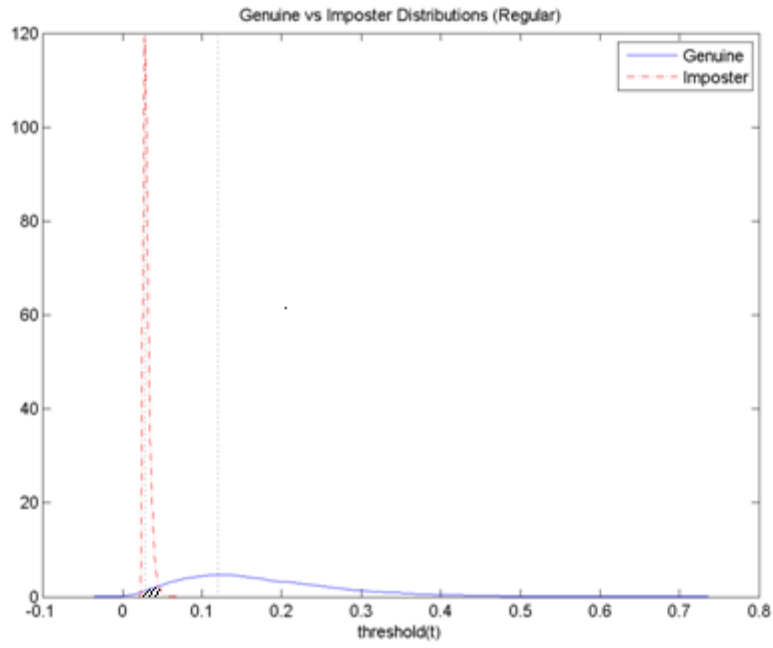
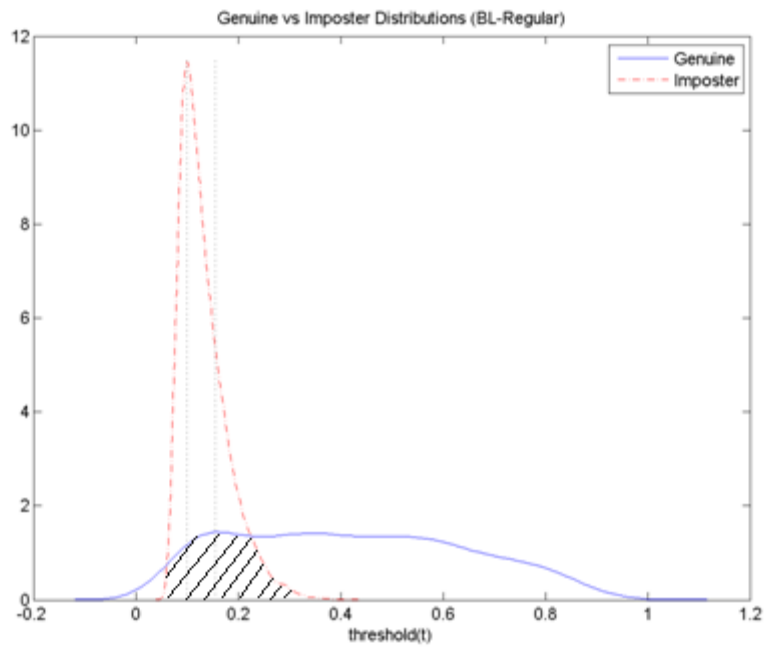Figure 5.14: Genuine versus imposter distributions using regular FFT and POC.

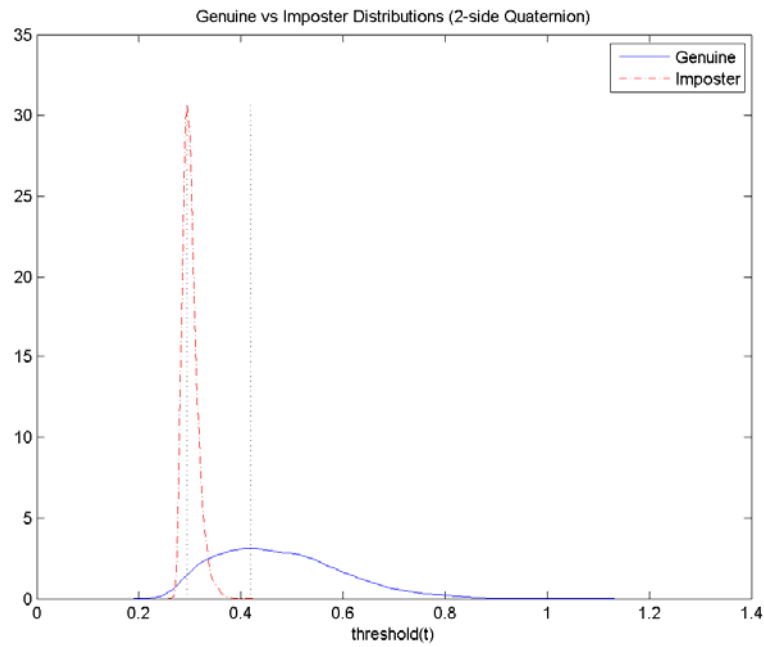Figure 5.15: Genuine versus imposter distributions using regular FFT and band-limited POC.

74

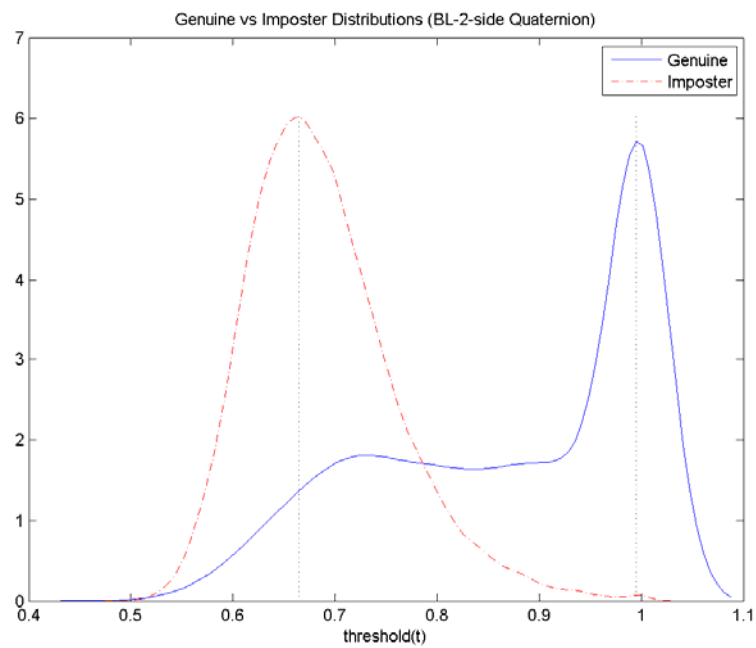Figure 5.16: Genuine versus imposter distributions using two-side QFT and POC.

Figure 5.17: Genuine versus imposter distributions using two-side QFT and band-limited POC.
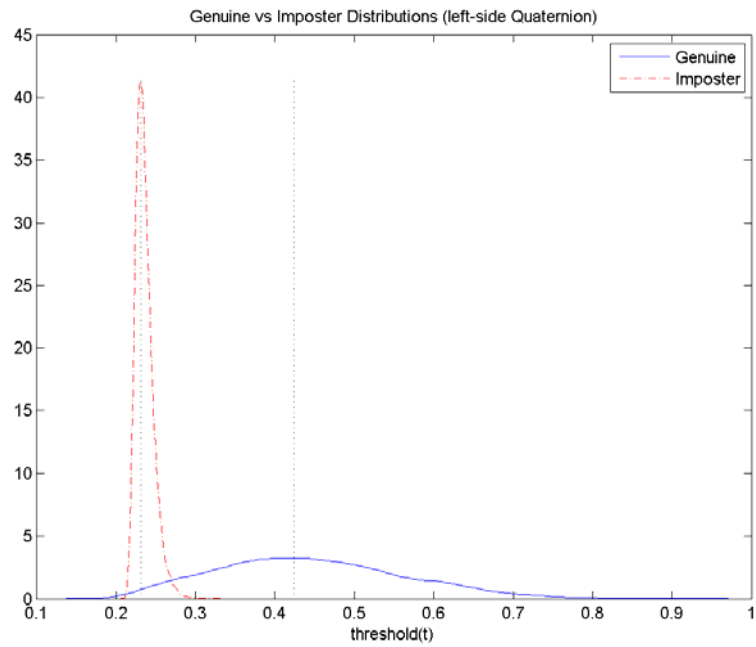
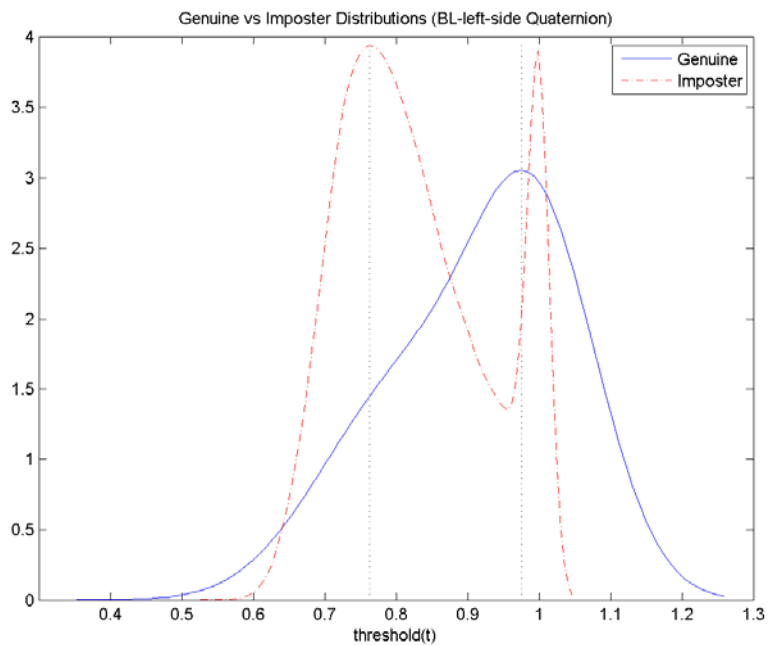Figure 5.18: Genuine versus imposter distributions using left-side QFT and POC.

Figure 5.19: Genuine versus imposter distributions using left-side QFT and band-limited POC.
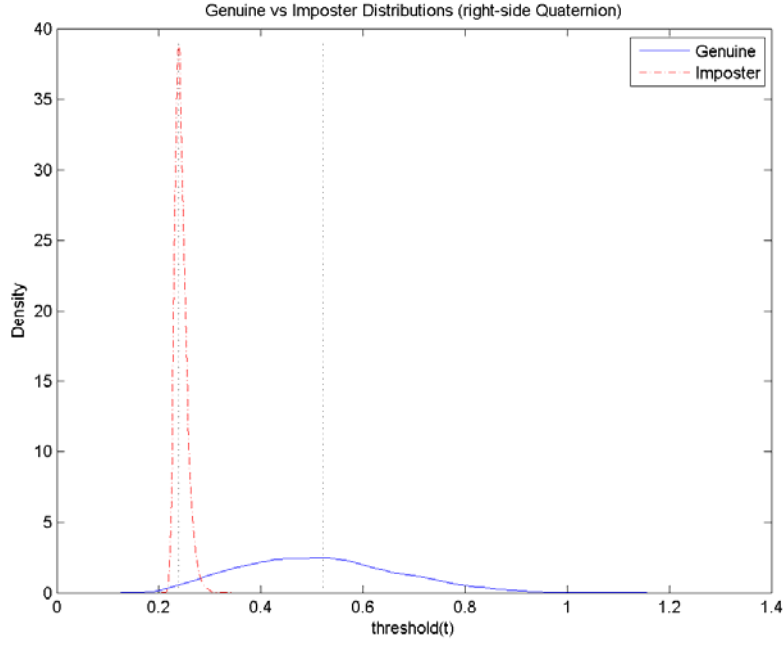
Figure 5.20: Genuine versus imposter distributions using right-side QFT and POC.
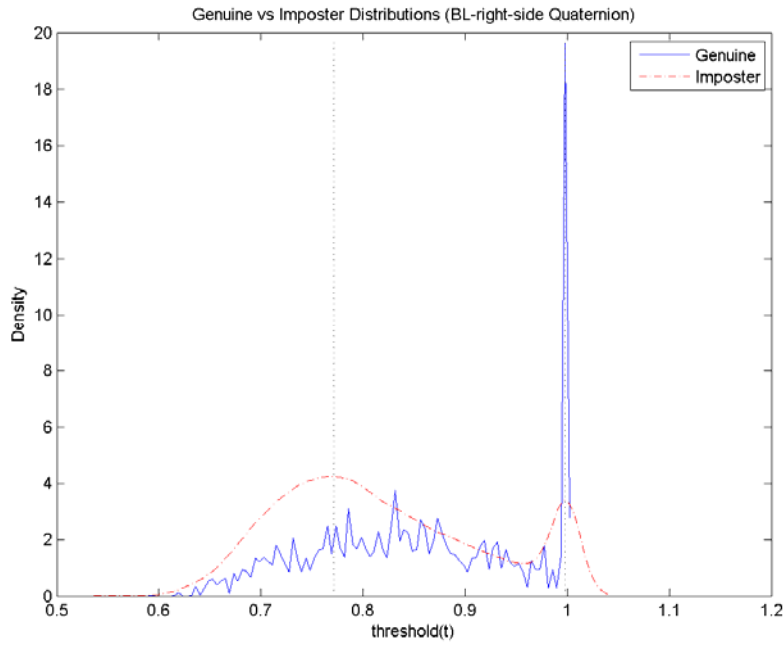

Figure 5.21: Genuine versus imposter distributions using right-side QFT and band-limited POC.
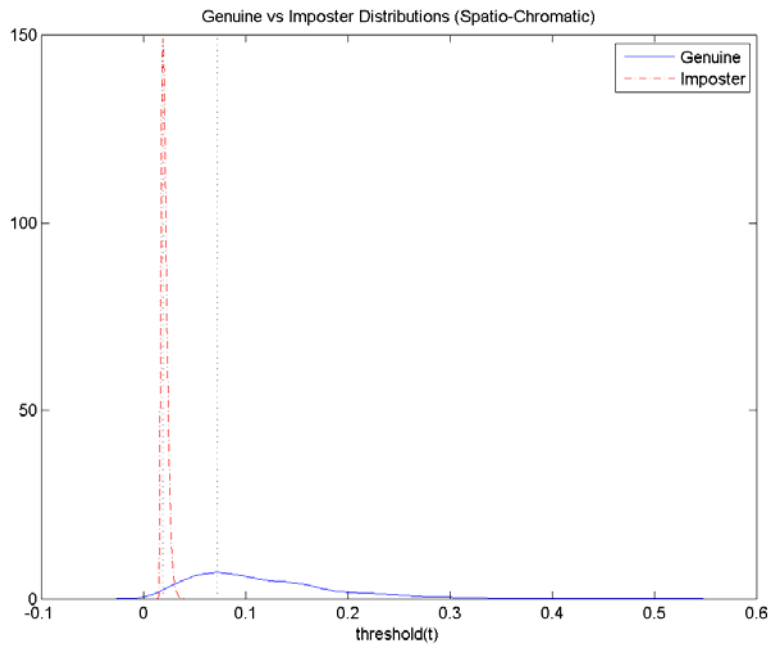
Figure 5.22: Genuine versus imposter distributions using spatio-chromatic FT and POC.
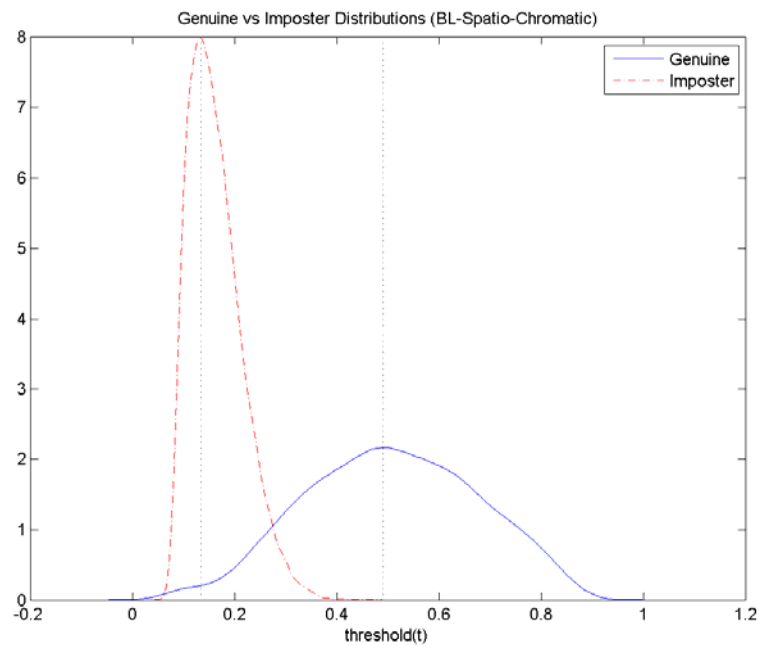

Figure 5.23: Genuine versus imposter distributions using spatio-chromatic FT and band-limited POC.

5.4.2.2. FMR and FNMR

The FMR and FNMR curves can be calculated from the genuine and imposter distributions by using a threshold t that ranges from 0 to 1. Thus, the FMR(t) and FNMR(t) are functions of t, where FMR(t) is the percentage of imposters greater than or equal to the threshold, and FNMR(t) is the percentage of genuine less than the threshold [39].

The following information can be inferred from the FMR and FNMR curves as illustrated in Figure 5.24 [39]:

Equal-Error Rate (EER): It is the error rate where FMR(t) = FNMR(t). Lower EER values indicate less errors. EER for the different representations is provided in Table 3.3.

ZeroFNMR: It is the lowest FMR where no FNM occur.

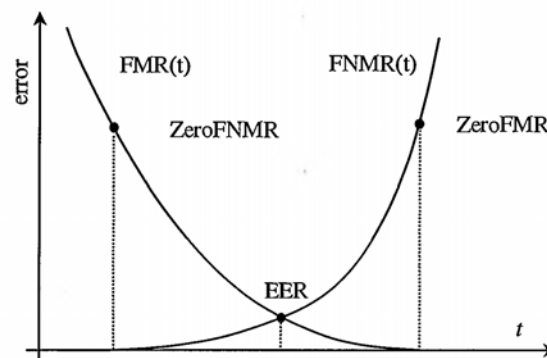**ZeroFMR**: It is the lowest FNMR where no FM occurs.

Figure 5.24: FMR and FNMR curves. [39]

79

Fourier Transform Method	EER
FFT	0.04
FFT-BL	0.18
QFT 2-sides	0.32
QFT 2-sides BL	0.73
QFT left-side	0.26
QFT left-side BL	0.86
QFT right-side	0.27
QFT right-side BL	0.83
Spatio-chromatic FT	0.03
Spatio-chromatic FT BL	0.25

Table 5.3: EER for the different representations.

Figure 5.25 shows the FMR and FNMR curves when using the regular FFT and POC. It can be noted that EER is small, and consequently errors are low. Figure 5.26 illustrates the curves when introducing Band-Limited filtering (BLPOC). The EER value is greater than the one achieved with POC, and thus BLPOC generate more errors. This observation confirms the results obtained from the genuine and imposter distributions. Figure 5.27 shows the curves using two-side QFT representation and POC. The EER value is greater than that obtained by using regular FFT. This indicates that two-side QFT representation has more errors. Figure 5.28 shows the curves when using BLPOC. It is clear that EER is far greater than the one obtained by using POC. Consequently there are far more errors. The curves using the left-side QFT and POC-based technique are shown in Figure 5.29. The value of EER is less than that obtained by using two-sides QFT. On the other hand,

the curves of left-side QFT using Band-Limited filtering (BLPOC) achieved greater EER compared with BLPOC of two-sides QFT. These curves are presented in Figure 5.30. In Figure 5.31, the curves using right-side QFT representation and POC are shown. A very similar EER value to left-side QFT can be observed. Similarly, Figure 5.32 shows the curves of right-side QFT using BLPOC and is very similar to that of left-side QFT. The curves of spatio-chromatic FT representation and POC are shown in Figure 5.33. The lowest EER value is obtained, which indicates that the lowest error rate is achieved by spatio-chromatic FT representation. The curves of spatio-chromatic FT using BLPOC give far greater EER value. These curves are presented in Figure 5.34.
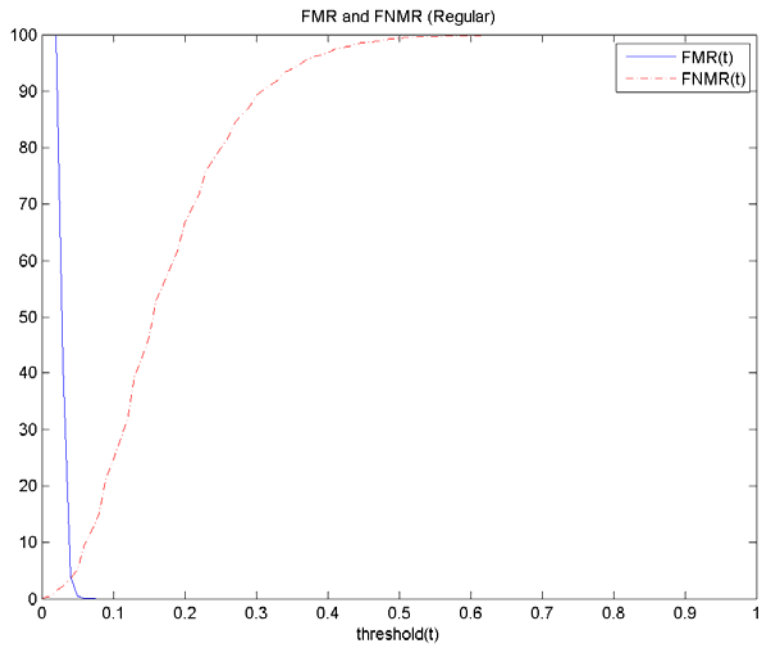
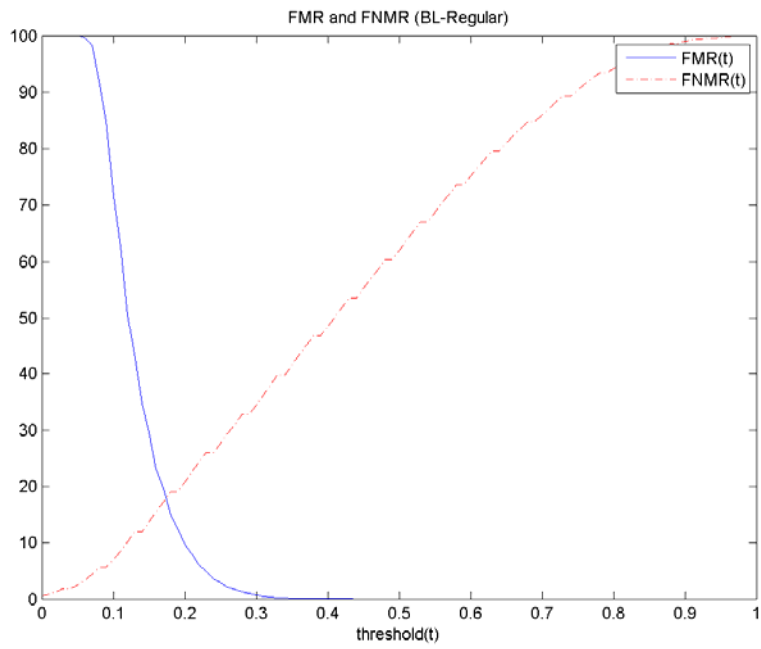Figure 5.25: FMR and FNMR using regular FFT and POC.

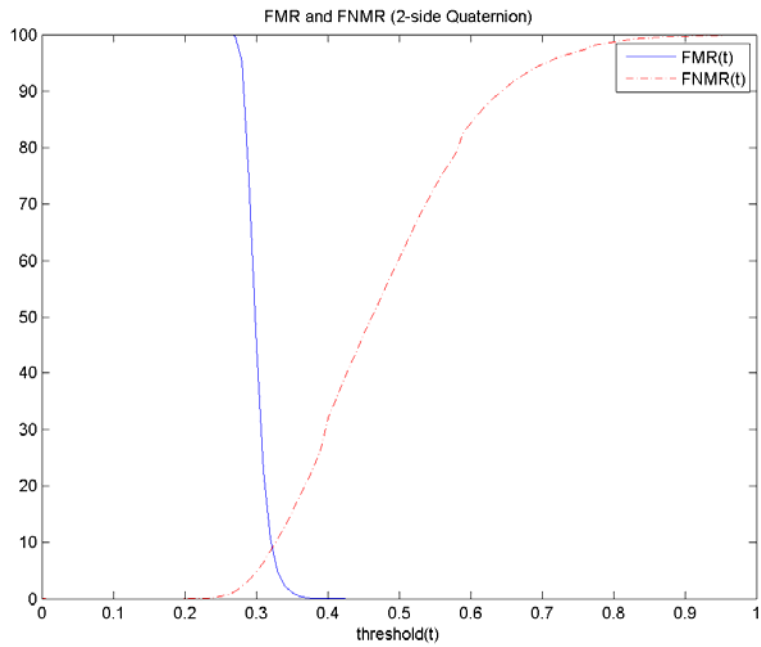Figure 5.26: FMR and FNMR using regular FFT and band-limited POC.

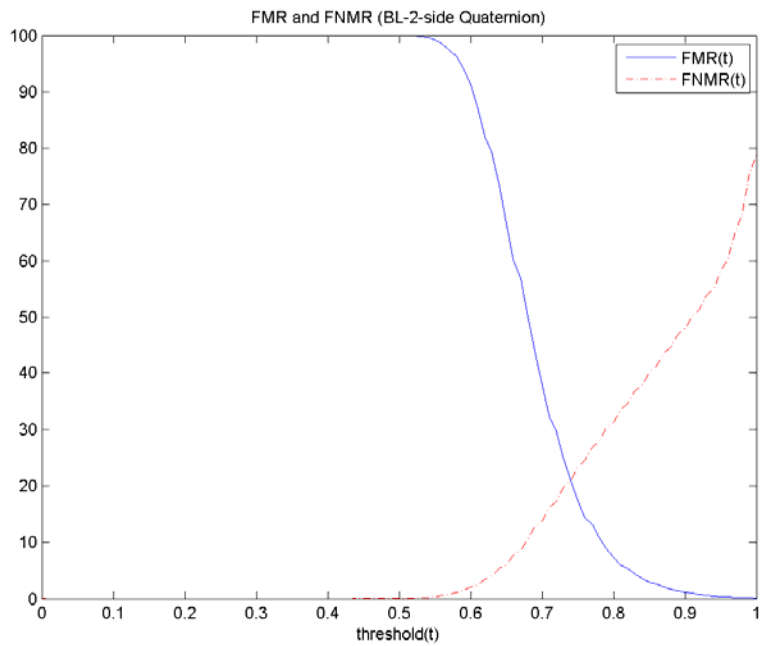Figure 5.27: FMR and FNMR using 2-sides QFT and POC.

Figure 5.28: FMR and FNMR using 2-sides QFT and band-limited POC.
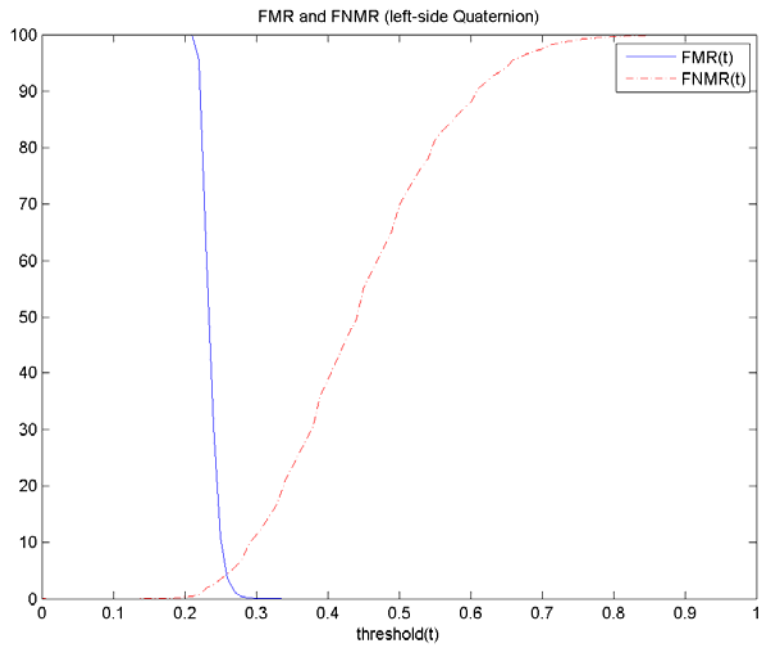
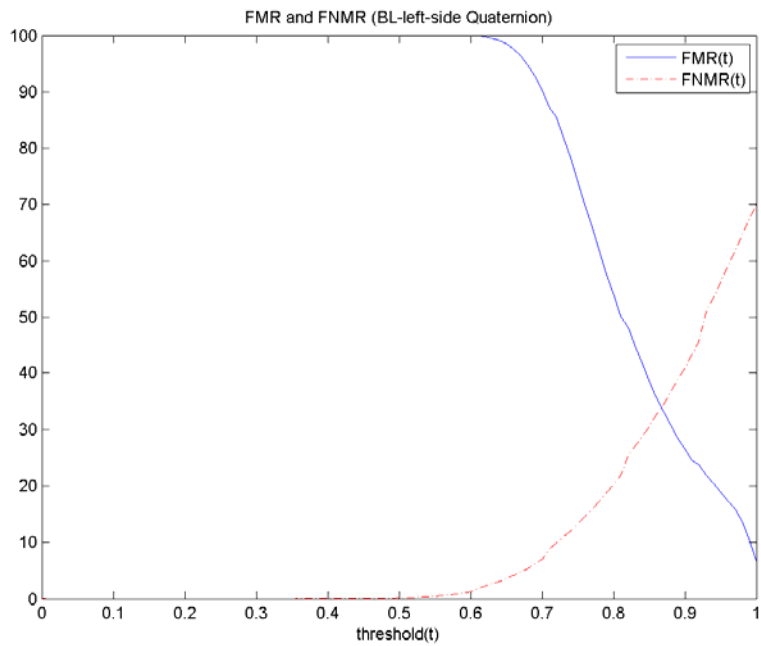Figure 5.29: FMR and FNMR using left side QFT and POC.

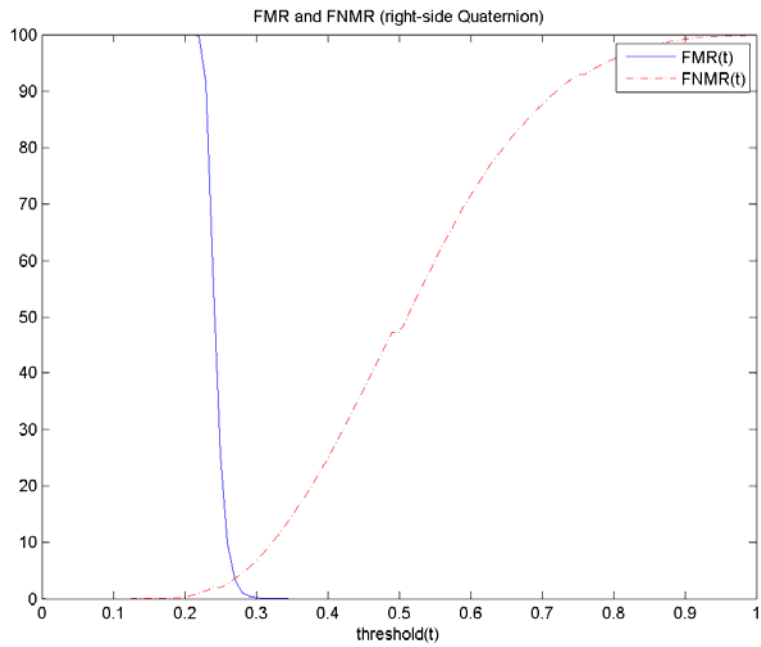Figure 5.30: FMR and FNMR using left side QFT and band-limited POC.

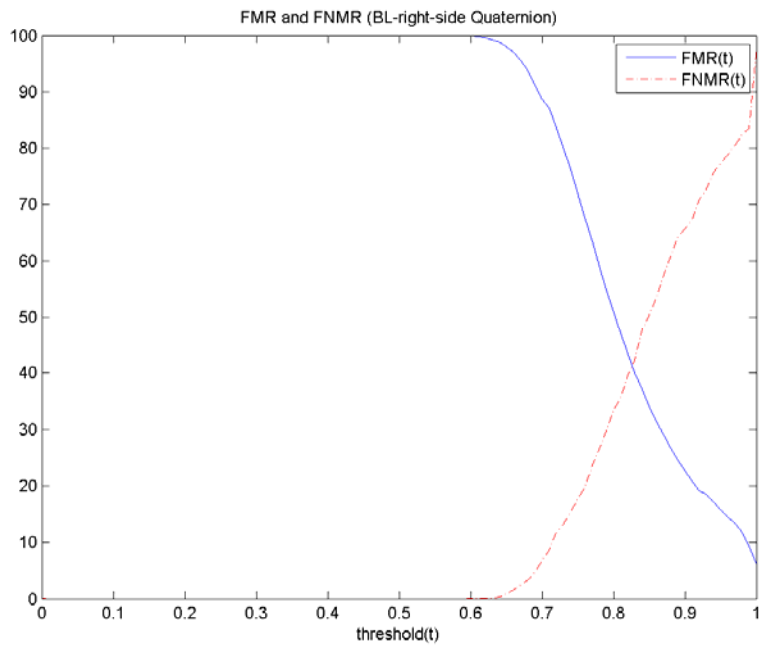Figure 5.31: FMR and FNMR using right side QFT and POC.

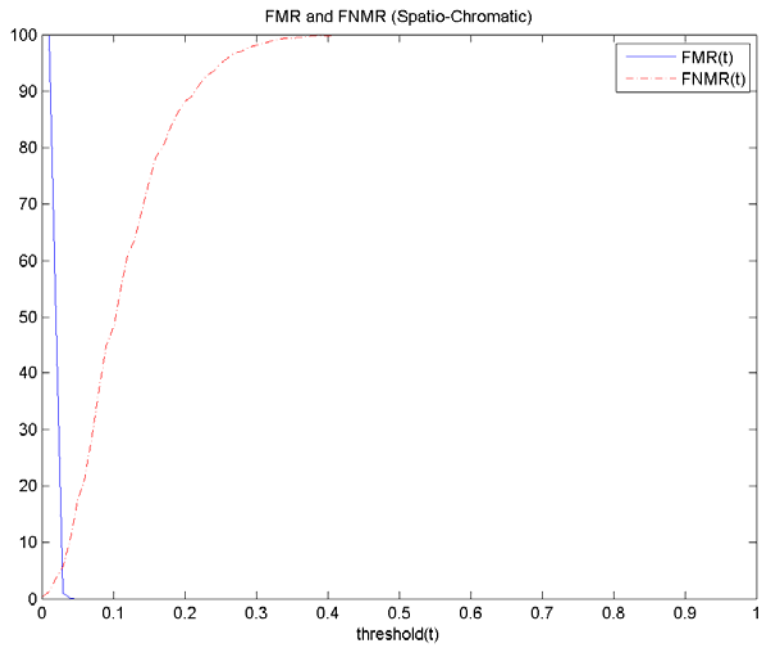Figure 5.32: FMR and FNMR using right side QFT and band-limited POC.

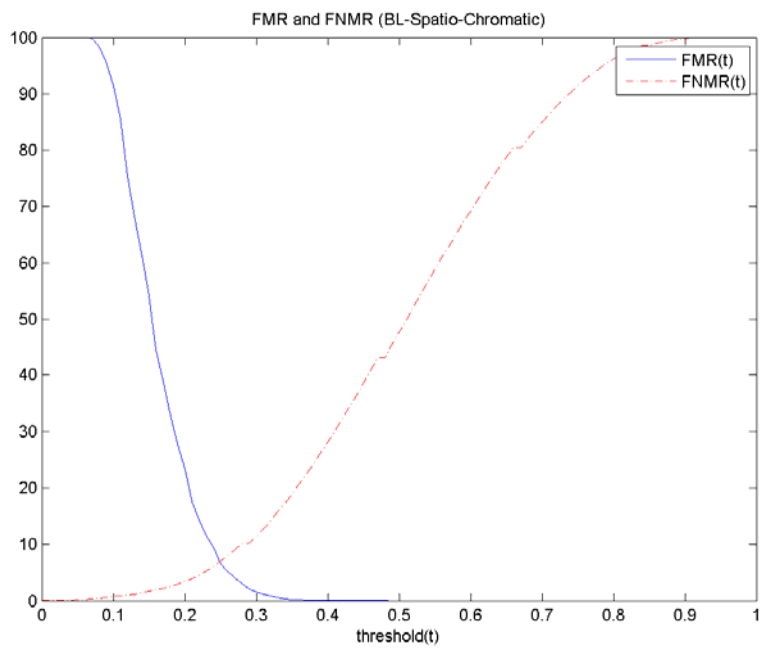Figure 5.33: FMR and FNMR using Spatio-Chromatic FT and POC.

Figure 5.34: FMR and FNMR using Spatio-Chromatic FT and band-limited POC.

5.4.2.3. Receiver Operating Characteristic (ROC) Curve

ROC curves show the system performance at all thresholds, and so the whole picture of the system performance can be seen. ROC curves can be achieved by plotting the FNMR as a function of FMR [**39**]. In the implementation, the plot is scaled by using log-log scales in order to make it clearer. From ROC curves, the relationship between FMR and FNMR can be observed. As FMR is increased, FNMR is decreased, and vice versa. The best curve is a straight horizontal line with zero FNMR, which means that EER is equal to zero.

Figure 5.35 shows the ROC curve when using the regular FFT and POC-based technique. The relationship between FMR and FNMR can be observed clearly. As FMR is increased, FNMR is decreased, and vice versa. Figure 5.36 illustrates the curve when using Band-Limited filtering (BLPOC). Compared with the POC curve, the result of BLPOC is a higher curve, which indicates higher EER values and errors. In Figure 5.37, the curve using two-side QFT representation and POC is illustrated. It can be observed that the curve is higher than the one obtained using regular FFT, and thus two-side QFT yields more errors. This confirms the finding from genuine and imposter distributions and FMR and FNMR curves. Figure 5.38 shows the result when introducing Band-Limited filtering (BLPOC). It is clear that by using BLPOC, more errors are achieved. The curve using left-side QFT and POC is shown in Figure 5.39. It can be inferred from this curve that left-side QFT achieved results with fewer errors compared with two-side QFT. Introducing Band-Limited filtering (BLPOC) increases the number of errors as illustrated in the curve of Figure 5.40. In Figure 5.41, the curve for using right-side QFT

representation and POC-based technique is presented. It can be noticed that the curve is slightly lower than the curve achieved in left-side QFT, and thus fewer errors are produced by right-side QFT. As all previous results, Band-Limited filtering (BLPOC) increases the number of errors, and this is obvious in the curve in Figure 5.42. The curve of spatio-chromatic FT representation and POC is shown in Figure 5.43. Among all curves, its curve is the lowest. Consequently, spatio-chromatic representation yields the lowest error rate among all representations. This confirms the result found by using the FMR and FNMR curves. The introduction of Band-Limited filtering (BLPOC) produced a higher curve, which indicates more errors. This curve is presented in Figure 5.44.
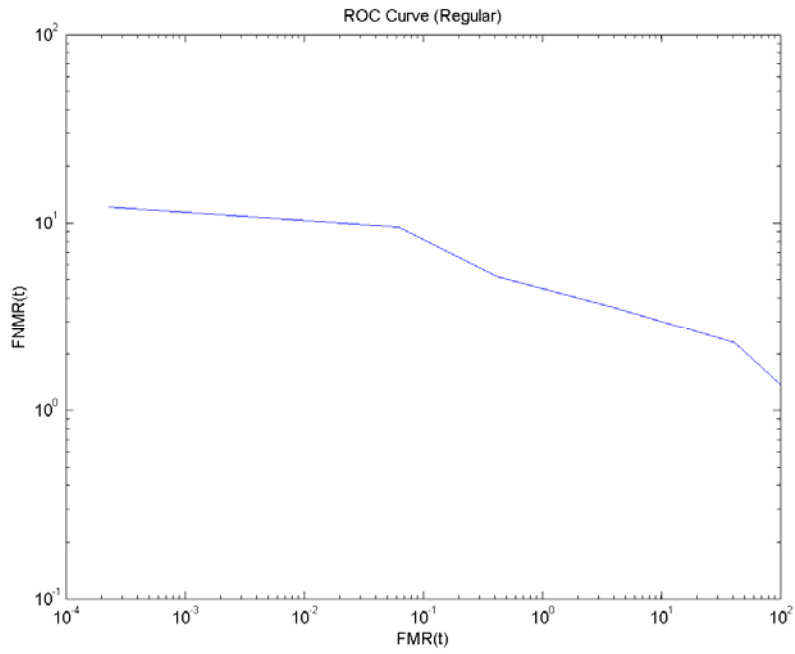
Figure 5.35: ROC curve using regular FFT and POC.

Figure 5.36: ROC curve using regular FFT and band-limited POC.

Figure 5.37: ROC curve using 2-sides QFT and POC.

Figure 5.38: ROC curve using 2-sides QFT and band-limited POC.

Figure 5.39: ROC curve using left side QFT and POC.

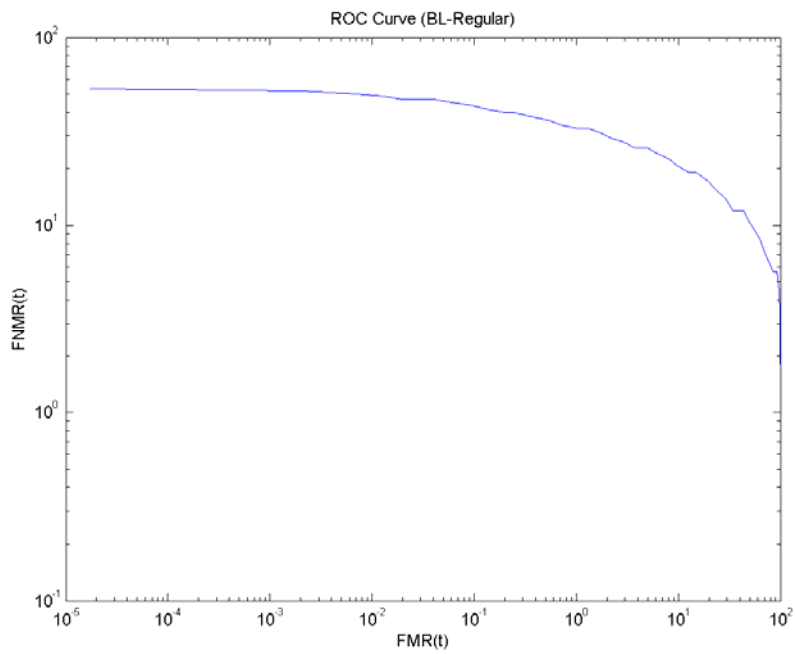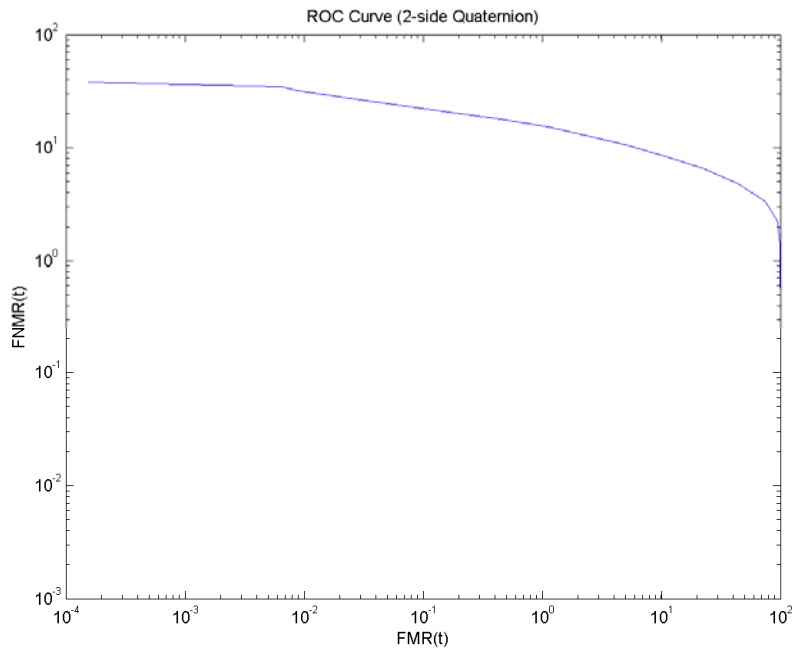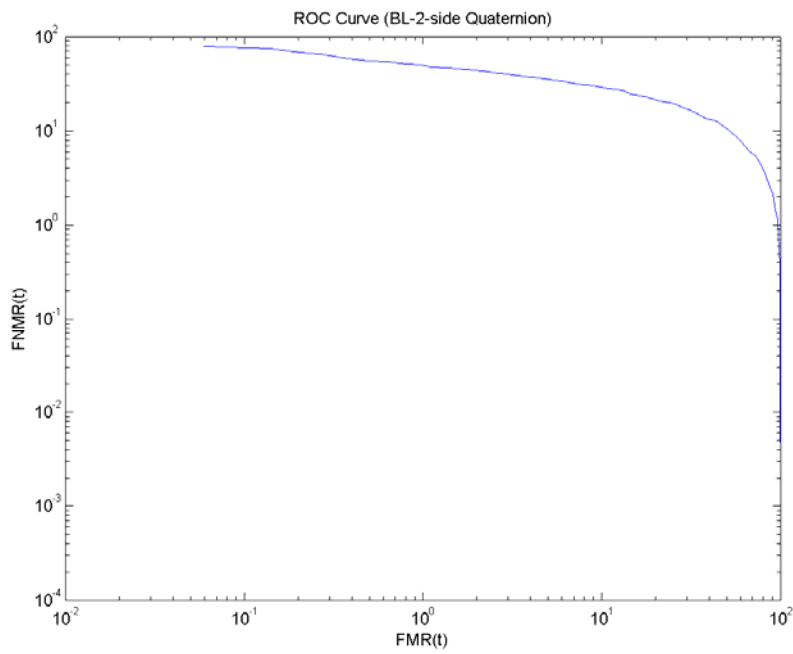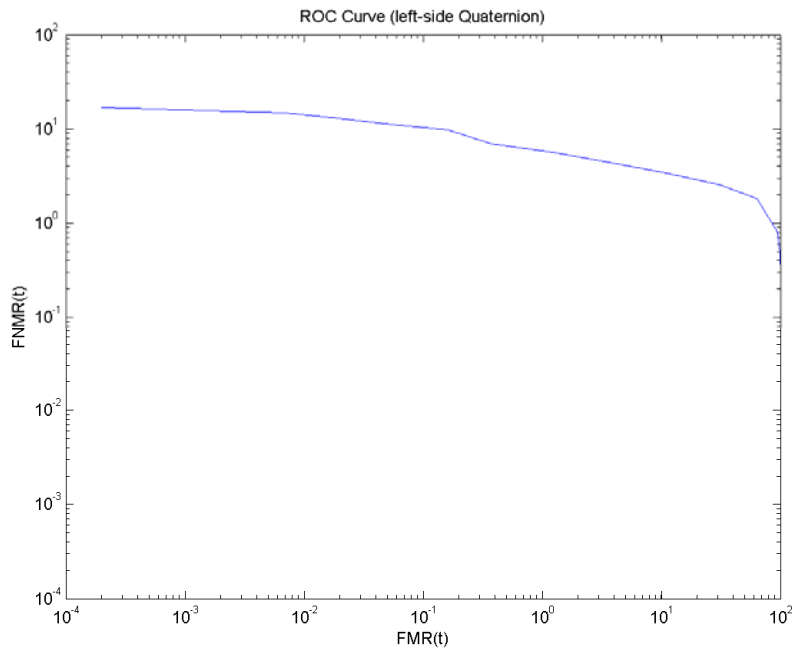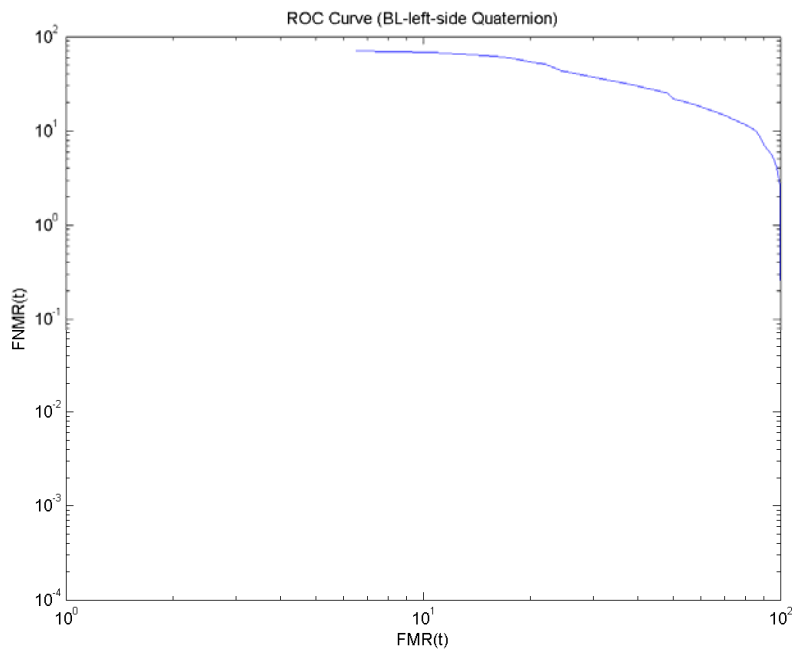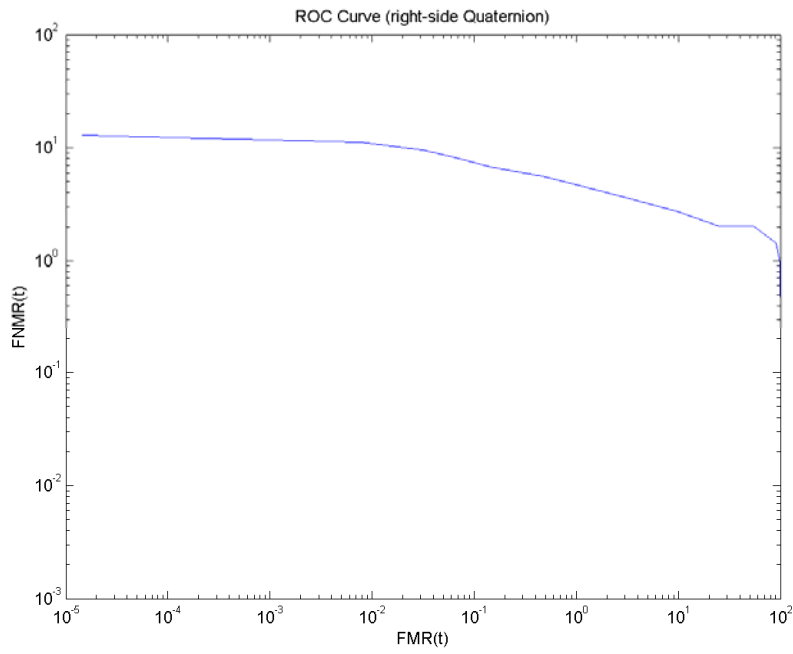Figure 5.40: ROC curve using left side QFT and band-limited POC.

Figure 5.41: ROC curve using right side QFT and POC.
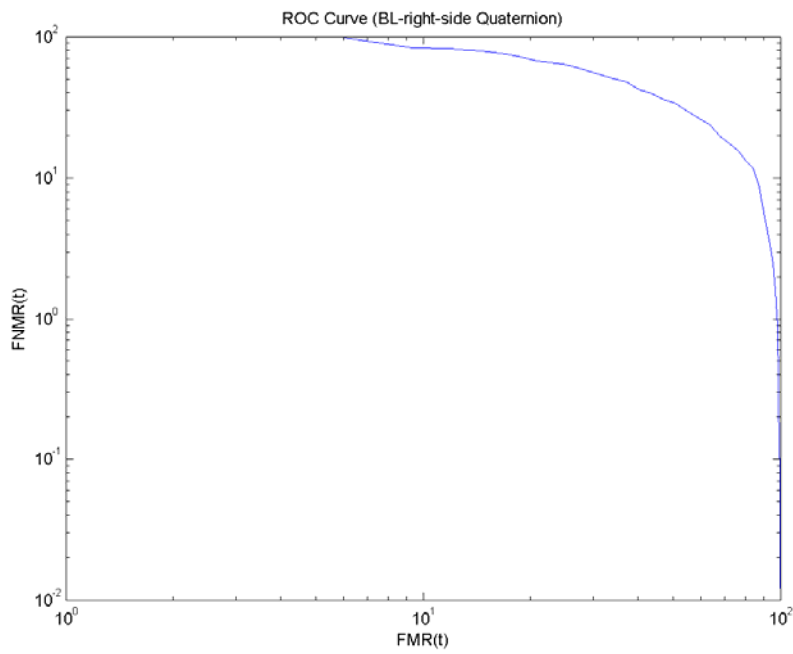
Figure 5.42: ROC curve using right side QFT and band-limited POC.
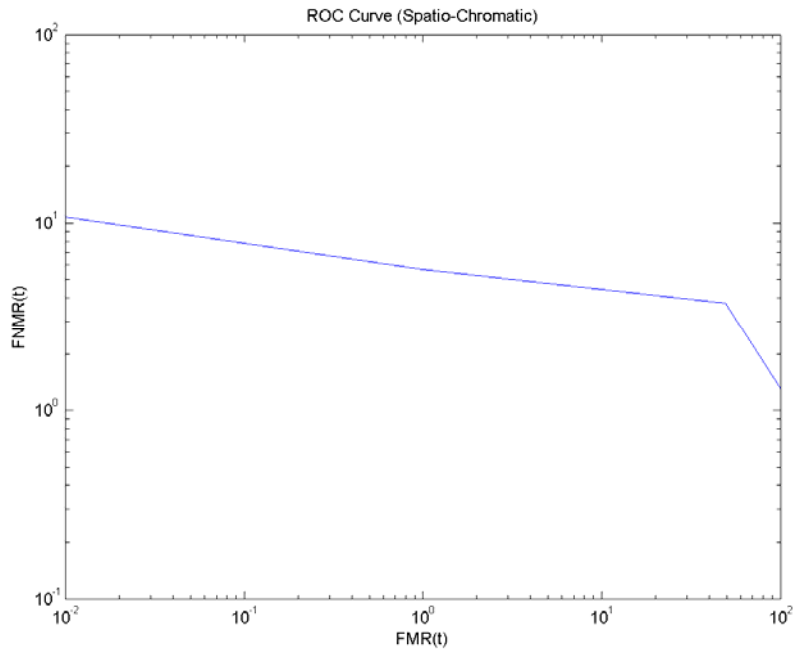
Figure 5.43: ROC curve using Spatio-Chromatic FT and POC.
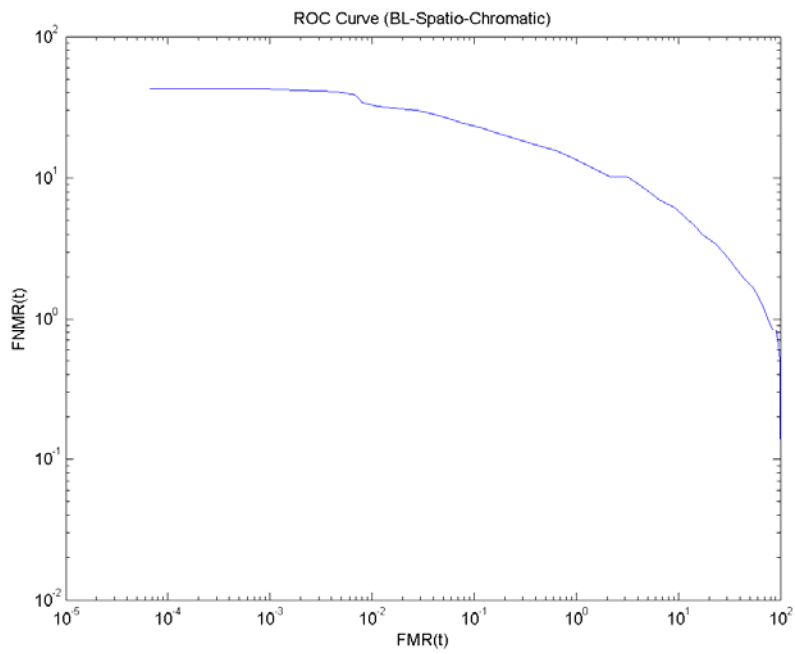
Figure 5.44: ROC curve using Spatio-Chromatic FT and band-limited POC.

5.4.2.4. Precision versus Recall Measure

Precision and recall are well known accuracy measurements for information retrieval systems. By using precision versus recall, the accuracy of getting n% of the models can be measured [**40**]. They can be calculated as follows [**40**]:

$$\text{Recall} = \frac{\text{retrieved in class}}{\text{total in class}} \tag{5.2}$$

$$\text{Precision} = \frac{\text{retrieved in class}}{\text{total retrieved}} \tag{5.3}$$

where 'retrieved in class' is the number of items retrieved in certain class, 'total in class' is total number of items in that class, and 'total retrieved' is the number of items retrieved.

In order to evaluate the whole system, several precision and recall curves are generated from different queries, and their average is taken. Because there are 11 recall points between 0 and 1, an interpolation is performed on precision values. Curves that approach the upper-right corner achieve better results.

Figure 5.47 illustrates a comparison of precision versus recall curves of different color representation techniques using POC. It is clear that spatio-chromatic representation achieved the best performance in retrieval, due to the fact that it has the smallest amount of errors as observed before. Regular FFT achieved a little less performance than spatio-

chromatic FFT, but better than the three representations of QFT. The three types of QFT obtained the highest error rate among the tested representations. Consequently, their retrieval performance affected and achieved the worse retrieval performance, especially two-side QFT. In Figure 5.48 shows a comparison of precision-versus-recall curves of different color representations when introducing Band-Limited filtering (BLPOC). As the result of high error rates for all representations when using BLPOC, their retrieval performance is degraded. The best retrieval was achieved by regular FFT, and then by spatio-chromatic representation. The three types of QFT obtained the worst retrieval, especially left-side and right-side QFTs.
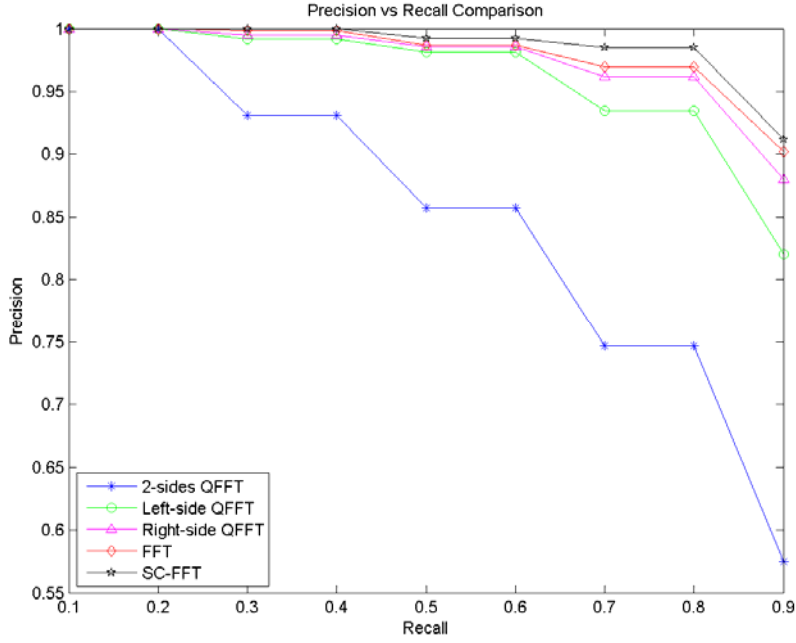
Figure 5.45: Precision versus recall comparison using POC.
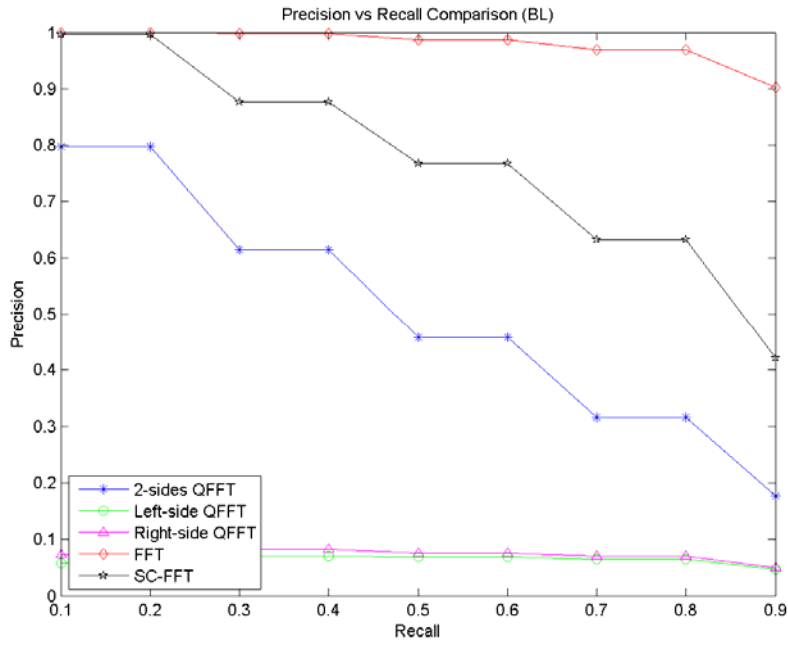
Figure 5.46: Precision versus recall comparison using Band-Limited POC.

5.5. Modified Daugman Method

The Daugman algorithm is used in order to test the performance of Quaternion color representation. Also, the Daugman algorithm is applied separately on each color, and then results are combined for comparison.

A Matlab implementation, provided by Masek [41], which implements the Daugman algorithm, is used in the experiment. Masek [41] used the 1D log-Gabor filter in the implementation. In this Thesis, the above-mentioned implementation is modified to use the 2D log-Gabor filter as proposed by Kovesi [42]. Also, the segmentation parameters are modified to work on the UBIRIS dataset.

5.5.1. Daugman Method for Separate RGB Colors

In order to use the Daugman method with regular 2D Log-Gabor filters, the color components of the input image are processed separately. Figure 5.47 shows how the algorithm works.
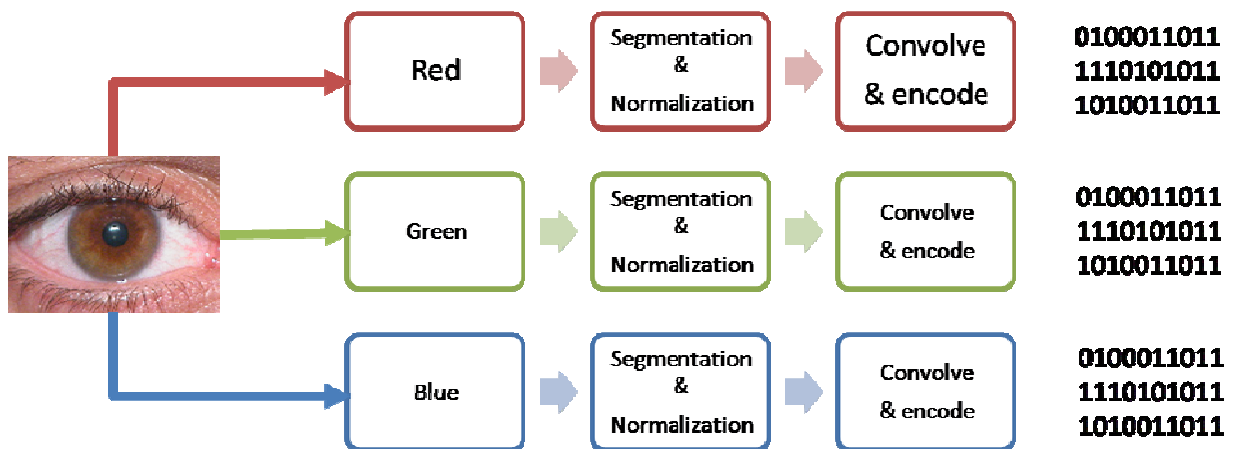
Figure 5.47: Illustration of Daugman algorithm for separate RGB colors.

Note that at the system output, there are three IrisCodes which will be combined to yield a single IrisCode signature. In order to achieve this fusion, two methods are used to merge the resulting IrisCodes signatures. The first method is implemented by calculating the Hamming distance separately for each color, and then taking the average of the three Hamming distances. The second technique is carried out by performing the Boolean XOR operation on the resulting IrisCodes signatures to obtain a single IrisCode signature which will then be used in the calculation of the Hamming distance.

Figure 5.48 shows genuine versus imposter distributions by the averaging method. It can be inferred from the figure that there are many errors in the result. This is because the performance measures are carried out on a very noisy iris database which resulted in many errors in the segmentation stage. These errors are propagated to the final result because many features are not captured. In Figure 5.49, FMR and FNMR of the result of using averaging technique are presented. It is clear that EER value is high. Furthermore, the ROC curve of averaging method results is very high, which strengthens the previous observation. The ROC curve is shown in Figure 5.50.

The genuine versus imposter distributions, based on the XOR operation, are shown in Figure 5.51. It can be clearly observed that the results indicate a poor performance. In Figure 5.52, the FMR and FNMR, based on using the XOR method, are presented. The EER value is high, which is consistent with the result obtained from genuine versus imposter distributions about the large number of errors. In addition, the ROC curve of the

XOR technique result is very high, which supports the previous observation. The ROC curve is shown in Figure 5.53.

Table 5.4 shows the decidability indices for the two fusion methods on the result of applying the Daugman method for separate RGB Colors. The XOR method achieved abetter decidability index, which means that its distributions are more separate than the average method. Also, the EER values of the two methods are almost identical. Thus, in general, the use of the XOR operation yielded better performance results.

Fusion Method	Decidability Index	EER
Average	0.2318	0.38
XOR	0.2776	0.39

Table 5.4: Decidability indices and EER for the two fusion methods.

Figure 5.48: Genuine versus imposter distributions for Daugman method using separate RGB colors and averaging.

Figure 5.49: FMR and FNMR for Daugman method using separate RGB colors and averaging.
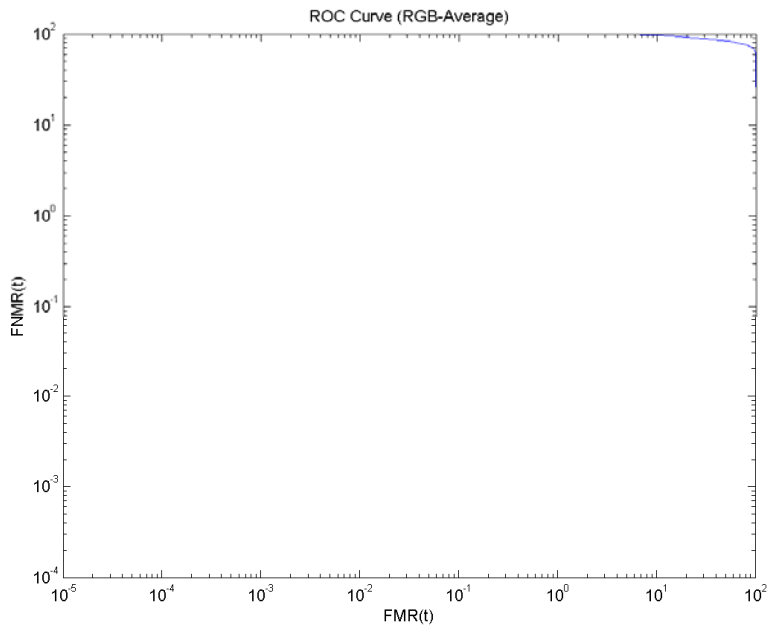
Figure 5.50: ROC curve for Daugman method using separate RGB colors and averaging.
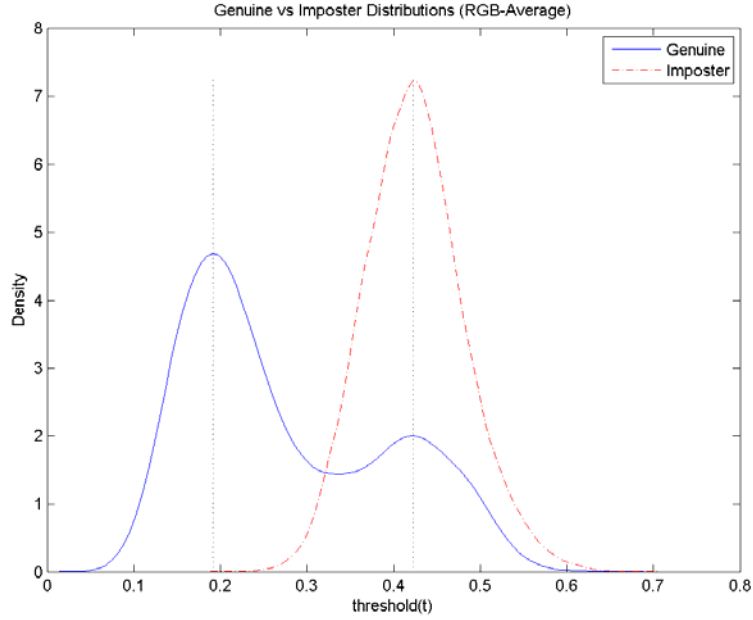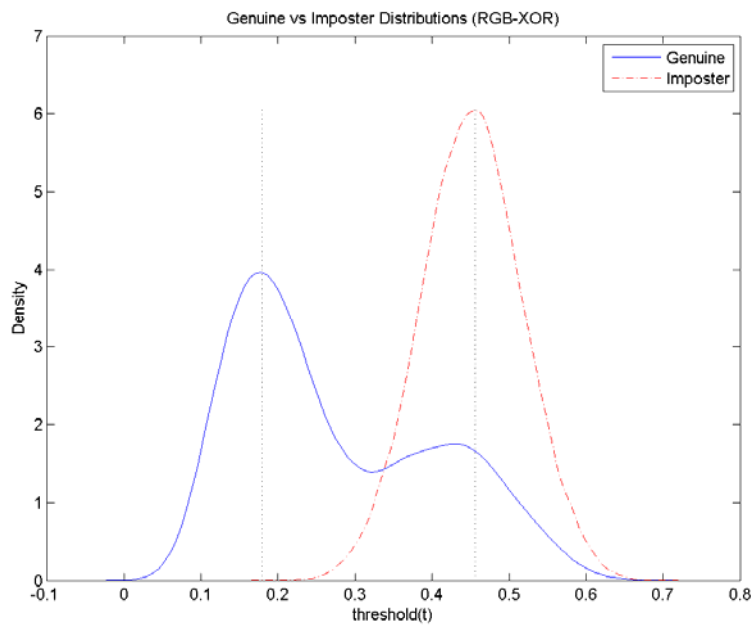

Figure 5.51: Genuine versus imposter distributions for Daugman method using separate

RGB colors and performing XOR operation.
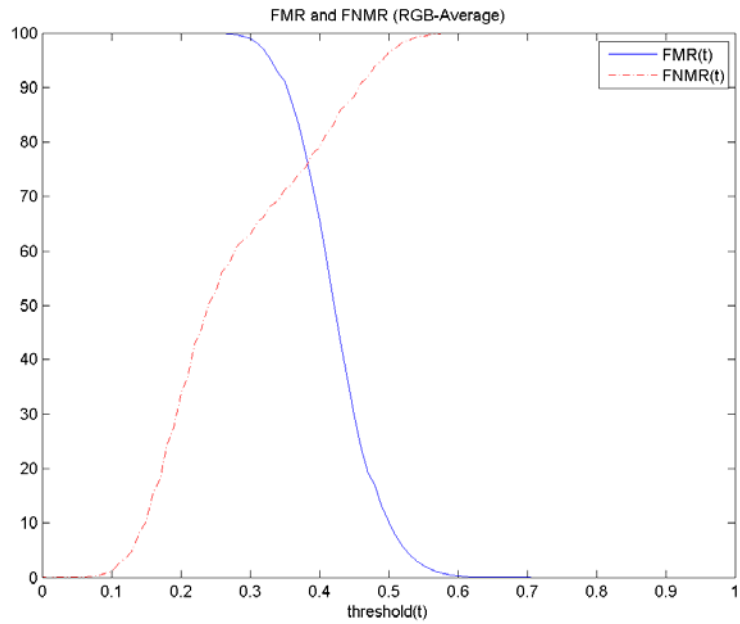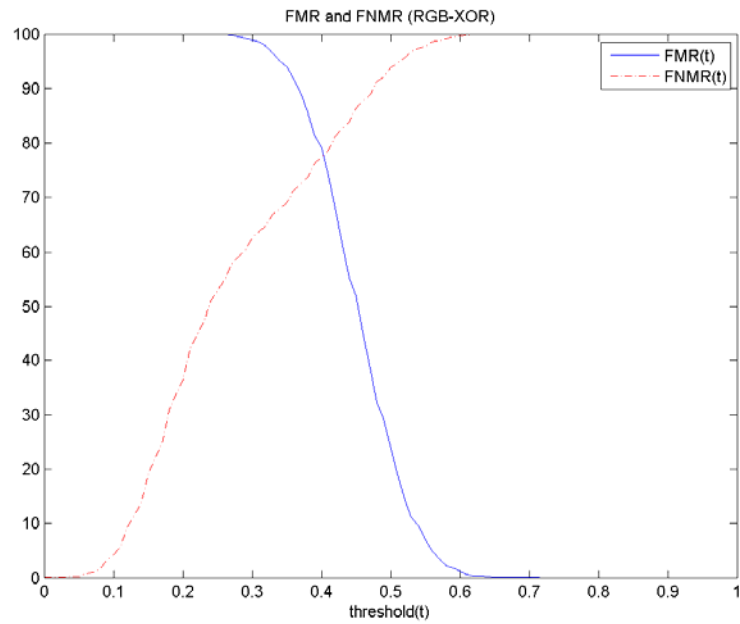
Figure 5.52: FMR and FNMR for Daugman method using separate RGB colors and performing XOR operation.
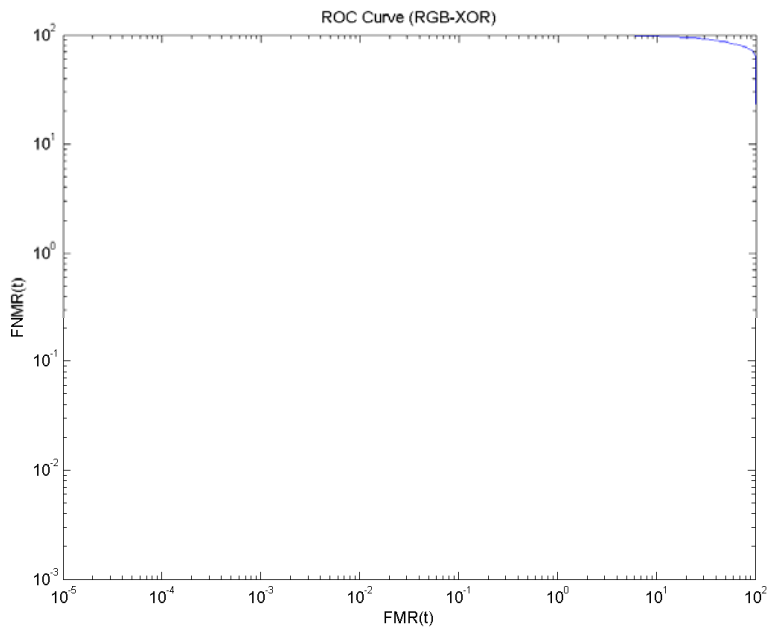
Figure 5.53: ROC curve for Daugman method using separate RGB colors and performing XOR operation.

5.5.2. Daugman Method for Quaternion Representation

The procedure of segmentation and normalization is the same as the one for processing RGB colors separately. After each color is normalized, they are combined into one Quaternion representation as described in section 3.5. Then, the quaternion image is convolved with the Quaternion 2D Log-Gabor filter, and the IrisCode is generated. This process is illustrated in Figure 5.54.
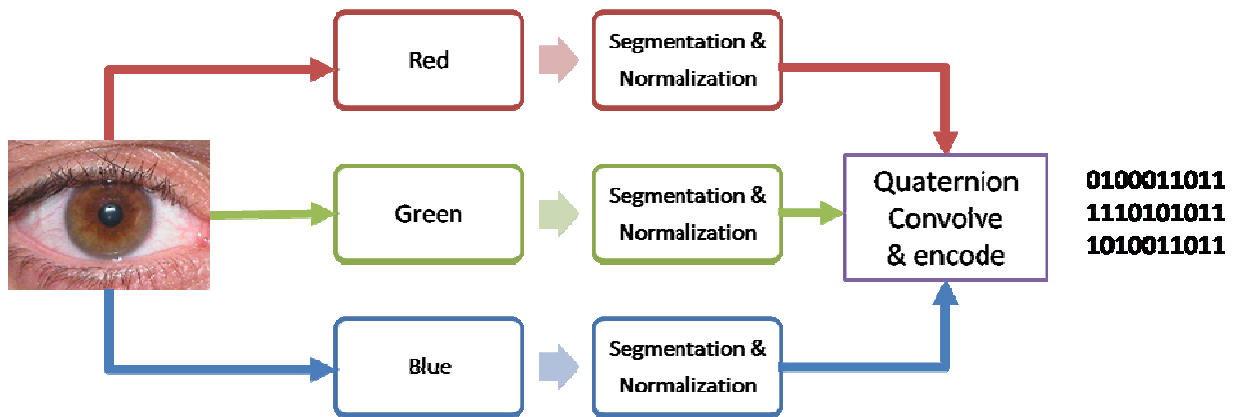
Figure 5.54: Illustration of Daugman algorithm for Quaternion representation.

As described in Section 2.1.1, Daugman quantized the result of convolution by setting 1 to real or imaginary parts if they are greater than 0, or 0 otherwise. But this is not applicable with the result of Quaternion convolution. This is because, by multiplying a pure unit Quaternion with the 2D Log-Gabor filter, the result is always a positive real part and 3 negative imaginary parts. Thus, Daugman quantization will not work.

In order to solve this problem, different ways of quantizing the results are tried. The first method is performed by calculating the average of each of the imaginary parts and use them as the decision boundary. Several images are used to determine the average of each imaginary part. The second method of quantization is done by dividing the Quaternion image with the magnitude and adding 0.5 to distribute the values above and below zero.

Figure 5.55 shows genuine versus imposter distributions by the average method. The large intersection area indicates many errors in the result. This is due to the fact that the used iris database contains many noisy images which make the result of feature extraction contain a lot of errors. In Figure 5.56, the FMR and FNMR of the result of the average technique are presented. Although EER has a slightly high value, it is less than the previous method for separate RGB colors. This indicates that the errors are reduced by using the average Quaternion method. The ROC curve of the averaging method is shown in Figure 5.57. Because of the high number of errors, the curve is very high in the Figure.

Genuine versus imposter distributions given by the divide-by-magnitude technique are illustrated in Figure 5.58. As with the average method, the resulting errors are large because of the problems of segmentation and feature extraction of the noisy iris images. This is supported with FMR and FNMR curves as shown in Figure 5.59. The achieved EER value is the same as the one achieved by the average Quaternion technique. The ROC curve of the result by the divide-by-magnitude method is shown in Figure 5.60. The height of the curve supports the previous observation about the number of errors.

Table 5.5 shows the decidability indices for the two quantization methods used in the experiments. It is clear that the average technique achieved the best separation between genuine and imposter distributions. In addition, the EER values are the same for both techniques. Thus, the average quantization method yields better results.

Quantization Method	Decidability Index	EER
Average	0.2849	0.23
Divide-by-magnitude	0.1737	0.23

Table 5.5: Decidability indices and EER for the two quantization methods.
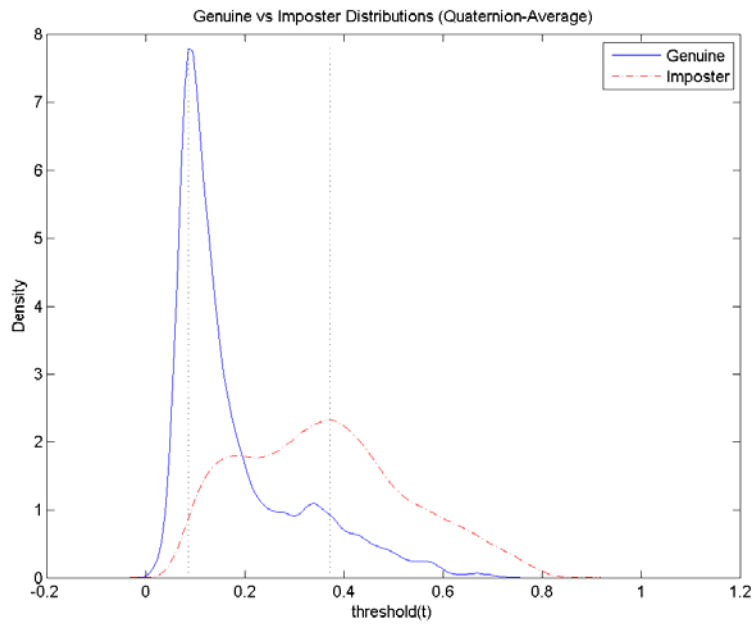
Figure 5.55: Genuine versus imposter distributions for Daugman method using Quaternion representation with average quantization.
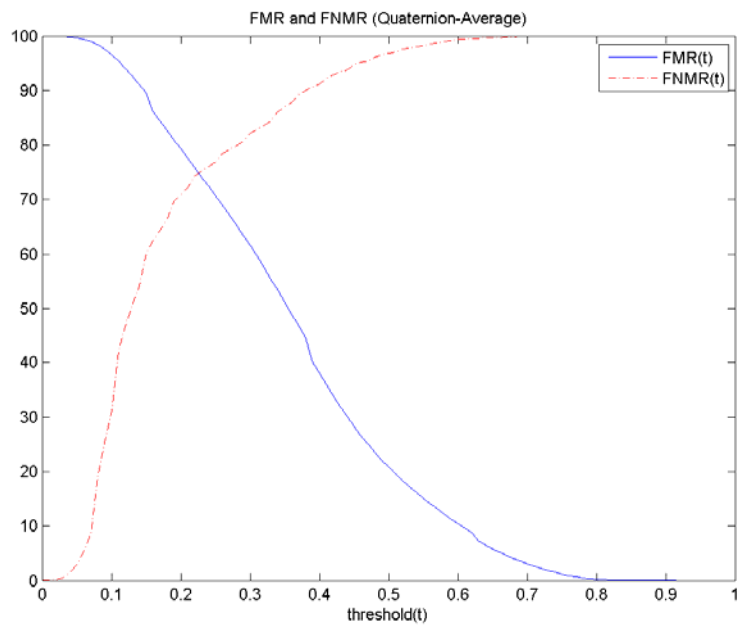
Figure 5.56: FMR and FNMR for Daugman method using Quaternion representation with average quantization.
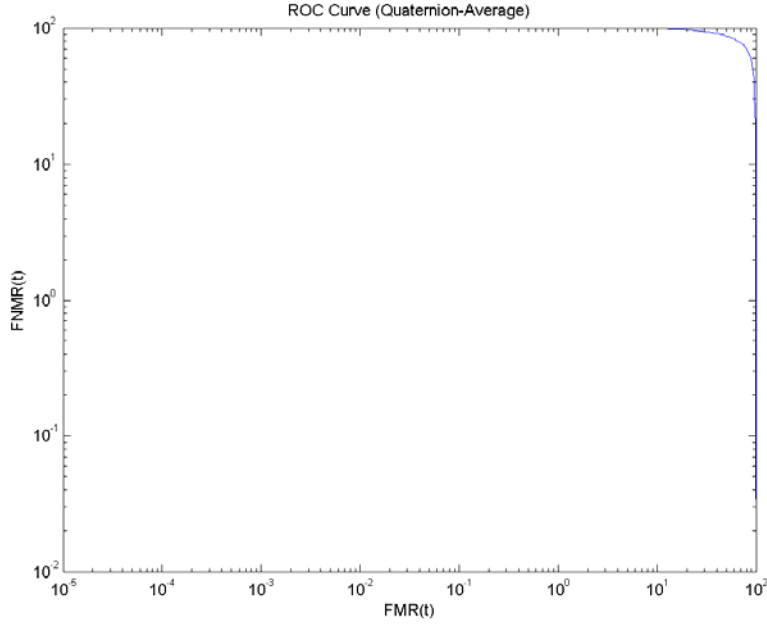
Figure 5.57: ROC curve for Daugman method using Quaternion representation with average quantization.
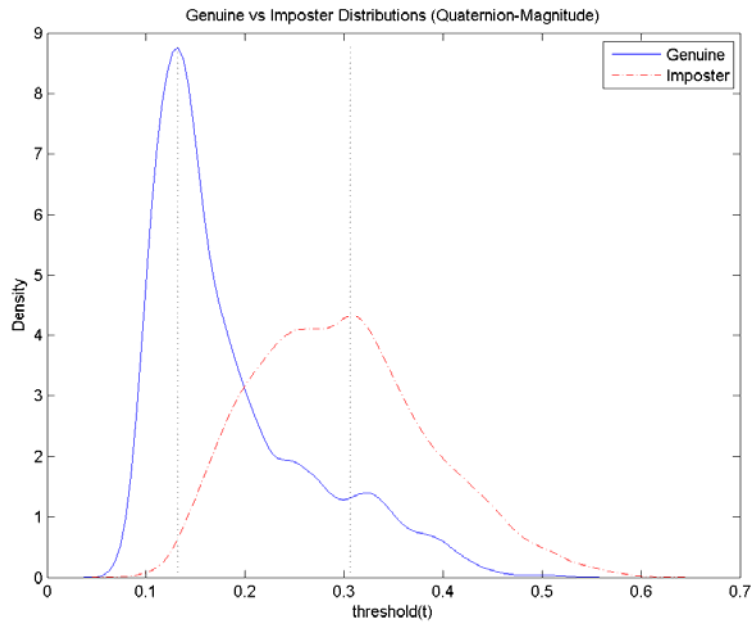
Figure 5.58: Genuine versus imposter distributions for Daugman method using Quaternion representation with divide-by-magnitude quantization.
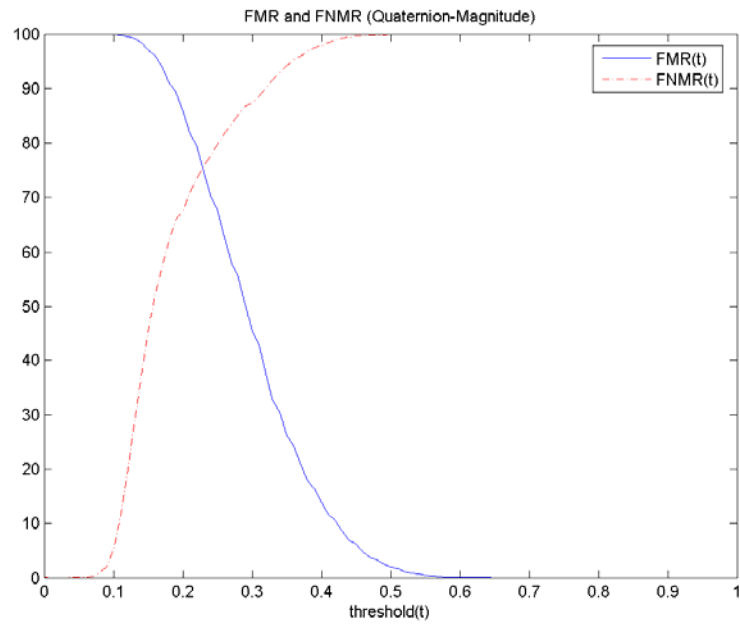
Figure 5.59: FMR and FNMR for Daugman method using Quaternion representation with divide-by-magnitude quantization.
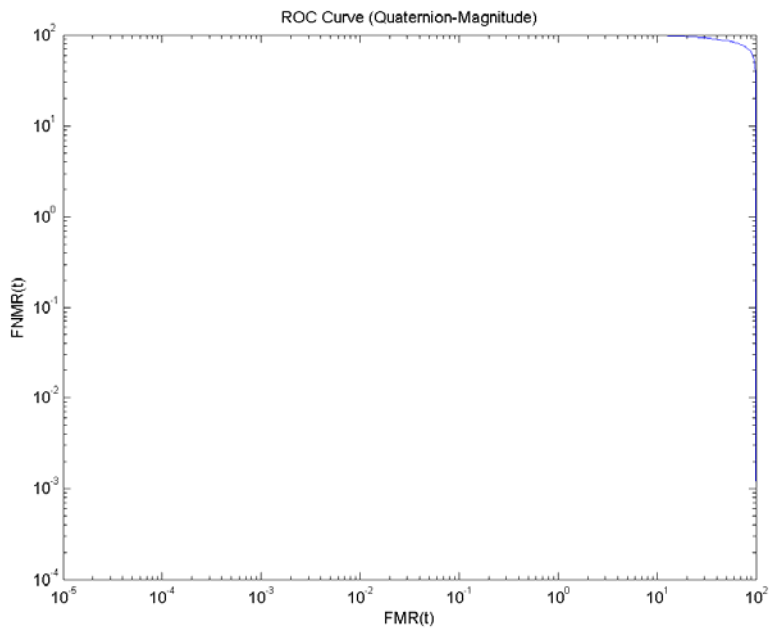
Figure 5.60: ROC curve for Daugman method using Quaternion representation with divide-by-magnitude quantization.

5.5.3. POC on Segmented and Normalized Color Iris Images

The Phase Only Correlation (POC) algorithm is performed on the segmented and normalized color iris images. Each color component is segmented and normalized as in the previous two sections. The maximum correlation of the three color components is taken as the correlation of the color image. The process of performing POC on two iris images is illustrated in Figure 5.61.
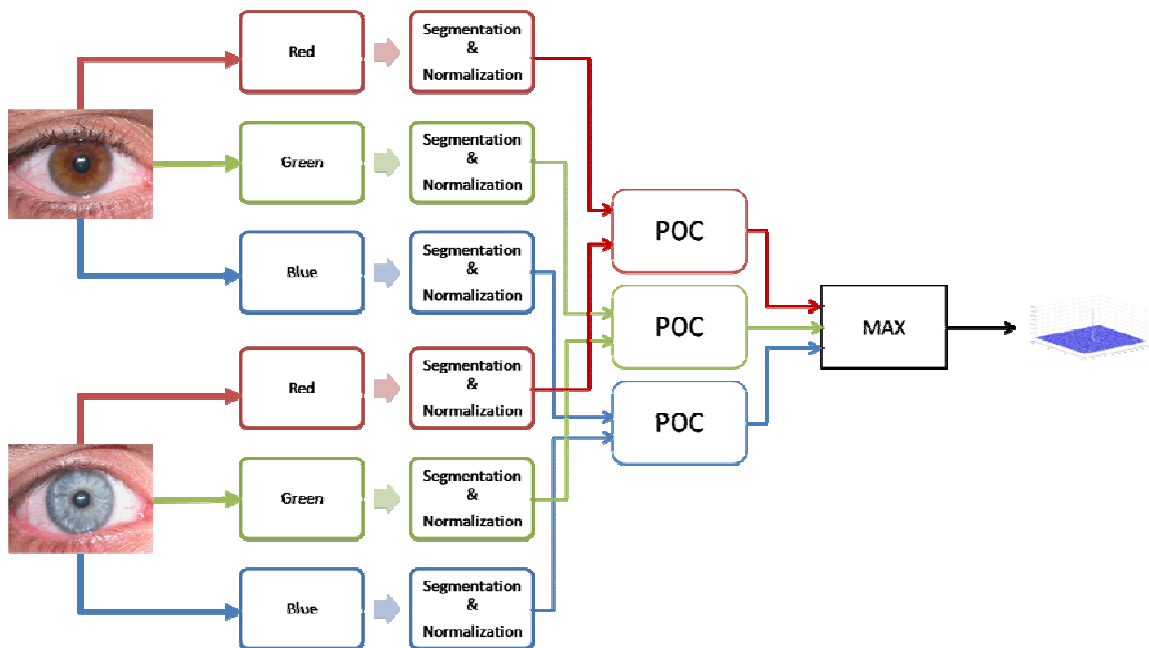
Figure 5.61: Process of performing POC on two segmented and normalized irises.

Figure 5.62 illustrates the genuine and imposter distributions of performing POC on two normalized color iris images. It is clear that the separation between the two distributions

is very small. Also, the intersection area between genuine and imposter distributions indicates that many errors occur. As mentioned before, this is due to the use of noisy database. In Figure 5.63, the FMR and FNMR curves are presented. EER has a lower value compared with the previous two techniques base on the Daugman algorithm. This indicates that fewer errors are obtained. This observation is consistent with the shape of the ROC curve which is a little lower than the previous two methods. The ROC curve is shown in Figure 5.64. Table 5.6 shows the decidability index and EER value for the discussed method.

Correlation Method	Decidability Index	EER
POC on segmented and normalized color iris image	0.0178	0.1

Table 5.6: Decidability indices and EER for the two quantization methods.
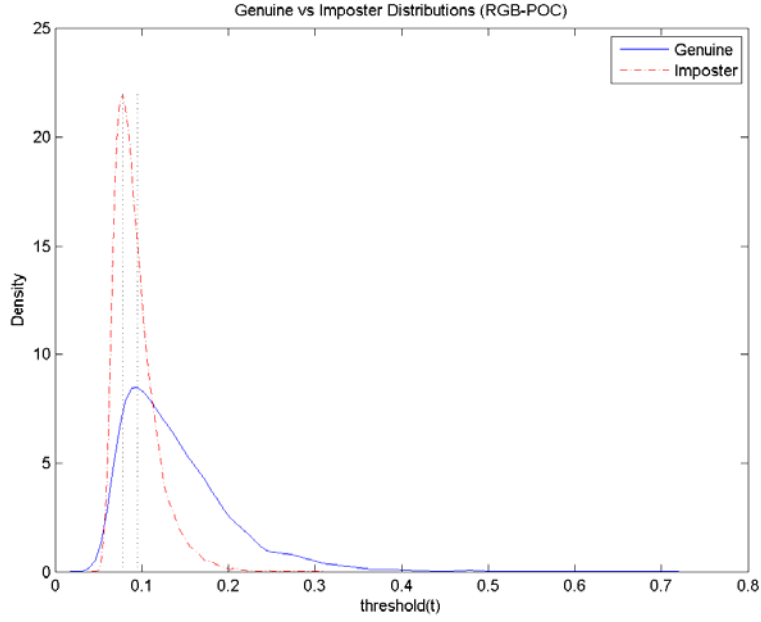
Figure 5.62: Genuine versus imposter distributions for POC on normalized images.
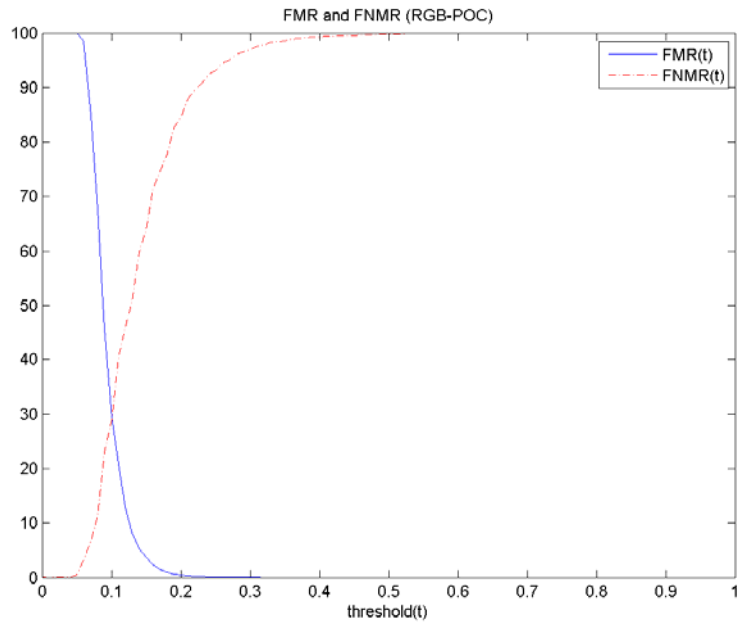
Figure 5.63: FMR and FNMR curves for POC on normalized images.

111
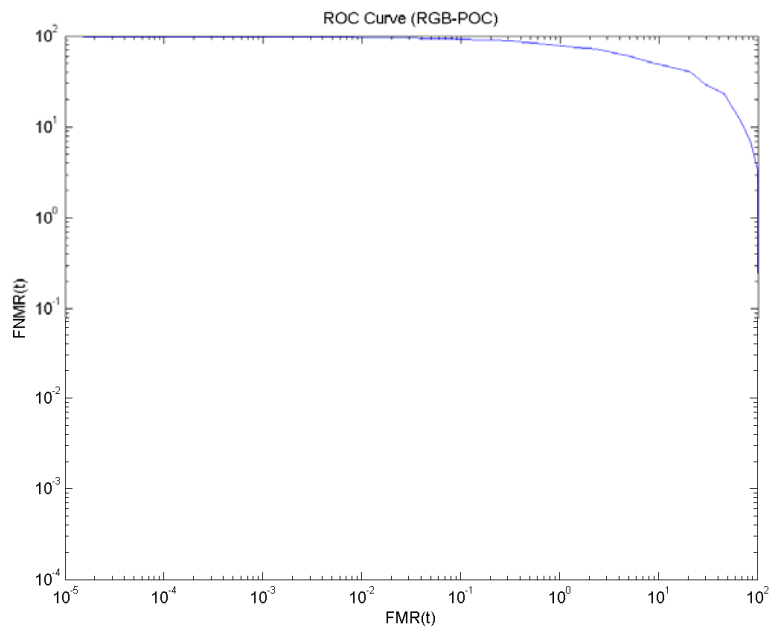
Figure 5.64: ROC curve for POC on normalized images.

CHAPTER SIX

CONCLUSION

6.1. Introduction

This Chapter summarizes of the research and findings, and it presents the limitations of this research. Finally, it offers suggestions for future improvements.

6.2. Summary and Findings

This research investigated the use of colors in the process of iris identification. An explanation of hypercomplex (Quaternion) numbers was provided, and then the Quaternion Fourier Transform (QFT) was derived. Also, Gabor filters and Log-Gabor filters were explained, and Quaternion Gabor filters that extend Gabor filters were introduced. Comparisons of the performance of the three types of QFT, regular FFT, and spatio-chromatic FT were performed. The used performance measures were Phase-Only Correlation (POC) and Band-Limited Phase-Only Correlation (BLPOC). Two types of experiments were conducted:

1. Measuring the performance against different types of noise. The tested noises were: Gaussian noise, rotations, average filtering, median filtering, and compression using JPEG. For all types of noises, it was found that the three types of QFT performed much better than the other two methods. Also, Band-Limited

filtering (BLPOC) yields better results than POC. This is due to the removal of high frequencies which contain most of the noise.

2. Measuring the performance against different images. Genuine and imposter distributions, FMR and FNMR curves, the ROC curve, and the precision-versus-recall curve were used to assess the performance against different images. It was found that the three types of QFT achieved the best separation between genuine and imposter distributions, but with the cost of more errors than the other representations. These errors affect the retrieval performance of the three types of QFT, which was less than the other representations. Also, it was found that BLPOC yields worse results than POC. This is because the most discriminating information, such as edges, is in the high frequencies which are discarded in the filtering process.

The Daugman algorithm for iris identification was extended to use color images in a holistic manner. This was done by representing color iris images in Quaternion representation and by using Quaternion Log-Gabor filters for the filtering and feature extraction. Two techniques of quantization were used: calculating averages of imaginary parts, and dividing by magnitude. The averaging method achieved better performance than dividing by magnitude.

For comparison, the Daugman method was performed separately on each color component of the input image. For the fusion of the result, two techniques were used. The first was carried out by getting the Hamming distance of all the three color components

and then calculating their average. The second technique was done by performing the XOR operation on the three IrisCodes, and then calculating the Hamming distance of the result. The XOR technique obtained the best result. By comparing the best results of the Daugman algorithm using Quaternion representation and three separate colors, it was concluded that the Quaternion representation achieved the best separation with the lowest rate of errors.

Finally, POC was performed on separated segmented and normalized color components, and then the results of them were combined. It was found that there was very little separation between genuine and imposter distributions and fewer errors than with the Quaternion Daugman algorithm.

6.3. Limitations

Some limitations were faced in this research:

1. Lack of clear definitions: The use of Quaternion numbers for representing and processing color images did not receive a lot of attention in the literature. Thus, contributions for this topic are very scarce. Furthermore, definitions of some concepts can be interpreted in different ways. For example, the conjugate of Quaternion numbers can be obtained in different ways. Also, there are several attempts to derive Quaternion Gabor filters in the literature, each with a different approach.

2. Interpretation of the results of the Quaternion and spatio-chromatic transforms are not the same as the interpretation of the results of the regular Fourier Transform. It is not clear how to interpret and visualize the results of them, and thus there is a difficulty in comparing the results properly.

3. The concept of filtering and convolution are different among the three used representations. Filtering and convolution in the regular Fourier domain are well defined, but they are not fully studied in the Quaternion and spatio-chromatic domains.

4. The used dataset is a very noisy dataset that contains images with different types and degrees of noises. Consequently, it yields very bad results due to errors in segmentation.

6.4. Future Work

The use of Quaternion numbers to represent and process color images is a complicated task and did not receive a lot of attention in the research literature. Some of the suggested future studies to enhance the present research are:

1. Study the results of QFT and Quaternion Gabor filters, and provide interpretation and visualization to better understand them.

2. Develop efficient Quaternion filters, study the mechanism of filtering in the Quaternion domain, and try to find relationships with filtering in the Fourier domain.

3. Use a noise-free color iris database to verify the results of this research.

4. Develop a better quantization technique in order to enhance the performance of the proposed system.

5. Investigate and develop a method for color iris segmentation by using the Quaternion representation of images.

REFERENCES

[1] L. Masek, "Recognition of Human Iris Patterns for Biometric Identification," 2003.

[2] J. Daugman, "High Confidence Visual Recognition of Persons by a Test of Statistical Independence," *IEEE Transaction on Pattern Analysis and Machine Intelligence*, vol. 15, no. 11, 1993.

[3] S. Haykin, *Neural Networks: A Comprehensive Foundation (second edition)*. Prentice Hall, 1999.

[4] J. Daugman, " How iris recognition works," in *International Conference on Image Processing*, 2002, pp. I-33-I-36vol1.

[5] J. Daugman, "How iris recognition works," *IEEE Transactions on Circuits and Systems for Video Technology*, vol. 14, no. 1, pp. 21-30, 2004.

[6] R. P. Wildes, "Iris recognition: an emerging biometric technology," *Proceedings of the IEEE*, vol. 85(9), pp. 1348-1363, 1997.

[7] W. W. Boles and B. Boashash, "A human identification technique using images of the iris andwavelet transform," *IEEE Transactions on Signal Processing*, vol. 46, no. 4, pp. 1185-1188, 1998.

[8] L. Ma, T. Tan, Y. Wang, and D. Zhang, "Efficient iris recognition by characterizing

key local variations," *IEEE Trans. Image Process.*, vol. 13, no. 6, 2004.

[9] K. Miyazawa, K. Ito, T. Aoki, K. Kobayashi, and A. Katsumata, "An Iris Recognition System Using Phase-Based Image Matching," in *IEEE International Conference on Image Processing*, 2006, pp. 325-328.

[10] K. Miyazawa, K. Ito, T. Aoki, K. Kobayashi, and H. Nakajima, "An Effective Approach for Iris Recognition Using Phase-Based Image Matching," *IEEE Transaction of Pattern Analysis and Machine Intelligence*, vol. 30, no. 10, 2008.

[11] R. C. Gonzalez and R. E. Woods, *Digital Image Processing (Third Edition)*. Pearson Prentice Hall, 2008.

[12] I. Koichi, N. Hiroshi, K. Koji, A. Takafumi, and H. Tatsuo, "A Fingerprint Matching Algorithm Using Phase-Only Correlation," *IEICE Trans. Fundam. Electron. Commun. Comput. Sci.*, vol. E87-A, no. 3, 2004.

[13] Y.-P. Huang, S.-W. Luo, and E.-Y. Chen, "An efficient iris recognition system," in *International Conference on Machine Learning and Cybernetics*, 2002.

[14] L. Ma, T. Tan, Y. Wang, and D. Zhang, "Personal identification based on iris texture analysis," *IEEE Transactions on Pattern Analysis and Machine Intelligence*, vol. 25, no. 12, 2003.

[15] B. Son, H. Won, G. Kee, and Y. Lee, " Discriminant iris feature and support vector

machines for iris recognition," in *International Conference on Image Processing*, 2004, pp. 865-868Vol2.

[16] P.-F. Zhang, D.-S. Li, and Q. Wang, " A novel iris recognition method based on feature fusion," in *International Conference on Machine Learning and Cybernetics*, 2004, pp. 3661-3665vol6.

[17] M. K. Khan, J. Zhang, and S. .-J. Horng, " An effective iris recognition system for identification of humans ," in *8th International Multitopic Conference*, 2004, pp. 114-117.

[18] R. W. Ives, A. J. Guidry, and D. M. Etter, "Iris recognition using histogram analysis," in *The Thirty-Eighth Asilomar Conference on Signals, Systems and Computers*, 2004.

[19] J.-G. Ko, Y.-H. Gil, and J.-H. Yoo, "Iris Recognition using Cumulative SUM based Change Analysis," in *International Symposium on Intelligent Signal*, 2006.

[20] V. Conti, G. Milici, F. Sorbello, and S. Vitabile, "A Novel Iris Recognition System based on Micro-Features," in *IEEE Workshop on Automatic Identification Advanced Technologies*, 2007, pp. 253-258.

[21] S. P. Narote, A. S. Narote, L. M. Waghmare, M. B. Kokare, and A. N. Gaikwad, " An iris recognition based on dual tree complex wavelet transform," in *IEEE Region*

10 Conference TENCON, 2007, pp. 1-4.

[22] K. N., "A Dual-Tree Complex Wavelet Transform with improved orthogonality and symmetry properties," in *International Conference on Image Processing*, 2000.

[23] W. Anna, C. Yu, W. Jie, and Zhangxinhua, "Iris Recognition Based on Wavelet Transform and Neural Network," in *IEEE/ICME International Conference on Complex Medical Engineering*, 2007.

[24] N. Sudha, N. B. Puhan, X. Hua, and J. Xudong, "Iris recognition on edge maps," in *6th International Information, Communications & Signal Processing*, 2007.

[25] R. Szewczyk, "New Features Extraction Method for People Recognition on the Basis of the Iris Pattern," in *14th International Conference on Mixed Design of Integrated Circuits and Systems*, 2007.

[26] E. Krichen, M. Chenafa, S. Garcia-Salicetti, and B. Dorizzi, "Color-Based Iris Verification," in *Advances in Biometrics*. Springer, 2007.

[27] J. Hanson, "Introduction to quaternions," DigiPen Institute of Technology, 2005.

[28] S.-C. Pei, J.-J. Ding, and J.-H. Chang, "Efficient implementation of quaternion Fourier transform, convolution, and correlation by 2-D complex FFT," *IEEE Transactions on Signal Processing*, vol. 49, no. 11, 2001.

[29] S. J. S. T.A. Ell, "Hypercomplex Fourier Transforms of Color Images," *IEEE Transactions on Image Processing*, vol. 16, no. 1, 2007.

[30] A. McCabe, T. Caelli, G. West, and A. Reeves, "Theory of spatiochromatic image encoding and feature extraction," *Journal of the Optical Society of America A: Optics, Image Science, and Vision*, vol. 17, no. 10, 2000.

[31] R. Lukac and K. N. Plataniotis, *Color Image Processing Methods and Applications*. CRC Press, 2007.

[32] D. Gabor, "Theory of Communication," *J. IEE*, vol. 93:429-457, 1946.

[33] C. F. Jones, "Color Face Recognition using Quaternionic Gabor Filters," PHD Dissertation, 2004.

[34] D. H. W. E. Dunn, "Optimal Gabor filters for texture segmentation," *IEEE Transactions on Image Processing*, vol. 4, no. 7, 1995.

[35] D. J. Field, "Relations between the statistics of natural images and the. response properties of cortical cells," *J. Opt. Soc. Am. A,*, vol. 4, no. 12, 1987.

[36] P. Kovesi. What Are Log-Gabor Filters and Why Are They Good?. [Online]. http://www.csse.uwa.edu.au/~pk/Research/MatlabFns/PhaseCongruency/Docs/conv expl.html

[37] G. S. Thomas Bulow, "Quaternionic Gabor filters for local structure classification," in *14th International Conference on Pattern Recognition*, 1998.

[38] P. Hugo and L. A. Alexandre, "UBIRIS: A noisy iris image database," in *Proceed. of ICIAP 2005 - Intern. Confer. on Image Analysis and Processing*, 2005.

[39] D. Maltoni, D. Maio, A. K. Jain, and S. Prabhakar, *Handbook of Fingerprint Recognition*. New York: Springer, 2003.

[40] R. Baeza-Yates and B. Ribeiro_Neto, *Modern Information Retrieval*. New York: Addison-Wisley, 1999.

[41] P. K. Libor Masek. (2003) MATLAB Source Code for a Biometric Identification System Based on Iris Patterns.

[42] P. D. Kovesi. MATLAB and Octave Functions for Computer Vision and Image Processing. [Online]. http://www.csse.uwa.edu.au/~pk/Research/MatlabFns/

Vita

Personal Information	- Date of Birth: 1982 - Place of Birth: Riyadh - Languages:
	   1. Arabic (native language)
	   2. English

Education and Work	2000 -2005: King Fahd University of Petroleum & Minerals Dhahran, Bachelor of Science in Software Engineering 2005-2006: Researcher at Computer and Electronic Research Institute in King Abdul-Aziz City for Science and Technology 2006-2009: King Fahd University of Petroleum & Minerals Dhahran, Master of Science in Computer Science
Publications	El-Alfy, E.-S. M.; Al-Qunaieer, F. S. "A fuzzy similarity approach for automated spam filtering," IEEE/ACS International Conference on Computer Systems and Applications, 2008
Interests	- Image processing and pattern recognition - Machine learning - Software Engineering topics (such as: requirements, design, testing, project management … etc). - Web development